

On Retrieving Profiles of CO₂ in the Lower Atmosphere using Spectroscopy in the Near and Far Infrared: A Preliminary Study

By
Matthew J. Christi and Graeme L. Stephens

Department of Atmospheric Science
Colorado State University
Fort Collins, Colorado

Research supported by DOE/ARM research grant #DE-FG03-94ER61748 and NOAA Research grant #NA17RJ1228.



**Department of
Atmospheric Science**

Paper No. 278

ON RETRIEVING PROFILES OF CO₂ IN THE LOWER ATMOSPHERE USING
SPECTROSCOPY IN THE NEAR AND FAR INFRARED: A PRELIMINARY
STUDY

Matthew J. Christi and Graeme L. Stephens

Research Sponsored by DOE/ARM Research Grant #DE-FG03-94ER61748 and
NOAA Research Grant #NA17RJ1228.

Department of Atmospheric Science
Colorado State University
Fort Collins, Colorado 80523

July 2002

Atmospheric Science Paper No. 728

ABSTRACT

ON RETRIEVING PROFILES OF CO₂ IN THE LOWER ATMOSPHERE USING SPECTROSCOPY IN THE NEAR AND FAR INFRARED: A PRELIMINARY STUDY

The amount of CO₂ in the atmosphere has received much attention in the scientific community in recent years in relation to its potential influence on the earth's radiation budget and the resulting impact on earth's climate. Various studies have been conducted with the goal of illuminating the relationship of CO₂ in its role in climate and climate change; however, the goal has remained somewhat elusive in part due to a lack of quantitative data on the carbon cycle. With the goal of obtaining a better understanding of climate in general and the carbon cycle in particular, this work explores the feasibility of retrieving profiles of CO₂ from instruments located on a spaceborne platform using moderate resolution measurements in the infrared and high resolution measurements from the 1.6 μm region in the near infrared.

The results of this study show that the measurements from the near and far infrared work in a complementary fashion in retrieving profiles of CO₂ in the lower atmosphere. For each retrieval scenario, an *a priori* profile of CO₂ concentration is used to assist in constraining the measurements. Results indicate a precision in the CO₂ column-averaged values of better than 1 ppmv for the clear sky cases run.

Results also indicate a precision in column-averaged value of better than 2.5 ppmv for the majority of cases ($\approx 73\%$) with a layer of thin cloud or aerosol present

($\tau < 0.2$) for an initial retrieval over a given locale provided there exists a means of detecting the height of a scattering layer to 1 km and the optical depth of the scattering layer to 10%. However, there is good reason to anticipate even better results once a number of retrievals are performed and the *a priori* tuned to a given locale using the results of previous retrievals.

Based on current research, it is estimated that the errors in resulting monthly-averaged column-average values of CO₂ from any such retrievals need to be less than 2.5 ppmv to be useful to researchers attempting to determine the location and magnitude of CO₂ surface sources and sinks. If space-based measurements are to be useful in estimating CO₂ over broad regions not covered by thicker clouds, it appears that measurements in addition to those used from the near and far infrared in this work will be needed to mitigate the effects of scatter by optically thin cirrus and aerosol and other sources of potential retrieval bias.

ACKNOWLEDGEMENTS

I would like to thank Dr. Philip Gabriel for his invaluable input during the development of the forward model used for the Near Infrared ("Radiant") and to Dr. Angela Benedetti for important data with which to compare during early testing of the model. I would also like to thank Dr. Richard Engelen for the infrared model used in this work as well as helpful thoughts and suggestions made by Dr. Richard Austin and Dr. Tristan L'Ecuyer. This work was sponsored by DOE/ARM research grant #DE-FG03-94ER61748 and NOAA research grant #NA17RJ1228.

Contents

1	Introduction	1
1.1	Motivation for This Work	1
1.2	In Situ and Remote Measuring of Atmospheric CO ₂	3
1.3	Looking Ahead	7
2	Absorption Bands of CO₂ in the Near Infrared	9
3	Atmospheric Absorption and Scattering	13
3.1	Rayleigh Scattering	14
3.2	Absorption and Scattering by Clouds and Aerosol	15
3.3	Absorption by Atmospheric Gases	16
4	Radiative Transfer and the Forward Models	21
4.1	Radiative Transfer Theory	21
4.2	Forward Model for the Near Infrared	23
4.3	Forward Model for the Infrared	27
5	Retrieving Atmospheric Parameters: Theory and Application to CO₂	29
5.1	Retrieval Theory	29
5.2	Application of the Method to Retrieving Profiles of CO ₂	33
6	Near Infrared Sensitivity Study	37

6.1	Sensitivity to Cirrus and Aerosol	38
6.2	Sensitivity to CO ₂	58
7	Retrieval Results	65
7.1	Retrieving a Profile of CO ₂ in Clear Sky	65
7.2	Retrieving a Profile of CO ₂ in the Presence of Thin Cirrus	78
7.3	Retrieving a Profile of CO ₂ in the Presence of Thin Aerosol	91
8	Conclusions and Future Work	101
A	Radiant	111
A.1	Introduction	111
A.1.1	Doubling/Adding and DISORT	111
A.1.2	Radiant: An Efficient Approach to Computing Radiative Transfer	113
A.2	Modified Eigenmatrix Method	115
A.3	Truncated Series Method	116
A.4	Radiant, DISORT, and doubling/adding: Accuracy Comparisons	118
A.5	Radiant, DISORT, and doubling/adding: Timing Comparisons	120
B	Global Transmission and Reflection Matrices: Numerical Consider- ations	125

List of Figures

1.1	Global Greenhouse Sampling Network (Source: Climate Monitoring and Diagnostics Laboratory)	4
1.2	Averaging kernels from a CO ₂ retrieval performed with simulated measurements from the far infrared only.	5
2.1	Absorption bands of CO ₂ located in the NIR at 1.6 and 2.0 μm	10
3.1	Scattering pattern corresponding to Rayleigh scatter.	15
4.1	Physical processes affecting the transfer of radiation through a medium.	22
4.2	The interaction principle illustrated for a homogeneous layer.	26
5.1	Mean vertical CO ₂ profile for midlatitudes (44°N), full dots (Schmidt and Khedim, 1991).	35
6.1	Sensitivity of 1.6 μm radiances to thin cirrus and aerosol for $\alpha = 0.1$ and $\theta_{\odot} = 0^{\circ}$	42
6.2	Sensitivity of 1.6 μm radiances to thin cirrus and aerosol for $\alpha = 0.1$ and $\theta_{\odot} = 30^{\circ}$	43
6.3	Sensitivity of 1.6 μm radiances to thin cirrus and aerosol for $\alpha = 0.1$ and $\theta_{\odot} = 45^{\circ}$	44
6.4	Sensitivity of 1.6 μm radiances to thin cirrus and aerosol for $\alpha = 0.1$ and $\theta_{\odot} = 60^{\circ}$	45

6.5	Sensitivity of $1.6\mu m$ radiances to thin cirrus and aerosol for $\alpha = 0.25$ and $\theta_{\odot} = 0^{\circ}$	46
6.6	Sensitivity of $1.6\mu m$ radiances to thin cirrus and aerosol for $\alpha = 0.25$ and $\theta_{\odot} = 30^{\circ}$	47
6.7	Sensitivity of $1.6\mu m$ radiances to thin cirrus and aerosol for $\alpha = 0.25$ and $\theta_{\odot} = 45^{\circ}$	48
6.8	Sensitivity of $1.6\mu m$ radiances to thin cirrus and aerosol for $\alpha = 0.25$ and $\theta_{\odot} = 60^{\circ}$	49
6.9	Sensitivity of $1.6\mu m$ radiances to thin cirrus and aerosol for $\alpha = 0.4$ and $\theta_{\odot} = 0^{\circ}$	50
6.10	Sensitivity of $1.6\mu m$ radiances to thin cirrus and aerosol for $\alpha = 0.4$ and $\theta_{\odot} = 30^{\circ}$	51
6.11	Sensitivity of $1.6\mu m$ radiances to thin cirrus and aerosol for $\alpha = 0.4$ and $\theta_{\odot} = 45^{\circ}$	52
6.12	Sensitivity of $1.6\mu m$ radiances to thin cirrus and aerosol for $\alpha = 0.4$ and $\theta_{\odot} = 60^{\circ}$	53
6.13	Sensitivity of $1.6\mu m$ radiances to thin cirrus and aerosol for $\alpha = 0.75$ and $\theta_{\odot} = 0^{\circ}$	54
6.14	Sensitivity of $1.6\mu m$ radiances to thin cirrus and aerosol for $\alpha = 0.75$ and $\theta_{\odot} = 30^{\circ}$	55
6.15	Sensitivity of $1.6\mu m$ radiances to thin cirrus and aerosol for $\alpha = 0.75$ and $\theta_{\odot} = 45^{\circ}$	56
6.16	Sensitivity of $1.6\mu m$ radiances to thin cirrus and aerosol for $\alpha = 0.75$ and $\theta_{\odot} = 60^{\circ}$	57
6.17	Sensitivity of NIR radiances to CO_2 in clear sky scenarios.	60
6.18	Sensitivity of radiances to CO_2 in clear sky for varying values of α	62
6.19	Sensitivity of radiances to CO_2 in clear sky for varying values of θ_{\odot}	63

7.1	Retrieved source profile of CO ₂ with associated profiles of error statistics for measurements with $\alpha = 0.06$ and $\theta_{\odot} = 0^{\circ}$	73
7.2	Retrieved source profile of CO ₂ with associated profiles of error statistics for measurements with $\alpha = 0.25$ and $\theta_{\odot} = 0^{\circ}$	74
7.3	Retrieved source profile of CO ₂ with associated profiles of error statistics for measurements with $\alpha = 0.40$ and $\theta_{\odot} = 0^{\circ}$	75
7.4	Comparison of retrieved source profile of CO ₂ with associated profiles of error statistics for measurements where $\alpha = 0.06$ and θ_{\odot} takes on values of 0° and 30°	76
7.5	Comparison of retrieved source profile of CO ₂ with associated profiles of error statistics for measurements where $\alpha = 0.40$ and θ_{\odot} takes on values of 0° and 30°	77
7.6	(i) Retrieved source profile of CO ₂ with associated profiles of error statistics obtained by using both IR and NIR measurements in the presence of a cirrus cloud at 13 km with $\tau = 0.1$ where $\alpha = 0.06$ and $\theta_{\odot} = 0^{\circ}$: CASE 1 and 2.	83
7.6	(cont'd) (ii) Retrieved source profile of CO ₂ with associated profiles of error statistics obtained by using both IR and NIR measurements in the presence of a cirrus cloud at 13 km with $\tau = 0.1$ where $\alpha = 0.06$ and $\theta_{\odot} = 0^{\circ}$: CASE 3 and 4.	84
7.7	(i) Same as CASE 1 and CASE 2 of Figure 7.6 except that $\alpha = 0.40$ and $\theta_{\odot} = 0^{\circ}$	85
7.7	(cont'd) (ii) Same as CASE 3 and CASE 4 of Figure 7.6 except that $\alpha = 0.40$ and $\theta_{\odot} = 0^{\circ}$	86
7.8	(i) Same as CASE 1 and CASE 2 of Figure 7.6 except that $\alpha = 0.06$ and $\theta_{\odot} = 30^{\circ}$	87
7.8	(cont'd) (ii) Same as CASE 3 and CASE 4 of Figure 7.6 except that $\alpha = 0.06$ and $\theta_{\odot} = 30^{\circ}$	88

7.9	Retrieved source profile of CO ₂ for CASE 3 with associated profiles of error statistics for measurements with $\alpha = 0.06$ and $\theta_{\odot} = 0^{\circ}$	89
7.10	Same as Fig 7.9 except for CASE 4.	90
7.11	Retrieved source profile of CO ₂ with associated profiles of error statistics obtained by using both IR and NIR measurements in the presence of an aerosol layer at 2 km with $\tau = 0.2$ where $\alpha = 0.06$ and $\theta_{\odot} = 0^{\circ}$	95
7.12	Same as Figure 7.11 except that $\alpha = 0.40$ and $\theta_{\odot} = 0^{\circ}$	96
7.13	Same as Figure 7.11 except that $\alpha = 0.06$ and $\theta_{\odot} = 30^{\circ}$	97
7.14	Retrieved source profile of CO ₂ for CASE 2 with associated profiles of error statistics for measurements with $\alpha = 0.06$ and $\theta_{\odot} = 0^{\circ}$	98
7.15	Same as Fig 7.14 except for CASE 3.	99
A.1	Results of a speed comparison between the eigenmatrix method in Radiant and the doubling method.	121
A.2	Results of a speed comparison between Radiant and DISORT.	122

List of Tables

5.1	Diagonal elements of the covariance matrix S_a	36
6.1	Key for sensitivity plots.	39
6.2	Typical surface albedos for different surfaces in the $1.6\mu\text{m}$ spectral region.	40
7.1	Total degrees of freedom for CO_2 retrievals.	67
7.2	Column-average values of CO_2 volume mixing ratio for real, <i>a priori</i> , and retrieved profiles along with associated error for clear sky scenarios (see text for explanation).	71
7.3	Column-average values of CO_2 volume mixing ratio for real, <i>a priori</i> , and retrieved profiles along with associated error in scenarios with a thin cirrus layer.	80
7.4	Column-average values of CO_2 volume mixing ratio for retrieved profiles in CASE 3 and CASE 4 using measurements from the IR only, NIR only, and both along with associated error in scenarios with a thin cirrus layer when $\alpha = 0.06$ and $\theta_{\odot} = 0^\circ$	81
7.5	Column-average values of CO_2 volume mixing ratio for real, <i>a priori</i> , and retrieved profiles along with associated error in scenarios with a thin aerosol layer.	93

7.6	Column-average values of CO ₂ volume mixing ratio for retrieved profiles in CASE 2 and CASE 3 using measurements from the IR only, NIR only, and both along with associated error in scenarios with a thin aerosol layer when $\alpha = 0.06$ and $\theta_{\odot} = 0^{\circ}$	93
A.1	Sample of organizations or authors and some of their radiative transfer codes.	112
A.2	Comparison of upwelling radiances generated by Van de Hulst Table 35 (VDH), a doubling/adding scheme (D/A), and DISORT (D) with those generated by Radiant (R) for a given layer of different optical parameters.	119
A.3	Comparison of downwelling radiances generated by Van de Hulst Table 35 (VDH), a doubling/adding scheme (D/A), and DISORT (D) with those generated by Radiant (R) for a given layer of different optical parameters.	119
A.4	Comparison of radiances generated by a doubling/adding scheme (D/A) with those generated by Radiant (R).	120

Chapter 1

Introduction

1.1 Motivation for This Work

The issue of global warming has received much attention in the scientific community as well as the general populace in recent years. The recent trend of an increase in the average global temperature has provoked concern from more than a few worldwide. Along with this increased concern, numerous studies have addressed the potential influence of increased global temperatures and climate change on various aspects of life on Earth. Among these potential influences are sea ice and sea level (Timbal et al. (1995); Titus and Richman (2001)), ocean circulation (Thorpe et al., 2001), precipitation (Fowler and Hennessy, 1995), food production (Topp and Doyle (1996); Howden et al. (2001)), forests and vegetation (Kirschbaum (2000); Papadopol (2000)), wetlands and soil (Feddema (1999); Burkett and Kusler (2000)), and various fauna (e.g. Sorenson et al., 1998).

In addressing these concerns, the amount of CO₂ in the atmosphere is currently under great scrutiny. Since 1958, the concentration of CO₂ in the troposphere has been observed increasing at an average rate of 1.3 ppmv (parts per million per unit volume) per year (Tanaka et al. (1987); Lambert et al. (1995); Dettinger and Ghil (1998)) and as of 2000 had reached a level of approximately 370 ppmv (Keeling

and Whorf, 2001). Being a gas capable of absorbing infrared radiation that would otherwise vent to space, it is currently being examined for its potential influence on the earth's radiation budget and the change in climate that might result from its influence. Several studies have addressed the issue of the sensitivity of global climate to various parameters including CO₂ (e.g. Caldeira and Kasting (1993); Cess et al. (1993); Wuebbles et al. (1995); Manabe (1998); Cox et al. (2000); Meehl et al. (2000)).

In addition to some of the above concerns and uncertainties, there is much to learn about the overall carbon cycle itself for its own sake and the role it plays in Earth's natural processes. For example, there currently remains rather significant uncertainties as to the magnitude and location of sources and sinks of carbon dioxide on the planet. Given the potential seriousness of the global warming issue in general and humankind's current state of ignorance of the carbon cycle in particular, prudence demands that we in the atmospheric science community invest some time gaining a better understanding of both so (1) our knowledge of these particular aspects of Earth's systems is based on an adequate amount of data and sound science and (2) this certainty can be translated into giving the best possible information to policymakers when called upon.

As much as one might like to gain a better handle on the global warming issue and a better understanding of how CO₂ and the carbon cycle might be influencing it, the truth of the matter is that the carbon cycle problem is currently unconstrained due to the lack of available data. Current surface measurements are good, but lack the necessary scope to do the job (Gurney et al., 2002). Also, aircraft have been used in the past to measure CO₂, but the cost of getting the consistent needed coverage is also prohibitive.

What is required for this job is (1) a much more significant volume of quality data that can be used to help close the carbon cycle problem and (2) a more economical way of obtaining it. It appears the best way to obtain the volume of data needed for the overall cost is to place an instrument aboard a space-borne platform so

it could have access to most of the globe, provided that the resulting measurements are of sufficient precision. For example, Rayner and O'Brien (2001) hold that remote sensing of CO₂ from space can be of benefit if a precision of better than 2.5 ppmv (on an 8° x 10° satellite footprint) for monthly-averaged CO₂ column data can be achieved.

The above provides a backdrop for the present work. We now turn our attention to spotlight some of the efforts that have been made thus far to measure atmospheric CO₂ near the surface and aloft.

1.2 In Situ and Remote Measuring of Atmospheric CO₂

As far as surface measurements are concerned, there are currently some 65 surface sites around the globe from which CO₂ concentration data are obtained (e.g. see Figure 1.1). Although valuable data has been gathered from these sites, it is clear from the figure that there are vast regions where no data is being gathered.

In response to the spatial deficiencies of the current surface network, there have been proposals to measure CO₂ concentrations remotely via satellite. In considering such possibilities, two methods that present themselves are the remote sensing of CO₂ in the near infrared portion of the electromagnetic (EM) spectrum via absorption of reflected sunlight and in the far infrared portion of the spectrum via atmospheric emission.

To date, several studies have addressed the retrieval of concentrations of CO₂ in the atmosphere at various levels. For example, the work of Rinsland et al. (1992) focused on the region of the atmosphere between 70-120 km, Park (1997) on the region between 10-45 km, and Engelen et al. (2001) on the region between 0-20 km. In this last work, spectroscopic measurements from the far infrared (IR) were used in trying to bring closure to the carbon cycle problem.

Measurement Programs

NOAA CMDL Carbon Cycle Greenhouse Gases

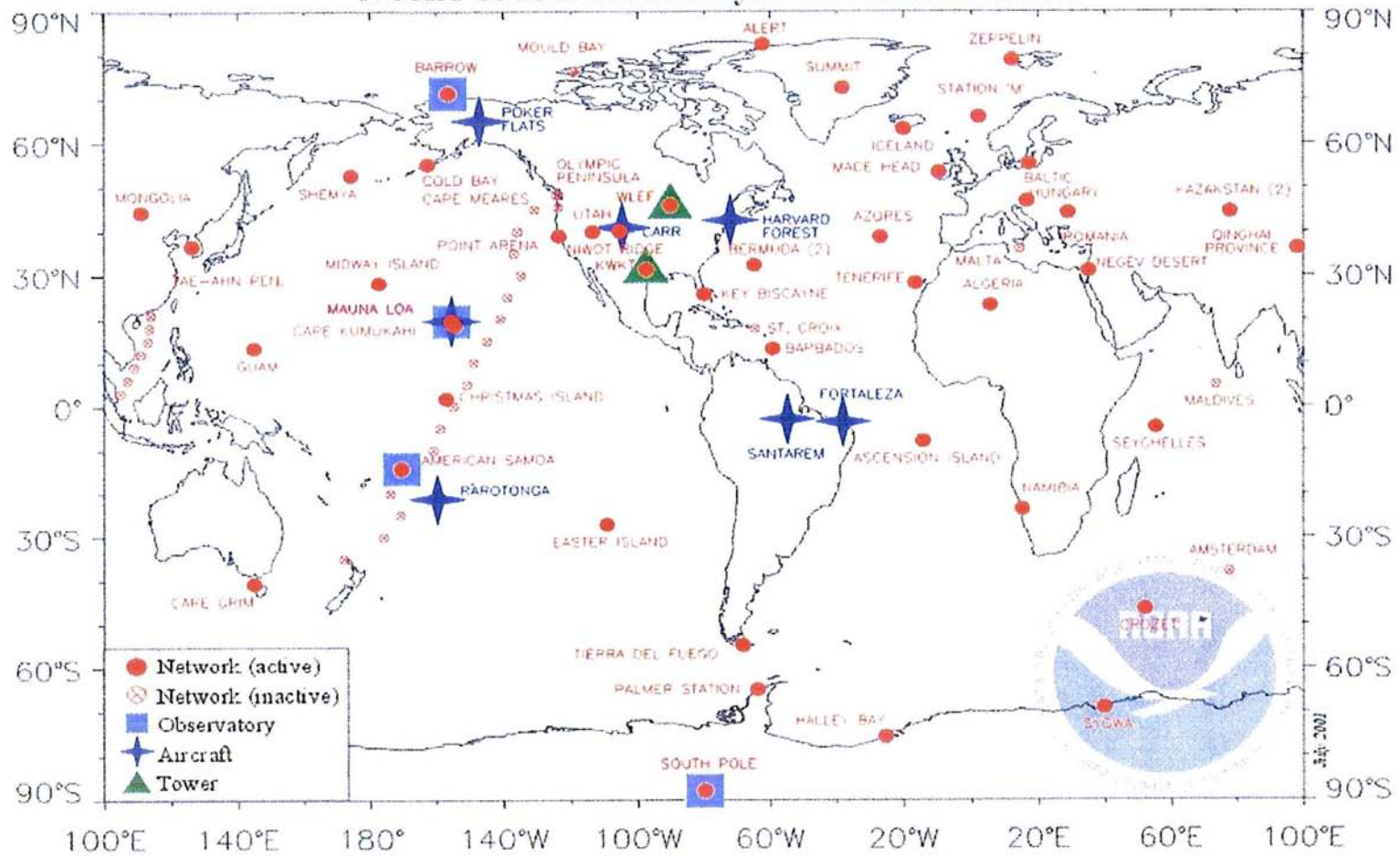


Figure 1.1: Global Greenhouse Sampling Network (Source: Climate Monitoring and Diagnostics Laboratory)

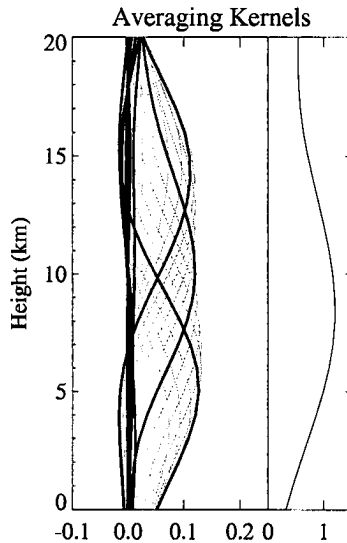


Figure 1.2: Averaging kernels from a CO₂ retrieval performed with simulated measurements from the far infrared only (See text for explanation). Reprinted from Engelen et al. (2001)

Since we are interested in obtaining profiles of CO₂ concentration in the lower atmosphere in general and values of concentration at the surface in particular, we will focus on this last region. However, one of the problems encountered in working in this region, as Engelen et al. (2001) illustrate, is having to contend with surface emission. There is not much contrast between the emission of infrared radiation from the lower atmosphere and its emission from the surface. As a result, the information in bands such as the 15 μm region originates largely from above 5 km with errors in the retrieved values of CO₂ increasing as one descends the the surface (see Figure 1.2). The lefthand side of the figure displays the averaging kernels for the IR retrieval. These provide a measure of the spatial resolution of the IR observing system. The righthand side of the figure indicates how much the CO₂ retrieval performed was relying on the measurements at each height where a value of ≈ 1 indicates primary reliance on the measurements and values less than 1 indicating more reliance on prior information of the atmospheric state (more on this later).

The quest of trying to achieve concentrations of CO₂ in the lower atmosphere using reflected radiation in the near infrared (NIR) however is also one of good news

and bad news. In order to have a reasonable chance of success, one must be able to obtain signals from surfaces whose returns are strong and whose reflective characteristics are fairly well known. In regards to this, land surfaces usually yield fairly decent returns, but have reflective characteristics that are not as precisely known. Conversely, ocean surfaces have reflective characteristics which are more uniform on the whole, but generally don't yield as good a return as their terrestrial counterparts. This is generally true except for one ocean region: a region in which the ocean surface acts as a "rough" mirror and produces sunglitter. Here, if an observer is positioned correctly, the observed signal return from the ocean surface can be several times greater than if the observer is not positioned to receive this direct reflection.

In addition to surface considerations, one must contend with such atmospheric phenomena as absorption and scattering by clouds and aerosol. On the one hand, if only measurements obtained from clear regions are used, most of this problem disappears. On the other hand, there are some clouds which do not yield easily to detection. Thin cirrus (cirrus clouds with an optical thickness $\tau \leq 0.2$) are of this nature. In addition to the scattering produced by ice crystals in these optically thin clouds, the absorption and scattering produced by optically thin aerosol can also potentially wreak havoc on attempts to retrieve CO₂ using reflected sunlight.

That is where this work comes in. The purpose of this work is to investigate, in a preliminary way, the possible benefit of using space-based spectral measurements from both the near and far infrared portions of the EM spectrum to see if (1) retrieved profiles of CO₂ concentration in the lower atmosphere reproduce the general characteristics of the the corresponding true profiles under different conditions and (2) the resulting column-averaged values of CO₂ are of sufficient precision to assist in bringing closure to the carbon cycle problem.

The results of this study show that the measurements from the near and far infrared work in a complementary fashion in retrieving profiles of CO₂ in the lower atmosphere. For each retrieval scenario, a general *a priori* profile of CO₂ concentration

is used to assist in constraining the measurements. Results indicate a precision in the CO₂ column-averaged values of better than 1 ppmv for the clear sky cases run.

Results also indicate a column-averaged value of better than 2.5 ppmv for the majority of cases ($\approx 73\%$) with a layer of thin cloud or aerosol present for an initial retrieval over a given locale *provided there exists a means of detecting the height of the scattering layer to 1 km and the optical depth of the scattering layer to 10%*. However, given the ability to detect the scattering layer, there is good reason to anticipate even better results once a number of retrievals are performed and the *a priori* tuned to a given locale using the results of previous retrievals.

Recalling the previously mentioned work of Rayner and O'Brien (2001), it is estimated that the errors in resulting monthly-averaged column-average values of CO₂ from any such retrievals need to be less than 2.5 ppmv to be useful to researchers attempting to determine the location and magnitude of CO₂ surface sources and sinks. If space-based measurements are to be useful in estimating CO₂ over the approximately 50% of the earth where thicker clouds do not occur each day, it appears that measurements in addition to the near and far infrared used in this work will be needed to mitigate the effects of scatter by the optically thin cirrus and aerosol which cover an estimated 20-30% of the remaining 50% of Earth.

1.3 Looking Ahead

We begin this study in chapter 2 by considering the absorption bands of CO₂ in both the near and far infrared and, in particular, one in the near infrared suitable to retrieve concentrations of CO₂ in the lower atmosphere. Following this, parameterizations used to simulate the absorption and scattering processes in the atmosphere are described in chapter 3.

Chapter 4 provides a sketch of the two methods and models used to simulate the measurements in the near and far infrared regions of the spectrum. Along with

this, some detail of a brand new and efficient multi-stream radiative transfer model called Radiant is provided. An emphasis is made on some of the strengths it possesses over the more established doubling/adding method and the more traditional use of the eigenmatrix method as implemented by the widely used radiative transfer code DISORT ("Discrete Ordinate Method for Radiative Transfer").

The retrieval method is subsequently elaborated on in chapter 5, both generally and how it is applied here to retrieving profiles of CO₂ concentration. Chapter 6 sheds light on the expected sensitivities of NIR spectroscopic measurements to thin cloud and aerosol as well as their sensitivities to CO₂ under varying scenarios of surface albedo and solar zenith angle. The results of retrievals performed using the simulated measurements from the IR and NIR are revealed in chapter 7 along with their implications for performing retrievals in the future using a spaceborne instrument. To the author's knowledge, this is the first time measurements from both the near and far infrared have been brought together to obtain profiles of CO₂ concentration and represents original work.

Chapter 2

Absorption Bands of CO₂ in the Near Infrared

Carbon dioxide possesses a number of absorption bands in both the far infrared (IR) and near infrared (NIR) regions of the EM spectrum. In the IR, these bands are centered at 4.3, 5.0, 10.0 and 15.0 μm - the one at 15 μm being the strongest. In the NIR, bands can be found centered at 1.4, 1.6, 2.0, and 2.7 μm with the one at 2.7 being the strongest.

Since one purpose of this study is to assess the value of measurements from the NIR using reflected sunlight to retrieving atmospheric CO₂, we will confine our discussion at the moment to the NIR portion of the spectrum. Also, since the focus is on retrieving CO₂ in the lower atmosphere, the use of bands that will not quickly saturate is desired. Now, since the band at 2.7 μm exhibits absorption that is strong in the NIR, it is disqualified for this application (the sun's radiation is also waning at these wavenumbers, thus yielding an input signal that is undesirably small). Also, since the CO₂ band at 1.4 μm is located in a region of strong water vapor absorption, it too is disqualified.

Hence, we turn our attention to the two remaining CO₂ absorption bands that remain as candidates for this job. These are the bands centered at 1.6 and 2.0 μm

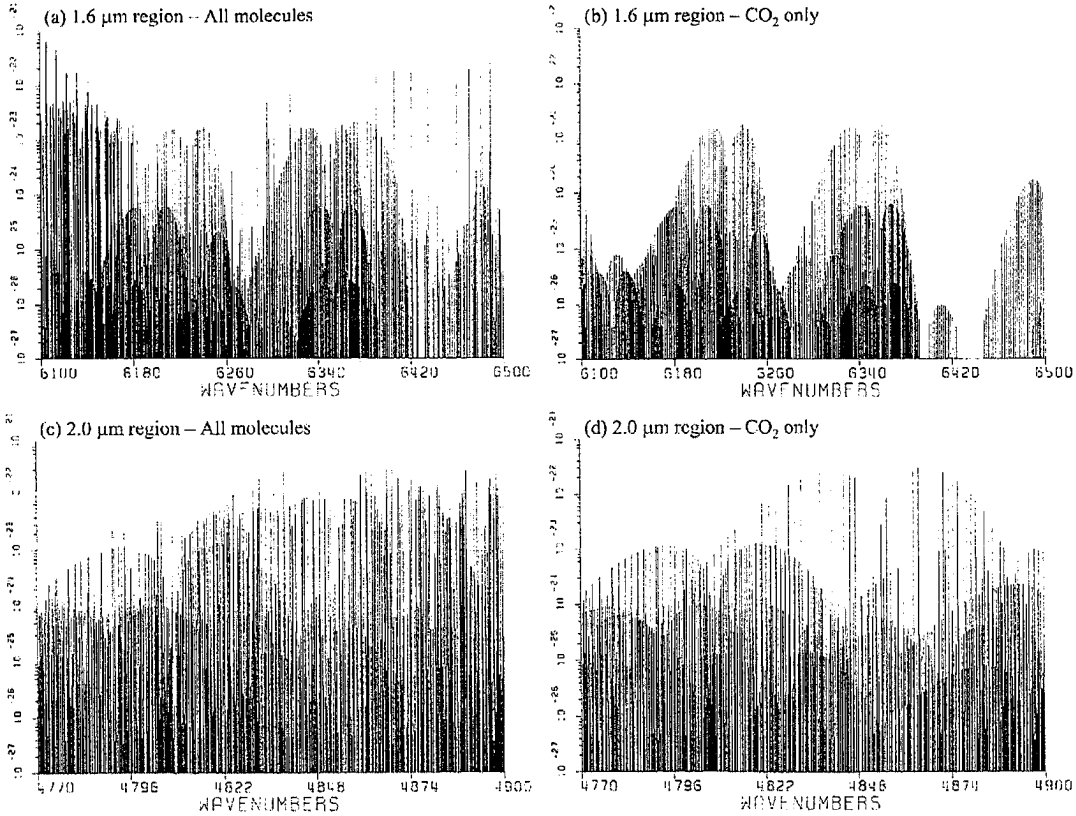


Figure 2.1: Absorption bands of CO_2 located in the NIR at $1.6 \mu\text{m}$ ((a) and (b)) and $2.0 \mu\text{m}$ ((c) and (d)). (a) and (c) show the CO_2 absorption lines along with those of other molecules in these respective regions while (b) and (d) show CO_2 alone.

and are pictured in Figure 2.1. The spectra depicted were produced by transition line data in the 1996 High-Resolution Transmission Molecular Absorption Database (HITRAN96). Inspection of part (c) of the figure reveals that the CO_2 absorption lines at $2.0 \mu\text{m}$ also suffer from water vapor absorption, though not as badly as $1.4 \mu\text{m}$. Although more weakly absorbing than water vapor, absorption lines of ammonia, hydroxide, and hydrogen bromide also accompany CO_2 in this band (also shown). Part (d) shows CO_2 alone in this region.

In contrast, the $1.6 \mu\text{m}$ band of CO_2 sits in a valley between two water vapor bands; hence, measured radiances are unaffected by absorption due to this highly variable atmospheric constituent. Part (a) of Figure 2.1 shows the CO_2 absorption lines in this region along with absorption lines of water vapor, methane, oxygen,

carbon monoxide, hydroxide, and hydrogen bromide. Part (b) displays CO₂ by itself for this region.

Hence, of the four absorption bands of CO₂ in the NIR, the one centered at 1.6 μm is the most promising for our purposes. It is lines from this band in the NIR that will be used to attempt to retrieve concentrations of CO₂ in the lower atmosphere.

Chapter 3

Atmospheric Absorption and Scattering

Upon entering the Earth's atmosphere after their 93 million mile journey, photons from the sun begin to experience attenuation as they traverse it. This activity takes place through one of two processes: out-scattering and absorption. Out-scattering is the process by which photons are scattered out of the path they had when they first entered a medium. Like a giant pinball machine, the earth's atmosphere serves to redirect photons of incident radiation.

The other process is the absorption of photons by cloud or gas. Depending on the particle or gas, photons are selectively absorbed: some photons are unaffected as they encounter certain constituents, while others are absorbed at one wavelength and re-emitted at another and continue on after their brief stay with these atmospheric residents. In this chapter, the various parameterizations used to model these processes that affect the photons as they make their journey through the atmosphere are described.

3.1 Rayleigh Scattering

Rayleigh scattering describes the symmetric scattering that occurs when a wavelength of incident radiation is large in comparison to the size of the particle or molecule it strikes. The type of scatter can be defined in relation size parameter $x = \frac{2\pi r}{\lambda}$ where r is the effective radius of the particle and λ is the wavelength of the impinging radiation. For spherical particles of radius r , if $x \ll 1$, then the scattering falls within the Rayleigh regime.

In the atmosphere, visible and infrared light is scattered predominantly by oxygen and nitrogen due to the diatomic nature of these molecules. Because these atoms are joined together by strong covalent bonds (two in the case of oxygen and three in the case of nitrogen), they are spectrally inert: incoming solar radiation is scattered rather than absorbed.

The probability that radiation is scattered in a particular direction due to Rayleigh scattering is given by the Rayleigh phase function

$$P(\cos\Theta) = \frac{3}{4}(1 + \cos^2\Theta) \quad (3.1)$$

where Θ is the scattering angle (the angle between the incident and reflected radiation). This type of scattering is illustrated in Figure 3.1.

To compute the Rayleigh scattering coefficient σ_s for radiative transfer computations, one can use the following empirical expression from Paltridge and Platt (1976) and Marggraf and Griggs (1969) to compute the Rayleigh optical depth τ_{ray} as

$$\tau_{ray} = 0.0088\lambda^{0.2\lambda-4.15}e^{-0.00116z^2-0.1188z} \quad (3.2)$$

where z is the height above sea level and λ is the wavelength at which τ_{ray} is being determined. In general, the optical depth τ is defined in relation to geometric length as $\tau = \int \sigma_e ds$. Thus, τ is determined both by the physical distance s through which

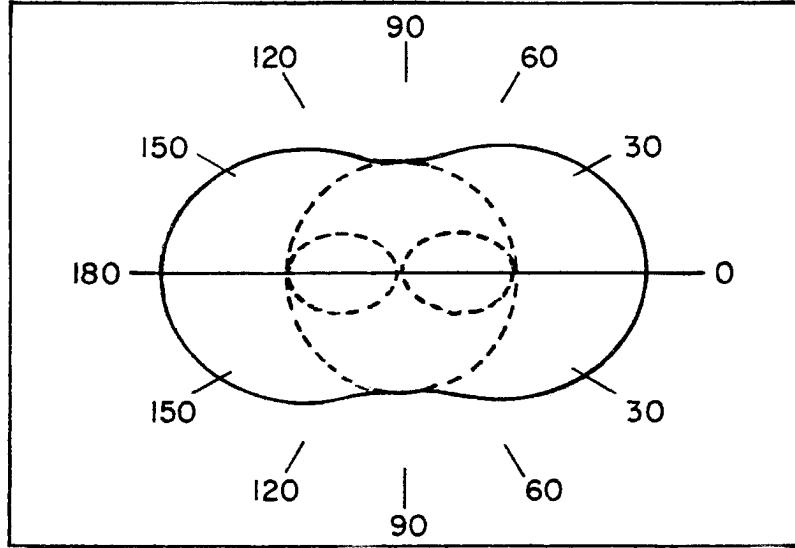


Figure 3.1: Scattering pattern corresponding to Rayleigh scatter.

a photon must pass in a given medium as well as the amount and effectiveness of absorbing and scattering material that it meets in its path (as quantified by the extinction coefficient σ_e). If one takes the derivative of this expression where σ_e is constant (as for a layer considered homogeneous at constant pressure), then σ_e can be computed by $\frac{\Delta\tau}{\Delta s}$ after using (3.2). Since the extinction is defined as the sum of both the absorption and scattering by constituents ($\sigma_e = \sigma_a + \sigma_s$ where σ_a is the absorption coefficient) and here there is no absorption, $\sigma_e = \sigma_s$. Assuming that the layer is homogeneous, upon applying (3.2) at two different atmospheric heights z to obtain the corresponding values of τ at those levels, one can use $\sigma_s = \sigma_e = \frac{\Delta\tau}{\Delta z}$ to obtain the coefficient due to Rayleigh scatter required for radiative transfer computations.

3.2 Absorption and Scattering by Clouds and Aerosol

Absorption and scattering by clouds is a complex process - being influenced by whether the constituents are water droplets or ice crystals (or both). If the cloud

contains water droplets alone, then the size of the droplets and their distribution becomes an issue. If the cloud contains ice crystals, then their size and shape become an issue also. Fortunately, clouds can be avoided for the most part so as to provide the best possible measurement of the CO₂ in an atmospheric column. From an operational point of view, if the measuring instrument is on board a satellite, only those pixels determined to be clear would be used. Of course, there are limits to which clouds can be detected and it is possible for clouds such as thin cirrus to go undetected. The potential influence of such undetected clouds will be studied in chapter 6.

The absorption and scattering by aerosol is also a complex process, the amount of scattering and absorption being influenced by the size, shape, and composition of the aerosol under consideration as well as whether it is dry or not. Again, for this study, aerosol plumes will be expressly avoided so as to provide the best possible measurement of the CO₂ in an atmospheric column and again only those pixels determined to be clear would be used. Like the case of thin cirrus however, it is possible for a thin aerosol layer to go undetected. This issue will also be taken up in chapter 6.

3.3 Absorption by Atmospheric Gases

The definition of optical depth can be rendered more appropriate for an atmospheric gas by expressing it as

$$\tau = \int k du \tag{3.3}$$

or for a homogeneous layer at a given wavenumber as

$$\tau = ku \tag{3.4}$$

where k is the gaseous absorption coefficient (with a wavenumber dependence that is understood but for simplicity has not been denoted here) and $u = \int du$ is the optical path of the gas. Unlike the optical depth τ , which is unitless, the optical path u often assumes units of mass per unit area.

The absorption coefficient k in turn can be described by

$$k = Sf(\nu - \nu_o) \quad (3.5)$$

where S is the strength of the absorption line of the gas at a given pressure and temperature and f is a function describing how the absorption line width of the gas changes with temperature and pressure (i.e. the line profile). The line strength S has a temperature dependence of the form (Liou, 1992)

$$S(T) = S(T_o) \left(\frac{T_o}{T}\right)^n \frac{1 - e^{-hc\nu_o/KT}}{1 - e^{-hc\nu_o/KT_o}} e^{-\frac{hcE_i}{K} \left(\frac{1}{T} - \frac{1}{T_o}\right)} \quad (3.6)$$

where T and T_o are actual and reference temperatures, h is Planck's constant, c is the speed of light, ν_o is the wavenumber at which the line strength is being computed, K is Boltzmann's constant, and E_i is the energy of the lower state of the transition.

As for the computation of the line profile, the answer will depend on where one is located in the atmosphere. If one is above 50 km, then the broadening of lines is primarily due to Doppler influences. The profile in this case can be described by the Doppler profile (Liou, 1992)

$$f_D(\nu - \nu_o) = \frac{1}{\alpha_D \sqrt{\pi}} e^{-\frac{(\nu - \nu_o)^2}{\alpha_D^2}} \quad (3.7)$$

where

$$\alpha_D = \frac{\nu_o}{c} \sqrt{2RT} \quad (3.8)$$

is the Doppler halfwidth. Here, ν_o is again the wavenumber for which the absorption coefficient is being computed, ν is the wavenumber where an absorption line is located

whose influence on the absorption at ν_o is being considered, c is the speed of light, R is the gas constant of the gas under consideration, and T is the temperature at the particular altitude in the atmosphere.

Below about 20 km in the atmosphere, the broadening of lines is primarily due to pressure influences. The profile in this case can be described by the Lorentz profile

$$f(\nu - \nu_o) = \frac{1}{\pi} \frac{\alpha}{(\nu - \nu_o)^2 + \alpha^2} \quad (3.9)$$

where

$$\alpha = \alpha(p, T) = \alpha_o \frac{p}{p_o} \left(\frac{T_o}{T}\right)^n \quad (3.10)$$

is the Lorentz halfwidth due to variations in pressure and temperature. Here, ν and ν_o are the same as in the Doppler case with p and T the pressure and temperature at the particular altitude in the atmosphere and p_o and T_o the pressure and temperature at a reference altitude. Here, n is the temperature exponent for the gas under consideration at wavenumber ν .

Finally, if one is somewhere between 20 and 50 km in the atmosphere, the broadening of lines is influenced by both Doppler and pressure effects and is appropriately described as a convolution or "smearing" of the two. What results is a profile known as the Voigt profile. It can be described theoretically as

$$f_V(\nu - \nu_o) = \int_{-\infty}^{\infty} f(\nu' - \nu_o) f_D(\nu' - \nu) d\nu' \quad (3.11)$$

For operational purposes, a numerically efficient expression for the Voigt profile is normally used. In this study, we will use the expression found in Liou (1992) which has its roots in the work of Matveev (1972). It is given by

$$\begin{aligned}
f_V(\nu - \nu_o) = & \sqrt{\frac{\ln 2}{\pi}} \frac{1}{\alpha_V} (1 - \xi) e^{-\eta^2 \ln 2} \\
& + \frac{1}{\pi \alpha_V} \xi \frac{1}{1 + \eta^2} - \frac{1}{\pi \alpha_V} \xi (1 - \xi) \left(\frac{1.5}{\ln 2} + 1 + \xi \right) \\
& \left(0.066 e^{-0.4 \eta^2} - \frac{1}{40 - 5.5 \eta^2 + \eta^4} \right)
\end{aligned} \tag{3.12}$$

where

$$\alpha_V = 0.5 \left(\alpha + \sqrt{\alpha^2 + 4 \ln 2 \alpha_D^2} \right) + 0.05 \alpha \left(1 - \frac{2 \alpha}{\alpha + \sqrt{\alpha^2 + 4 \ln 2 \alpha_D^2}} \right) \tag{3.13}$$

is the Voigt halfwidth, $\xi = \alpha/\alpha_V$, and $\eta = (\nu - \nu_o)/\alpha_V$. According to Matveev, this formulation is generally accurate to within 3% of values generated by using the definition in (3.11). Since the Voigt profile takes into account both effects, it is the above expression that will be used to compute the absorption coefficient k for CO₂ at the NIR wavenumbers employed in this work.

Chapter 4

Radiative Transfer and the Forward Models

4.1 Radiative Transfer Theory

The essence of radiative transfer (RT) theory can be described by equation (4.1) and Figure 4.1. The term on the lefthand side of equation (4.1) describes the change in intensity of radiation (I) as it travels through a volume of space in a given medium. On the right side, μ_{\odot} is the cosine of the solar zenith angle, σ_e , σ_s , and σ_a are the extinction, scattering, and absorption coefficients, respectively, P is the scattering phase function, and B is the Planck function of emission. The terms on the right side can be interpreted as follows:

$$\begin{aligned} \mu \frac{dI(z, \mu, \phi)}{dz} = & -\sigma_e(z)I(z, \mu, \phi) \\ & + \frac{\sigma_s(z)}{4\pi} \int_0^{2\pi} \int_{-1}^1 P(z, \mu, \phi, \mu', \phi') I(z, \mu', \phi') d\mu' d\phi' \\ & + \frac{F_{\odot}}{4\pi} \sigma_s(z) P(z, \mu, \phi, \mu_{\odot}, \phi_{\odot}) e^{-\sigma_e(z_T - z)/\mu_{\odot}} \\ & + \sigma_a(z) B(T(z)) \end{aligned} \quad (4.1)$$

1st term - The attrition of photons that radiation undergoes due to absorp-

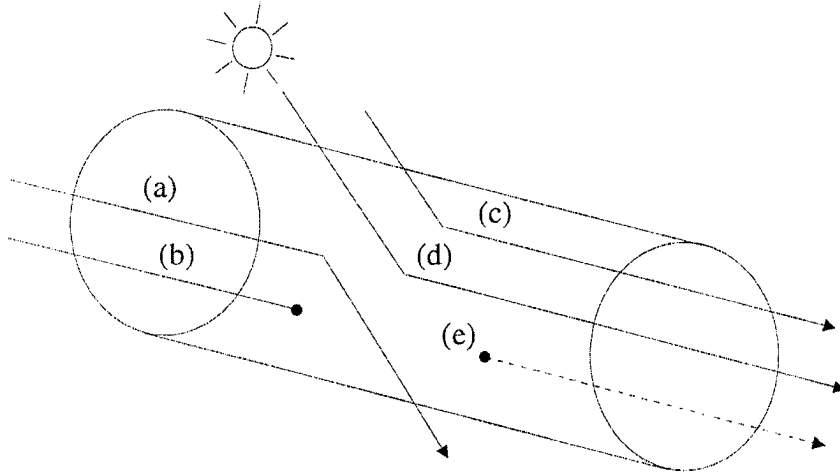


Figure 4.1: Physical processes affecting the transfer of radiation through a medium. These processes are (a) out-scattering, (b) absorption, (c) and (d) in-scattering of diffuse and direct radiation, respectively, and (e) emission.

tion and out-scattering (the scattering of a photon **out** of the path it had when it first entered a volume of space). Again, the absorption and out-scattering together comprise what is commonly referred to in RT circles as the extinction. See *a* and *b* in Figure 4.1 for a depiction of out-scattering and absorption, respectively.

2nd and 3rd terms - The accumulation of photons that radiation experiences due to in-scattering (the scattering of photons from different directions **into** the path of the incident radiation being considered). The second term is associated with the in-scattering of diffuse radiation, whereas the third term is associated with the in-scattering from a direct source (in this case, the sun). These processes are depicted by *c* and *d* in Figure 4.1.

4th term - The addition of photons that radiation experiences due to the emission of photons by particles or gases within the medium into the direction of the incident radiation. In Figure 4.1, this is depicted by *e*.

4.2 Forward Model for the Near Infrared

An overall description of the method used to compute radiances in the NIR model is now described. A method of solving the equation of transfer (4.1) involves replacing the integrals in the equation by finite sums, thereby producing a discrete form of the equation. By using a quadrature scheme such as Gaussian or Lobatto quadrature, if one expresses the phase function $P(z, \mu, \phi, \mu', \phi')$ as the sum of a suitable number of orthogonal polynomials, Legendre polynomials for instance, the integrals in (4.1) are exact. The number of discrete equations which are required to represent the radiation field will depend on the number of terms required to represent the phase function. For example, if the number of terms required to represent the phase function is N , then it will take $2n \geq N + 1$ equations when using Gaussian quadrature or $2n \geq N + 3$ equations when using Lobatto quadrature to represent the radiation field and allow the integrals to be computed exactly. Here, N is assumed to be odd and n is the number of upward (or downward) streams used to describe the radiation field.

The radiance I can be described by the Fourier expansion

$$I(z, \mu, \phi) = \sum_{m=0}^M I_m(z, \mu) \cos[m(\phi - \phi_{\odot})] \quad (4.2)$$

where z is altitude, μ is the cosine of the observation angle in reference to zenith, and ϕ and ϕ_{\odot} are the azimuth angle of the radiance and the sun, respectively, with respect to a given coordinate system.

The system of scalar equations resulting from the above discretization process of (4.1) can be expressed as set of matrix equations, one for each m in the Fourier expansion of I :

$$\begin{aligned}
\frac{d^m I^\pm}{dz} &= \mp \sigma_e (M^{-1}) ({}^m I^\pm) \\
&\pm (1 + \delta_{0m}) \frac{\sigma_s}{4} [(M^{-1}) ({}^m P^\pm) C ({}^m I^+) + (M^{-1}) ({}^m P^\mp) C ({}^m I^-)] \\
&\pm \frac{\sigma_s}{4\pi} F_\odot (M^{-1}) ({}^m P_\odot^\mp) e^{[-\sigma_e (z_T - z) / \mu_\odot]} \\
&\pm \sigma_a (M^{-1}) ({}^m Y) B(T(z))
\end{aligned} \tag{4.3}$$

Here, we have:

${}^m I^\pm$ - A vector describing the m th term in the Fourier expansion of I where

(+) represents that portion of the vector representing upwelling radiances and (-) that portion representing downwelling radiances.

${}^m P^\pm$ and ${}^m P_\odot^\pm$ - The phase function matrices for the forward (+) and backward (-) scattering of diffuse and direct radiation, respectively.

M^{-1} - A matrix consisting of the reciprocals of quadrature roots.

C - A matrix of quadrature weights.

${}^m Y$ - A vector of unity for $m = 0$ and a vector of zeros otherwise.

$B(T(z))$ - The Planck function (assumed constant within a layer).

σ_a - The absorption coefficient of the medium.

σ_e - The extinction coefficient of the medium.

δ_{0m} - The Kronecker delta.

F_\odot - The solar flux incident at the top of the medium.

$T(z)$ - The temperature at altitude z .

μ_\odot - The cosine of the solar zenith angle.

The set of equations represented by (4.3) can be rendered more compact in the following matrix equation

$$\frac{d}{dz} \begin{bmatrix} {}^m I^+ \\ {}^m I^- \end{bmatrix} = \begin{bmatrix} \hat{t}^m & -\hat{r}^m \\ \hat{r}^m & -\hat{t}^m \end{bmatrix} \begin{bmatrix} {}^m I^+ \\ {}^m I^- \end{bmatrix} + \begin{bmatrix} {}^m \hat{\Sigma}^+ \\ -{}^m \hat{\Sigma}^- \end{bmatrix} \tag{4.4}$$

where

$$\hat{t}^m = -\sigma_e(M^{-1}) + (1 + \delta_{om})\frac{\sigma_s}{4}[(M^{-1})({}^mP^+)C] \quad (4.5)$$

$$\hat{r}^m = -(1 + \delta_{om})\frac{\sigma_s}{4}[(M^{-1})({}^mP^-)C] \quad (4.6)$$

are matrices describing the local transmission and reflection properties of a given layer in the medium (i.e. the layer's intrinsic scattering properties) and

$${}^m\hat{\Sigma}^+ = \frac{\sigma_s}{4\pi}F_{\odot}(M^{-1})({}^mP_{\odot}^-)e^{[-\sigma_e(z_T-z)/\mu_{\odot}]} + \sigma_a(M^{-1})({}^mY)B \quad (4.7)$$

$${}^m\hat{\Sigma}^- = \frac{\sigma_s}{4\pi}F_{\odot}(M^{-1})({}^mP_{\odot}^+)e^{[-\sigma_e(z_T-z)/\mu_{\odot}]} + \sigma_a(M^{-1})({}^mY)B \quad (4.8)$$

are vectors describing sources of upwelling and downwelling radiation within the medium, respectively. Finally, denoting the matrix of local transmission and reflection functions by A and the radiance and source vectors by I and Σ , respectively, we arrive at the more concise expression

$$\frac{d}{dz}I = AI + \Sigma \quad (4.9)$$

where a dependence on m is understood. The above system of differential equations described by this matrix equation has the formal solution

$$I = e^{A\sigma_e H}I_o + \int_0^H \sigma_e e^{A\sigma_e(H-z)}\Sigma dz \quad (4.10)$$

where H is a fixed altitude above sea level.

The above solution can be obtained in a rather efficient manner by employing what is sometimes referred to as the interaction principle. The essence of this principle is displayed in Figure 4.2.

The upwelling radiances, $I^+(H)$ and $I^+(0)$, and the downwelling radiances, $I^-(H)$ and $I^-(0)$, can be expressed as combinations of global transmission and reflection matrices and source vectors ($T(H, 0)$, $T(0, H)$, $R(H, 0)$, $R(0, H)$, $S(H, 0)$, and

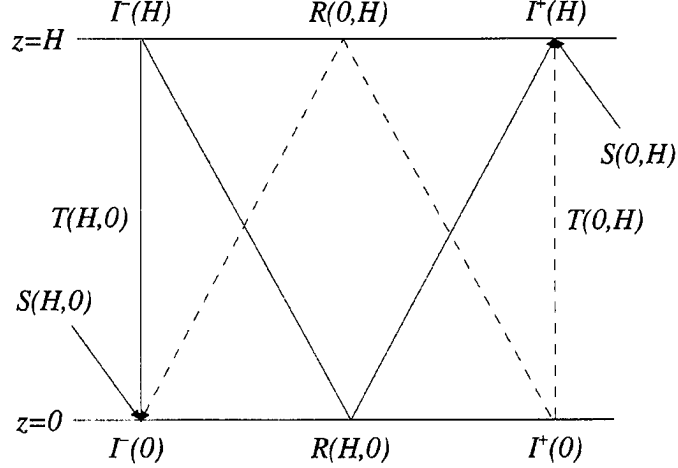


Figure 4.2: The interaction principle illustrated for a homogeneous layer where $T(H,0)$ and $R(H,0)$ are the downwelling global transmission and reflection matrices and $T(0,H)$ and $R(0,H)$ their upwelling counterparts. $S(H,0)$ is the downwelling source vector and $S(0,H)$ the upwelling source vector, respectively.

$S(0,H)$). Whereas the local transmission and reflection matrices and source vectors describe only the intrinsic scattering properties of the medium, these matrices account for both its intrinsic properties as well as its geometric thickness. Using the interaction principle and these matrices, the radiances can be expressed algebraically as

$$I^+(H) = T(0,H)I^+(0) + R(H,0)I^-(H) + S(0,H) \quad (4.11)$$

$$I^-(0) = R(0,H)I^+(0) + T(H,0)I^-(H) + S(H,0) \quad (4.12)$$

After some rather involved algebra to promote both numerical stability and efficiency, the eigenvalues and eigenvectors of the eigenmatrices in the matrix form of equation (4.10) are obtained. Upon rearranging equations (4.11) and (4.12) to express the outgoing radiances $I^+(H)$ and $I^-(0)$ in terms of the incoming radiances $I^+(0)$ and $I^-(H)$, one can compare the resulting expressions with the matrix form of (4.10) and obtain a form for the required global transmission and reflection matrices and source vectors to obtain the solution to the radiative transfer equation. It was this method that was used to generate the simulated measurements in the NIR model. For further

details on this method and model, see appendix A.

4.3 Forward Model for the Infrared

The forward model used to describe the influence of nature on wavelengths of light in the IR portion of the spectrum and produce the resulting simulated IR measurements is the same used by Engelen et al. (2001) with earlier versions given in Engelen and Stephens (1997) and Engelen and Stephens (1999). The IR forward model uses a Malkmus band model to obtain the transmission and resulting optical depth produced by different atmospheric gases. In this study, potential influences of CO₂, H₂O, and O₃ were considered.

Here, the solution to the radiative transfer equation given in (4.10) can be rendered

$$I_\nu(0, \mu) = B_\nu(T_s)e^{-\tau_s/\mu} + \int_0^{\tau_s} B_\nu(T)e^{-\tau/\mu}\mu^{-1}d\tau \quad (4.13)$$

where $I_\nu(0, \mu)$ is the upwelling radiance at the top of the atmosphere, $B_\nu(T)$ is the Planck radiance at wavenumber ν and temperature T , μ is the cosine of the solar zenith angle, and τ is the optical depth.

In this region, the transmission is determined by

$$Tr(\tau) = \frac{1}{\Delta\nu} \int \Delta\nu e^{-\tau\nu} d\nu \quad (4.14)$$

where the transmission is integrated over a 1 cm⁻¹ spectral interval. Using the Malkmus band model, the transmission can be rendered analytically as

$$Tr(u) = \exp\left[-\frac{\pi\alpha_L}{2\delta} \left(\sqrt{1 + \frac{4Su}{\pi\alpha_L}} - 1\right)\right] \quad (4.15)$$

where S is the average line intensity, α_L is the average Lorentz line width, and δ is the average absorption line spacing.

The Malkmus transmission can be determined once values of S , α_L , and δ are given. S and α_L are obtained by using absorption data and demanding agreement in the strong and weak-line limits. Using this renders the transmission as

$$Tr(u) = exp[-\frac{2X^2}{Y\Delta\nu}(\sqrt{1 + \frac{Y^2u}{X^2}} - 1)] \quad (4.16)$$

where

$$X = \sum_{i=1}^N \sqrt{S_i \alpha_i} \quad (4.17)$$

$$Y = \sum_{i=1}^N S_i \quad (4.18)$$

are the so-called strong and weak line limits. In this model, X and Y were determined through least-squares fitting to data from the HITRAN96 database. This was done because using the above expressions in (4.17) and (4.18) directly provide parameters that suffer accuracy (Lacis and Oinas, 1991).

Making these substitutions in (4.13), it becomes

$$I(0, \mu) = B(T_s)Tr(\tau_s) + \int_0^{\tau_s} B(T)Tr(\tau)\mu^{-1}d\tau \quad (4.19)$$

where $I(0, \mu)$ is the radiance for a given 1 cm^{-1} spectral interval. In this work, nadir soundings are used, thus yielding a value of $\mu = 1$. Unlike Engelen et al. (2001), the Jacobians needed for retrieving CO_2 were produced by finite differences to assist in assimilating the IR model in the retrieval scheme.

Chapter 5

Retrieving Atmospheric Parameters: Theory and Application to CO₂

5.1 Retrieval Theory

For this study, simulated radiances taken at the top of the atmosphere from both the IR and NIR are used to retrieve a profile of CO₂ in the lower atmosphere. The relationship between these measurements and the CO₂ can be expressed as

$$y = f(x, b) + \epsilon_y \quad (5.1)$$

where y is a vector of measured radiances, f is the relation established by the physics of nature between y and the atmospheric state vector x (here, a profile of CO₂), b represents parameters that are not being retrieved (e.g. other atmospheric gases), and ϵ_y is a vector of error in the measurements.

Of course, f is not perfectly known and must be approximated by a forward

model which we will call F . With this, (5.1) becomes

$$y = F(x, b') + \epsilon_y + \epsilon_F = F(x, b') + \epsilon \quad (5.2)$$

where b has been replaced by an approximation b' and ϵ_F is a vector of error due to approximations made or processes ignored or unknown in nature's relation f that are inherent in the forward model F . Following this, ϵ will be used to denote the combined error of both the measurements (ϵ_y) and the forward model (ϵ_F).

In theory, one need only invert (5.2) to retrieve the current atmospheric state vector x ; however, due to the nature of the radiative transfer equation, the whole process becomes problematic as it is highly ill-conditioned. Thus, the errors ϵ_y and ϵ_F can be amplified to such an extent as to render the retrieval useless. To combat this problem, prior information about the state vector x is used to assist in constraining the retrieval where needed. This *a priori* information is introduced in the form of an *a priori* profile x_a .

Using Bayes' theorem and assuming that the *a priori* and the errors in the measurement and model are normally distributed, the solution to the inversion problem can be obtained by minimizing the cost function (Rodgers, 2000)

$$J = [y - F(x)]^T S_\epsilon^{-1} [y - F(x)] + [x - x_a]^T S_a^{-1} [x - x_a] \quad (5.3)$$

where S_ϵ is the covariance matrix associated with the measurement and model error, S_a a covariance matrix associated with the *a priori*, and where the b notation has been dropped for simplicity of expression. Using Newton's method for nonlinear systems and assuming the problem is not terribly nonlinear in F , one can obtain the following expression for iteration (Rodgers, 2000):

$$x_{i+1} = x_a + (S_a^{-1} + K_i^T S_\epsilon^{-1} K_i)^{-1} K_i^T S_\epsilon^{-1} [y - F(x_i) + K_i(x_i - x_a)] \quad (5.4)$$

where the K matrix is the so-called Jacobian which indicates the sensitivity of the measurements to the parameter(s) being retrieved at the measuring wavenumbers (in this case CO_2). The i notation on the K matrix and x vector indicate those associated with the i th iteration of the method.

As mentioned earlier, the errors in the retrieval can be characterized by the variances associated with both the measurement and model error and any previous knowledge or assumptions of the atmosphere (i.e. the *a priori*). To account for these errors in computations, the above covariance matrices are constructed with the variance in the measurement and model error at a given wavenumber or *a priori* value at a given level in the atmosphere placed in the corresponding diagonal entry of the respective matrix. In addition, the influence of error at one wavenumber (or level) upon the error at another can be simulated by filling in appropriate off-diagonal covariance elements in the matrix.

Following the development in Rogers (2000), from (5.4) we can define a new matrix G , often referred to as the gain matrix or "generalized inverse" of K as

$$G_i = (S_a^{-1} + K_i^T S_\epsilon^{-1} K_i)^{-1} K_i^T S_\epsilon^{-1} \quad (5.5)$$

From the gain matrix, another matrix can be constructed: the A matrix or "averaging kernel" (Note: This is not the same A matrix used earlier in the exponential matrix when describing the NIR forward model). The contribution that the measurements are making to a retrieved CO_2 profile versus the *a priori* information can be estimated by this matrix. It can be obtained via multiplying G_i by the Jacobian K_i , thus yielding the expression

$$A = G_i K_i \quad (5.6)$$

Employing the above method, the optimal CO_2 profile \hat{x} can be expressed as

$$\hat{x} = x_a + (S_a^{-1} + \hat{K}^T S_\epsilon^{-1} \hat{K})^{-1} \hat{K}^T S_\epsilon^{-1} [y - F(\hat{x}) + \hat{K}(\hat{x} - x_a)] \quad (5.7)$$

where x_a is the *a priori* profile of CO₂ given either by climatology or as the result of previous measurements or model output. The use of hats on K here denotes that it is the Jacobian associated with the optimal solution \hat{x} . Substituting the definitions of y , G , and A provided by (5.2), (5.5), and (5.6), respectively, and linearizing $F(x)$ about \hat{x} , the retrieved profile \hat{x} can be rendered in the alternate form

$$\hat{x} = x_a + \hat{A}(x - x_a) + \hat{G}\epsilon \quad (5.8)$$

where the hats on A and G again denote that these matrices are associated with the optimal solution \hat{x} . This form has the advantage of providing insight as to the composition of the retrieved profile as well as offering an interpretation of the A matrix. If the A matrix is the identity matrix (the ideal), the retrieval relies solely on the measurements and the retrieved profile will be the sum of the real profile and a contribution $\hat{G}\epsilon$ due to measurement and model error; however, as A moves closer and closer to the $\mathbf{0}$ matrix, the retrieved profile more and more assumes the properties of the *a priori* (aside from the error contribution $\hat{G}\epsilon$).

How the covariances S_ϵ and S_a actually affect the covariances in the retrieved profile can be expressed by a covariance matrix S_x which can be obtained by (Rodgers, 2000)

$$S_x = S_a - (S_a^{-1} + \hat{K}^T S_\epsilon^{-1} \hat{K})^{-1} \hat{K}^T S_\epsilon^{-1} \hat{K} S_a \quad (5.9)$$

As in the case of \hat{x} , some simplification can be done to (5.9) by substituting the expressions for G and A to obtain

$$S_x = (I - \hat{A})S_a \quad (5.10)$$

Once again, this form also has the advantage of providing insight as to the composition of the retrieved covariance matrix. It indicates that, if the measurements are reliable ($\hat{A} \approx I$), the error in the retrieved CO₂ profile should be small ($S_x \approx \mathbf{0}$ matrix);

however, if the measurements are not as reliable and the retrieved CO₂ profile depends more on the *a priori*, the error covariances in the retrieved profile will largely come from the assumed covariances in the *a priori*.

To assist in testing the quality of the retrieval, a χ^2 test was employed to test the assumption that \hat{x} belonged to a normal distribution with the assumed error covariances used. From the expression for the cost function J , we have

$$\chi^2 = (\hat{x} - x_a)^T S_a^{-1} (\hat{x} - x_a) + (y - F(\hat{x}))^T S_\epsilon^{-1} (y - F(\hat{x})) \quad (5.11)$$

By a theorem of statistics, if x follows a normal distribution with the error covariances S_a and S_ϵ , then J should be $\chi^2(N)$ - a χ^2 distribution with N degrees of freedom; thus, a value of N for χ^2 is obtained if x is normally distributed and the assumed error covariances are accurate. Now, if either or both of the covariances S_a or S_ϵ are underestimated, then $\chi^2 > N$; however, if both S_a and S_ϵ are overestimated, $\chi^2 < N$. From (5.11), we observe that a portion of the χ^2 value comes from the measurements and a portion from the *a priori*. This will come into play later on.

To provide a reference with which to compare the χ^2 results, the total number of degrees of freedom (DF) can be determined for a given retrieval by simply summing the number of elements in the measurement vector y with the number of elements in the *a priori* vector x_a . Comparing χ^2 with the DF will help provide a sense of how reasonable the assumptions are that the errors are normally distributed with the magnitudes and correlations assigned in the covariance matrices S_a and S_ϵ .

5.2 Application of the Method to Retrieving Profiles of CO₂

The above retrieval scheme is applied to retrieving profiles of atmospheric CO₂. For this study, the covariance matrix S_ϵ will be assumed diagonal (the measurement

error at one wavenumber is assumed independent of the measurement error at other wavenumbers). However, the covariance matrix S_a associated with the *a priori* will assume an exponential form (i.e. the error associated with the *a priori* at one level is assumed to be correlated to the error in the *a priori* at other levels in an exponentially decreasing fashion). Specifically, each of the entries in the *a priori* covariance matrix is determined by the expression

$$\sigma_{ij}^2 = (\sigma_{ii}^2 \sigma_{jj}^2)^{1/2} \exp[-(z_i - z_j)^2 / l^2] \quad (5.12)$$

where σ_{ii} and σ_{jj} are the standard deviations in the *a priori* CO₂ values at altitudes z_i and z_j in the atmosphere, respectively, and the exponential expression determines the correlation coefficient. Here, as in Engelen et al. (2001), we assume $l = 3.0$ km (personal communication). The only deviation from this representation is at the surface where the correlations (and as a result, the covariances) are assumed to be zero due to the highly variable nature of CO₂ in the boundary layer (see below).

The actual values of the variances used on the diagonal of the S_a matrix are based in part on the work of Schmidt and Khedim (1991). Figure 5.1 is Figure 2 of that work.

From this figure, we make the following observations. Focusing on the average midlatitude profile (full dots), we first observe that the concentration of CO₂ falls off as one moves from the mid-troposphere into the lower stratosphere up to 80 hPa (≈ 17 km). From here, a transition region follows which leads to a more homogeneous regime above 35 hPa (≈ 24 km). Further, the amount of variation in CO₂ concentration wanes as one moves from lower to higher altitudes. Based on the variational behavior given in this figure, the standard deviations used to prescribe the variances used for the diagonal elements in the S_a matrix are given in Table 5.1. This profile of error was used in performing CO₂ retrievals in clear-sky cases where there was no interference by a scattering layer or in cases when the altitude and optical depth of the scatterer

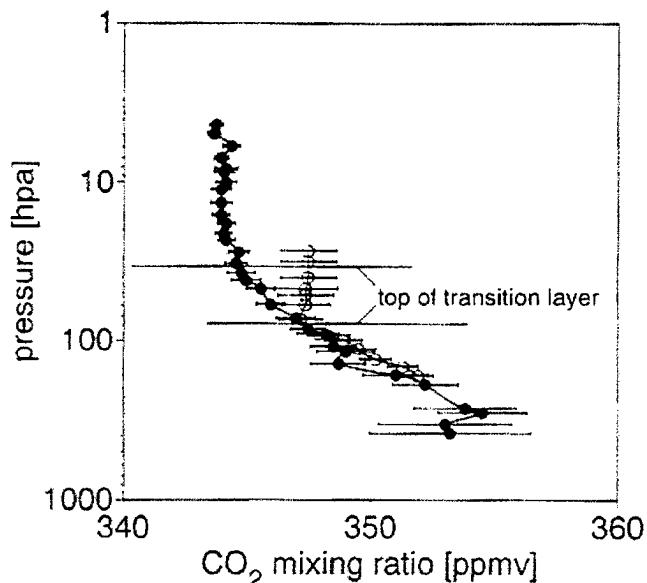


Figure 5.1: Mean vertical CO₂ profile for midlatitudes (44°N), full dots (Schmidt and Khedim, 1991).

was simulated as being precisely known. In these cases, the CO₂ *a priori* profile is designated as *a priori 1*. For those cases when the altitude or optical depth of the scatterer was either unknown or only crudely determined, σ was set to 5.4 ppmv at the surface, 4.4 ppmv at 1 km, and 3.4 ppmv at 2-6 km. All others remained unchanged. This was done to allow the *a priori* profile to constrain the retrieval more in these cases where the effect of the scattering layer is more severe and the measurements could not be relied upon as much as a result. In these cases, the *a priori* profile is designated as *a priori 2*.

The values of σ used for the lower atmosphere below 500 hPa were designed to reflect the larger variations in CO₂ that occur in this region. In particular, the value of σ estimated for the surface is based on CO₂ measurements taken from tall towers (see Bischof (1971), Bischof et al. (1985), Bakwin et al. (1995), and Bakwin et al. (1998)). In these studies, CO₂ demonstrates a highly variable behavior in the boundary layer. Diurnal variations of 50 ppmv are not uncommon with variations near the surface up to 85 ppmv reported from one of these studies. In light of this information, 15 ppmv was chosen as a reasonable initial standard deviation for the

Table 5.1: Diagonal elements of the covariance matrix S_a .

Altitude (km)	σ (ppmv)	Altitude (km)	σ (ppmv)
100	1.0	15	1.0
70	1.0	14	1.1
50	1.0	13	1.3
45	1.0	12	1.5
40	1.0	11	1.9
35	1.0	10	2.3
30	1.0	9	2.7
25	1.0	8	3.0
24	1.0	7	3.4
23	1.0	6	3.7
22	1.0	5	4.0
21	1.0	4	4.4
20	1.0	3	4.7
19	1.0	2	5.0
18	1.0	1	7.0
17	1.0	0	15.0
16	1.0		

surface for *a priori* 1. Of course, if and when the ideas presented in this work are implemented in an operational framework, the error statistics of the *a priori* profile could be tuned for each locale in which the measurements are made and thus yield more precise *a priori* for that region.

The measurements used in the retrieval were taken from the 6203.400-6221.475 cm^{-1} spectral interval in the 1.6 μm region of the NIR at a resolution of 0.025 cm^{-1} (724 channels) and from 500-2500 cm^{-1} in the IR at a resolution of 1 cm^{-1} (2000 channels). This portion of the 1.6 μm region was chosen for its lack of interference from other atmospheric gases. Nadir viewing was employed in both the IR and NIR with the surface assumed Lambertian (i.e. it scatters isotropically) with a surface temperature of 296K and different surface albedos to simulate different surfaces.

Chapter 6

Near Infrared Sensitivity Study

As alluded to earlier, the retrieval of CO₂ is a process that could be influenced by a number of variables. Among these are undetected (subvisual) cirrus and aerosol. In addition, since the measurements in the NIR are making use of reflected sunlight, solar zenith angle θ_{\odot} and surface albedo α should also be considered. Thus, a sensitivity study is provided to estimate some of the potential influences of these elements on a CO₂ retrieval.

As far as the optical properties of the cloud and aerosol are concerned, they are both assumed to possess an asymmetry factor of $g = 0.75$ and single scatter albedo of $\omega = 1.00$. The Henyey-Greenstein phase function was assumed to characterize the cloud and aerosol's pattern of scatter. Although the Henyey-Greenstein is not totally adequate to describe the scattering pattern of an ice cloud for example, which are notorious for having complex phase functions, the Henyey-Greenstein was used as in O'Brien and Rayner (2002) to provide a reasonable upper bound on the scattered radiance.

The instrument in the NIR is assumed to have a δ -function response. Since high resolution measurements appear to be required for the measurement of CO₂ (O'Brien and Rayner, 2002), a δ -function response will again provide an upper bound on what the NIR measurements can be expected to provide.

The surface albedo is assumed to remain constant across this narrow spectral region of the 1.6 μm band, both in this NIR sensitivity study and in the retrievals performed later. In addition, the underlying surface is assumed Lambertian, which for ocean surfaces is generally reasonable for a solar zenith angle $\theta_o < 50^\circ$ (Bukata et al., 1995), but for land surfaces is more uncertain as their reflective characteristics are not as well known.

Using the Bode definition of sensitivity (Bode, 1945)

$$S = \frac{x}{I} \frac{\partial I}{\partial x} \quad (6.1)$$

the sensitivity of the radiances I in the 1.6 μm region of the NIR to the optical depth of thin cirrus and aerosol as well as CO_2 concentration was estimated. The first portion of the study focused on the influence of thin cirrus and aerosol on the NIR radiances. It was performed for four cirrus and four aerosol scenarios, each at four values of solar zenith angle and four values of surface albedo yielding a total of 128 scenarios. The second portion of the study focused on the influence of the CO_2 on these radiances also for varying solar zenith angles and albedos. The results of this study are presented next.

6.1 Sensitivity to Cirrus and Aerosol

A certain amount of undesirable scattering is introduced by cirrus clouds due to their ice crystals. If cirrus can be detected, then it and its accompanying scattering can be avoided; however, unlike the lower, more optically thick clouds in the atmosphere, thin cirrus can be very difficult to detect. Thus, if measurements are taken in a region where thin cirrus are present but cannot be detected due to their minute optical depth, then spurious scatter is introduced. The presence of this scatter can have a potentially degrading or devastating effect on a CO_2 retrieval.

To assess the effect of thin cirrus on a CO_2 retrieval, a sensitivity study was

Table 6.1: Key for sensitivity plots.

Cirrus Scenario	Altitude (km)	τ	Aerosol Scenario	Altitude (km)	τ
Cirrus 1	12-13	0.05	Aerosol 1	12-13	0.05
Cirrus 2	12-13	0.10	Aerosol 2	12-13	0.20
Cirrus 3	6-7	0.05	Aerosol 3	1-2	0.05
Cirrus 4	6-7	0.10	Aerosol 4	1-2	0.20

performed. Cirrus clouds of optical depth $\tau = 0.05$ and 0.10 were assumed in the regions 6-7 km and 12-13 km with the optical properties stated at the beginning of this chapter. This gives four scenarios which are denoted Cirrus 1 - Cirrus 4 on the left hand side of Table 6.1. The results of the cirrus cases are given in the lefthand column of Figures 6.1 - 6.16 and will be addressed shortly. Use Table 6.1 as a key to matching these scenarios with the left hand plots of these figures.

Like cirrus, the presence of aerosol can also complicate any attempt to retrieve atmospheric CO_2 due to the scattering it can bring. If the aerosol can be detected, its accompanying scattering can be avoided or taken into account; however, optically thin layers of aerosol, like thin cirrus, can also be difficult to detect. Thus, if measurements are taken in a region where a thin aerosol layer is present but undetected, then spurious scatter is also introduced. This scattering introduces a debilitating effect on retrieving atmospheric CO_2 to the high degree of accuracy required to be of benefit to efforts to determine CO_2 surface sources and sinks.

A similar set of sensitivity experiments were performed for aerosol. Aerosol layers of optical depth $\tau = 0.05$ and 0.20 were placed in the regions 1-2 km and 12-13 km with the optical properties stated at the beginning of this chapter. This also gives four scenarios and are denoted Aerosol 1 - Aerosol 4 on the right hand side of Table 6.1. The sensitivity results of the aerosol cases are given in the right hand column of Figures 6.1 - 6.16.

Each of the four cirrus scenarios and four aerosol scenarios were performed for a solar zenith angle $\theta_{\odot} = 0^{\circ}, 30^{\circ}, 45^{\circ},$ and 60° and a surface albedo $\alpha = 0.10, 0.25, 0.40,$ and 0.75 . This gives 128 scenarios total. The values of surface albedo were

Table 6.2: Typical surface albedos for different surfaces in the $1.6\mu\text{m}$ spectral region. (* = from Elachi (1987))

Surface	Albedo
Ocean	0.05
Snow,Ice	0.15
Alfalfa, Soybeans*	0.20
Bare Soil*	0.40
Composite Rock*	0.60

chosen to correspond to a wide range of different surfaces (See Table 6.2).

For this portion of the sensitivity study, the x in equation (6.1) was the optical depth of the cirrus (τ_c) or aerosol (τ_a). The partial derivative in the equation was computed by finite difference. The first radiance was computed for the value of optical depth given in Table 6.1. For the second radiance calculation, the optical depth was reduced by $\delta\tau = -0.0001$ when the initial optical depth was $\tau = 0.05$ and by $\delta\tau = -0.001$ when the initial optical depth was either $\tau = 0.10$ or 0.20 .

There are at least four notable features in Figures 6.1 - 6.16. First, as α increases for a given θ_\odot , the sensitivity of the reflected radiance to τ_c or τ_a becomes less positive/more negative (i.e. $\frac{\partial S}{\partial \alpha} < 0$). For example, compare the cirrus 2 scenario in Figures 6.2, 6.6, 6.10, and 6.14. The reason for this is that more and more of the reflected radiant energy is coming from the underlying surface. For example, if we take a thin cirrus cloud and increase its optical depth slightly over a surface whose albedo is very small, the radiance returned from the new cloud/surface combination will be greater than that originally due to better returns from the cloud. However, if we take the same thin cirrus cloud and increase its optical depth slightly over a surface whose albedo is large, the radiance returned from the new cloud/surface combination will be smaller than that originally because the stronger returns from the surface are now being obscured by the cloud.

A second phenomenon to observe is, as θ_\odot increases for a given value of α , the sensitivity to τ_c or τ_a becomes more positive/less negative (i.e. $\frac{\partial S}{\partial \theta_\odot} > 0$). To observe this behavior, compare the aerosol 2 scenarios in Figures 6.9 - 6.12 for example. This

is also expected because, as θ_{\odot} increases, more and more photons are scattered off the cloud or aerosol layer and less returned from the more CO₂-rich region below where they can be absorbed. That is, at lower solar zenith angles, the scattering layer tends to serve more as a trap, preventing photons from easily exiting the more CO₂-rich region below the scattering layer, whereas at higher solar zenith angles, the layer tends to serve more as a barrier, preventing photons from entering the lower region. The result is suppressed radiances when the optical depth of the scattering layer is slightly increased at lower solar zenith angles and enhanced radiances when its optical depth is increased at higher solar zenith angles.

Thirdly, for a given value of τ_c or τ_a , the sensitivity to the cloud or aerosol is of larger magnitude at higher altitude ($\frac{\partial |S|}{\partial H} > 0$). For example, compare cirrus 2 with cirrus 4 in any of Figures 6.1 - 6.16. This is reasonable because with the scatterer at higher altitude, this implies greater opportunity for photons to be absorbed by CO₂ in the larger region below the cloud or aerosol when it is acting more as a trap and less opportunity when acting more as a barrier. The magnitude of the radiance sensitivity to τ_c or τ_a at a higher altitude increases as a result.

Lastly, the sensitivity of the radiances to changes in cloud or aerosol optical depth at a fixed altitude is of greater magnitude with greater optical depth ($\frac{\partial |S|}{\partial \tau} > 0$). For example, compare aerosol 1 with aerosol 2 in any of Figures 6.1 - 6.16. A cloud or aerosol of greater optical thickness serves as a better trap or barrier, thus either impeding photons from exiting the lower region once there or preventing photons from passing through to the lower region to begin with where they can experience more absorption. Thus, the sensitivity of the radiances to thin cloud or aerosol is of greater magnitude when their optical depth is greater.

For these cases, we observe that the radiances can be suppressed by up to 5% to being enhanced by up to 50%. This is highly variable and potentially disastrous behavior if not accurately accounted for.

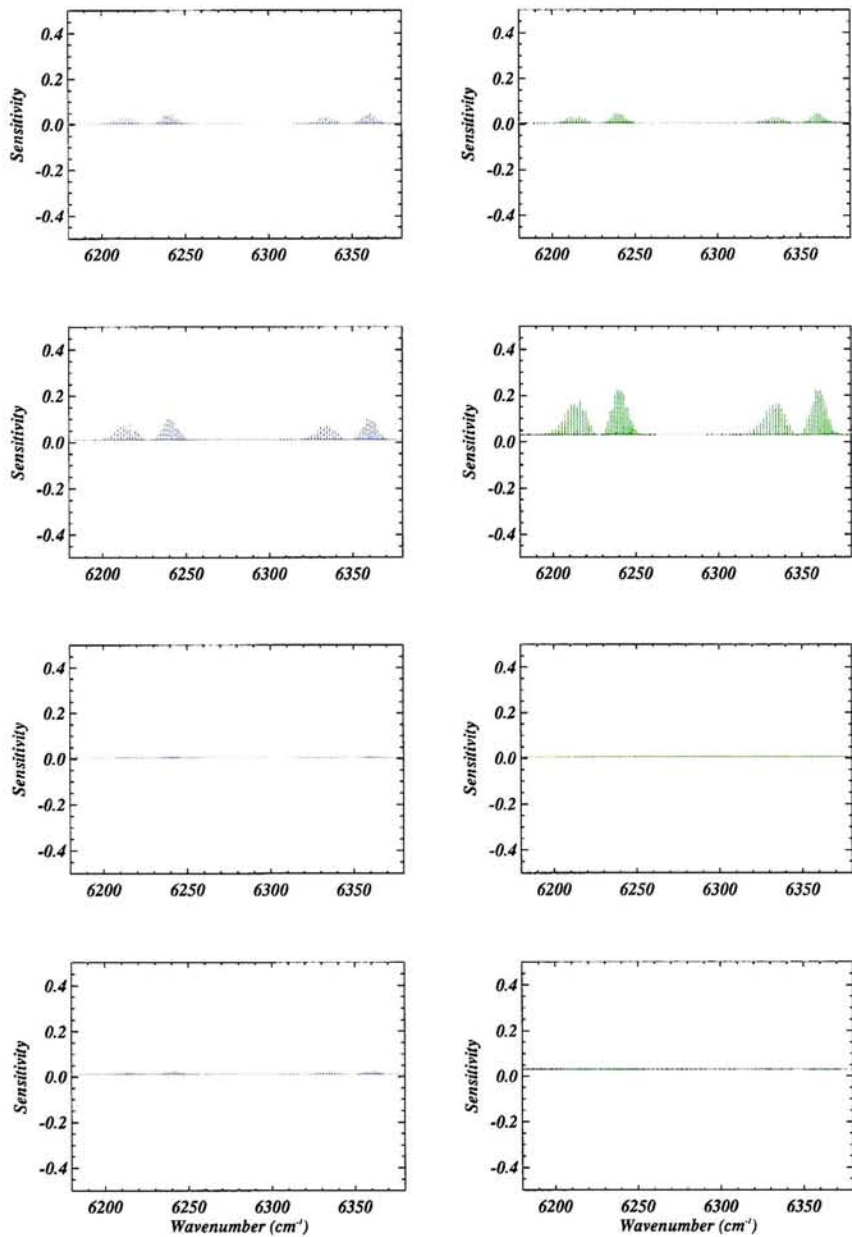


Figure 6.1: Sensitivity of $1.6\mu m$ radiances to thin cirrus (left) and aerosol (right) for $\alpha = 0.1$ and $\theta_{\odot} = 0^{\circ}$. See Table 6.1 for key to cirrus and aerosol scenarios.

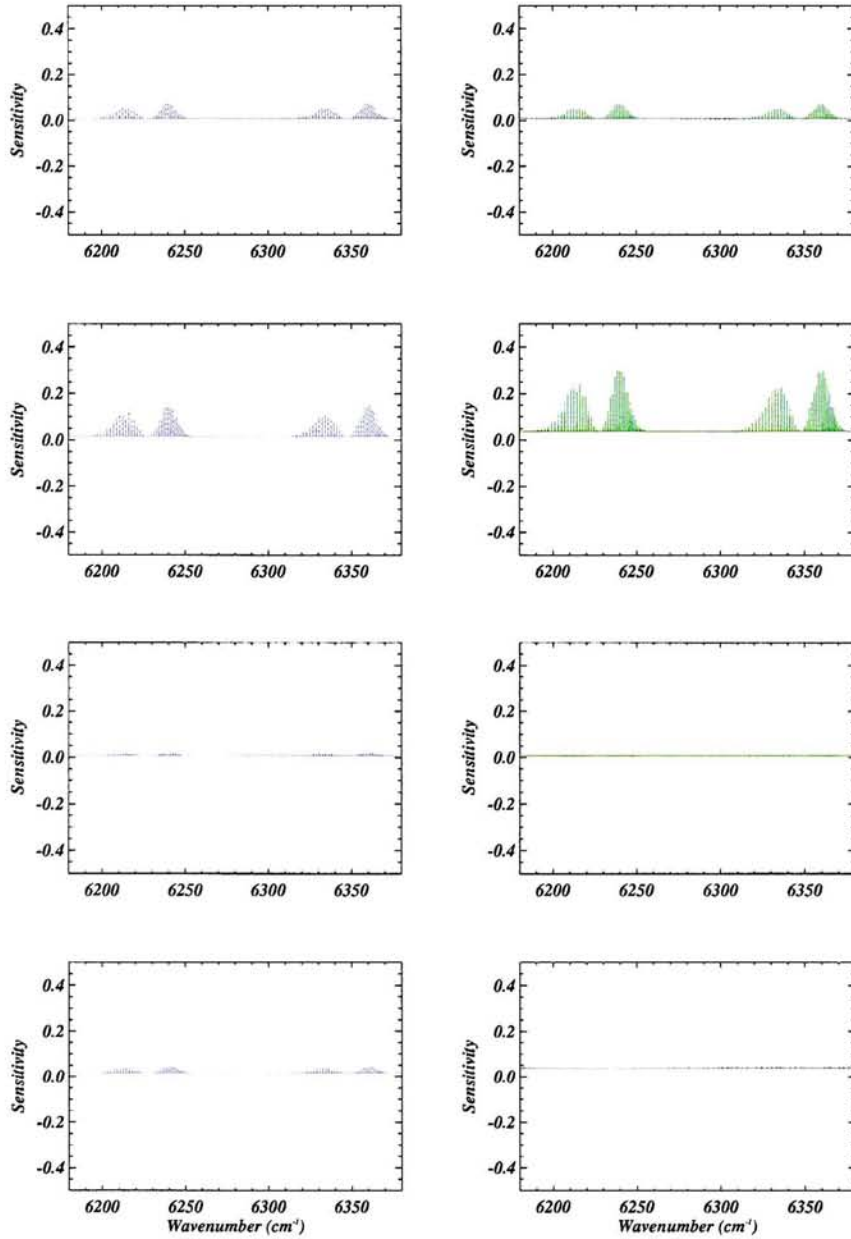


Figure 6.2: Sensitivity of $1.6\mu\text{m}$ radiances to thin cirrus (left) and aerosol (right) for $\alpha = 0.1$ and $\theta_{\odot} = 30^{\circ}$. See Table 6.1 for key to cirrus and aerosol scenarios.

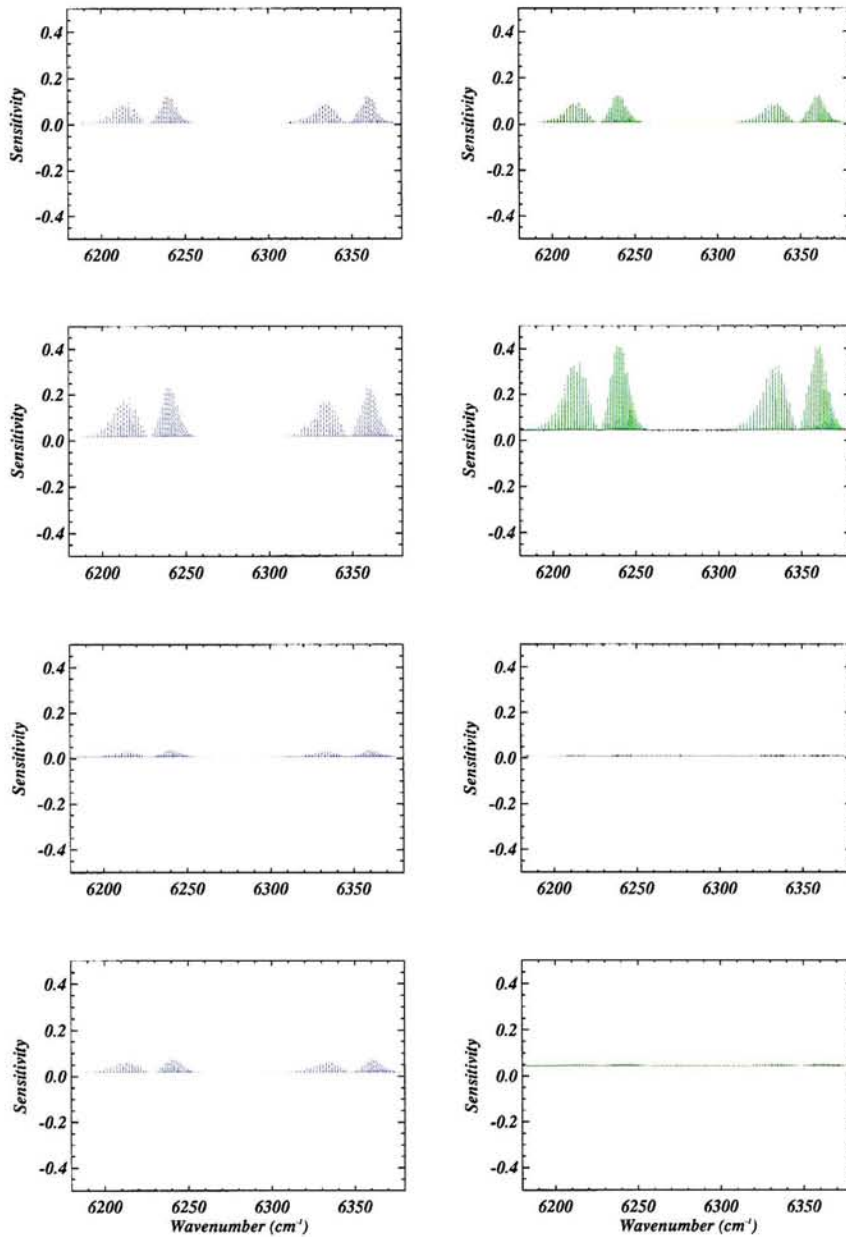


Figure 6.3: Sensitivity of $1.6\mu m$ radiances to thin cirrus (left) and aerosol (right) for $\alpha = 0.1$ and $\theta_{\odot} = 45^{\circ}$. See Table 6.1 for key to cirrus and aerosol scenarios.

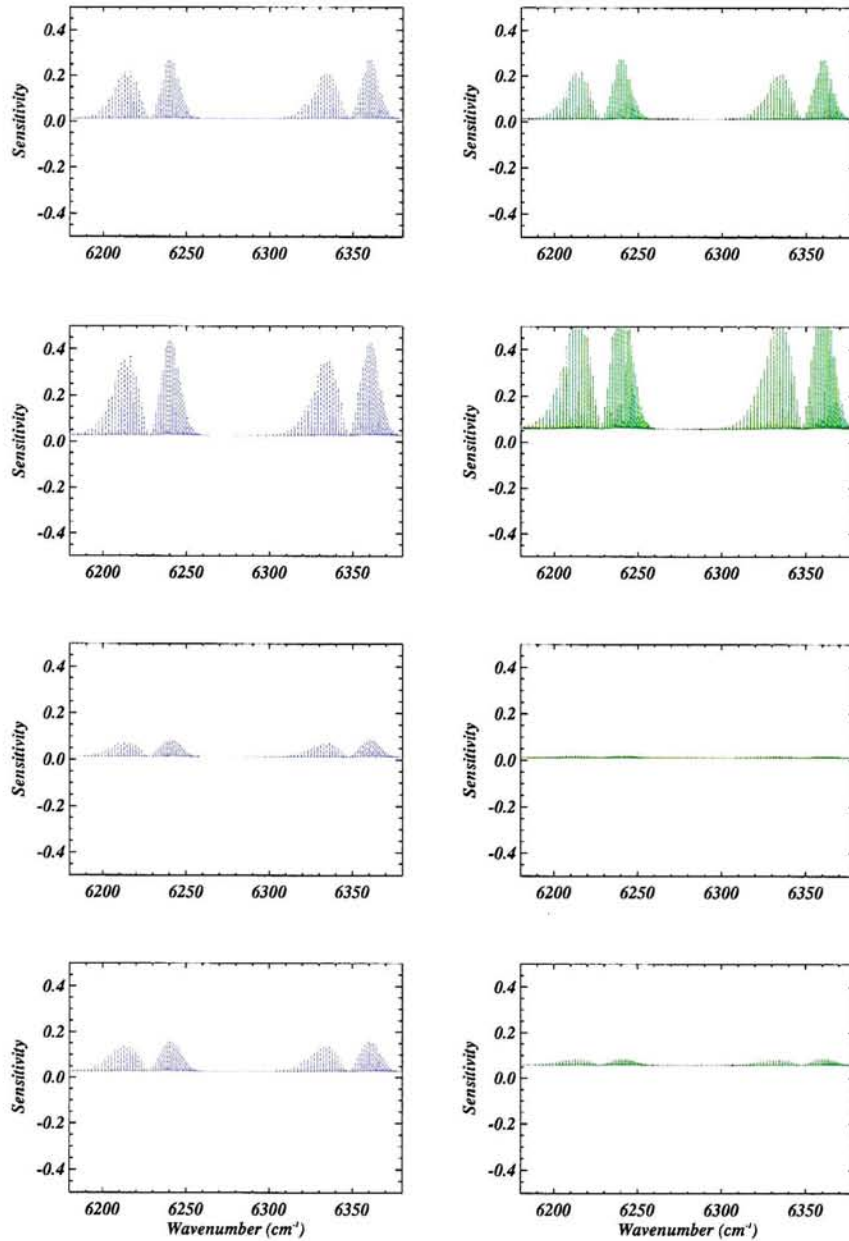


Figure 6.4: Sensitivity of $1.6\mu m$ radiances to thin cirrus (left) and aerosol (right) for $\alpha = 0.1$ and $\theta_{\odot} = 60^{\circ}$. See Table 6.1 for key to cirrus and aerosol scenarios.

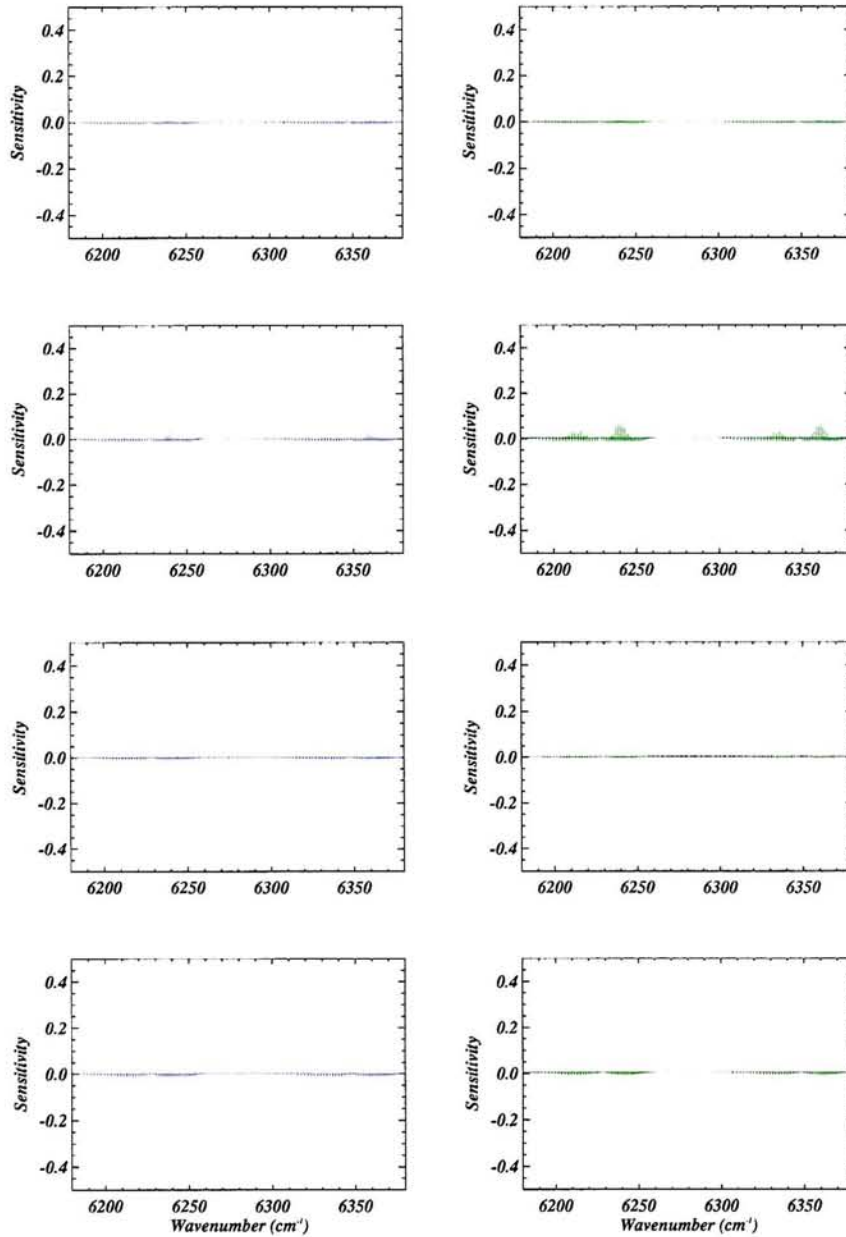


Figure 6.5: Sensitivity of $1.6\mu m$ radiances to thin cirrus (left) and aerosol (right) for $\alpha = 0.25$ and $\theta_{\odot} = 0^{\circ}$. See Table 6.1 for key to cirrus and aerosol scenarios.

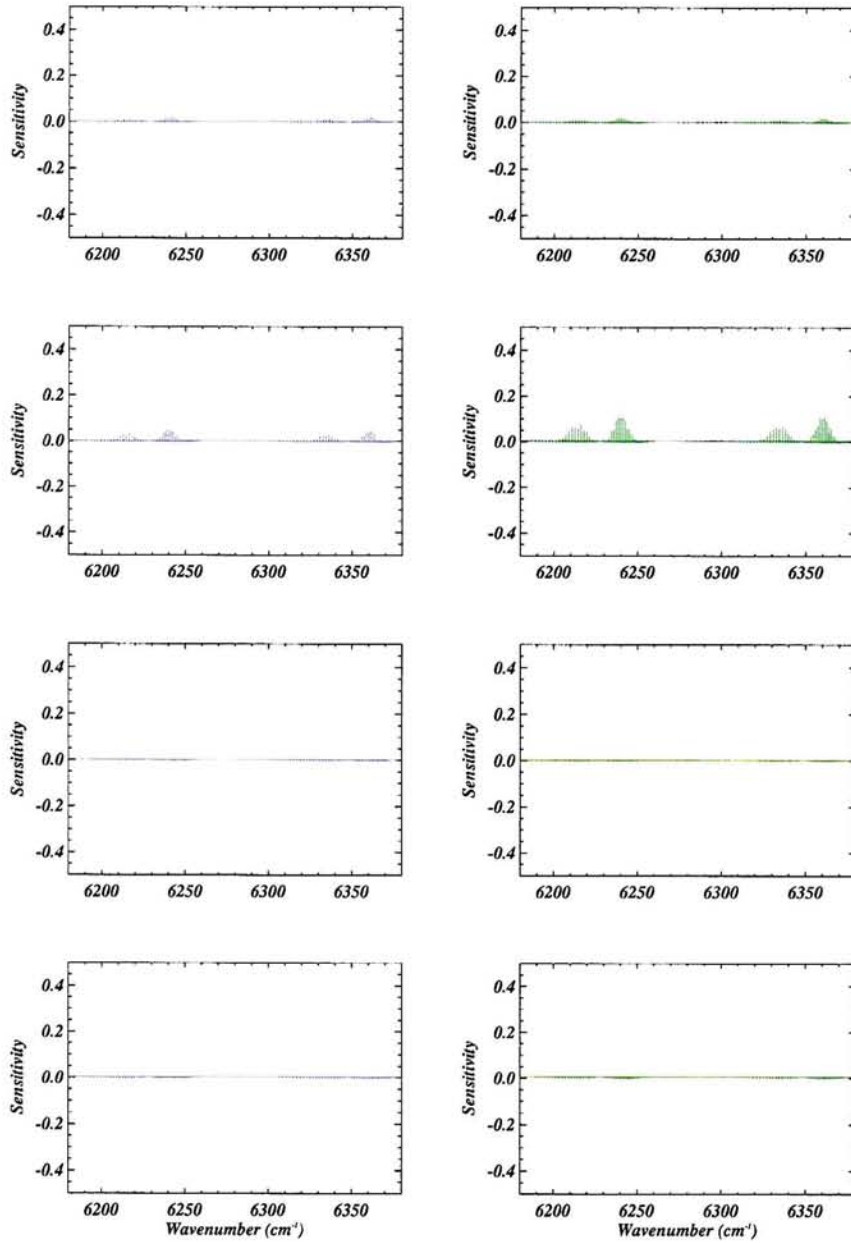


Figure 6.6: Sensitivity of $1.6\mu m$ radiances to thin cirrus (left) and aerosol (right) for $\alpha = 0.25$ and $\theta_{\odot} = 30^{\circ}$. See Table 6.1 for key to cirrus and aerosol scenarios.

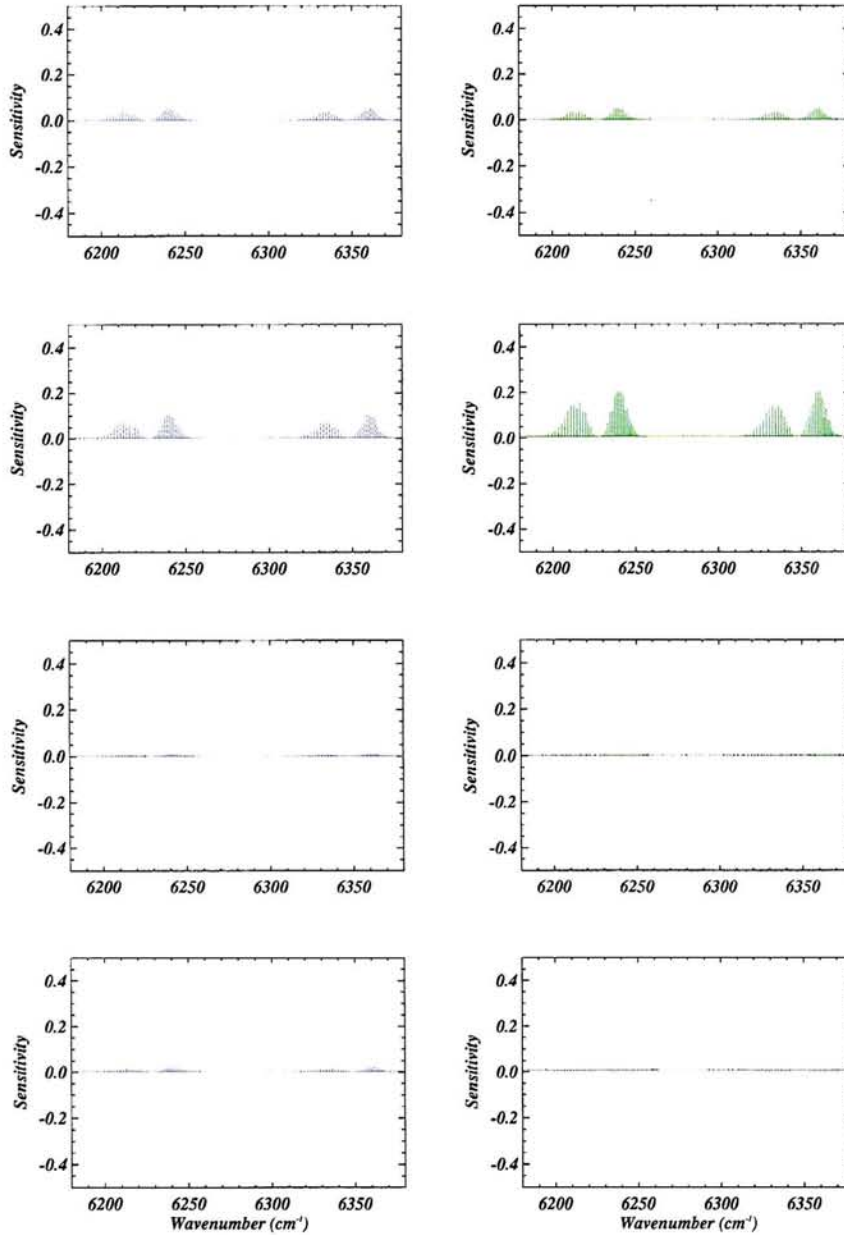


Figure 6.7: Sensitivity of $1.6\mu m$ radiances to thin cirrus (left) and aerosol (right) for $\alpha = 0.25$ and $\theta_{\odot} = 45^{\circ}$. See Table 6.1 for key to cirrus and aerosol scenarios.

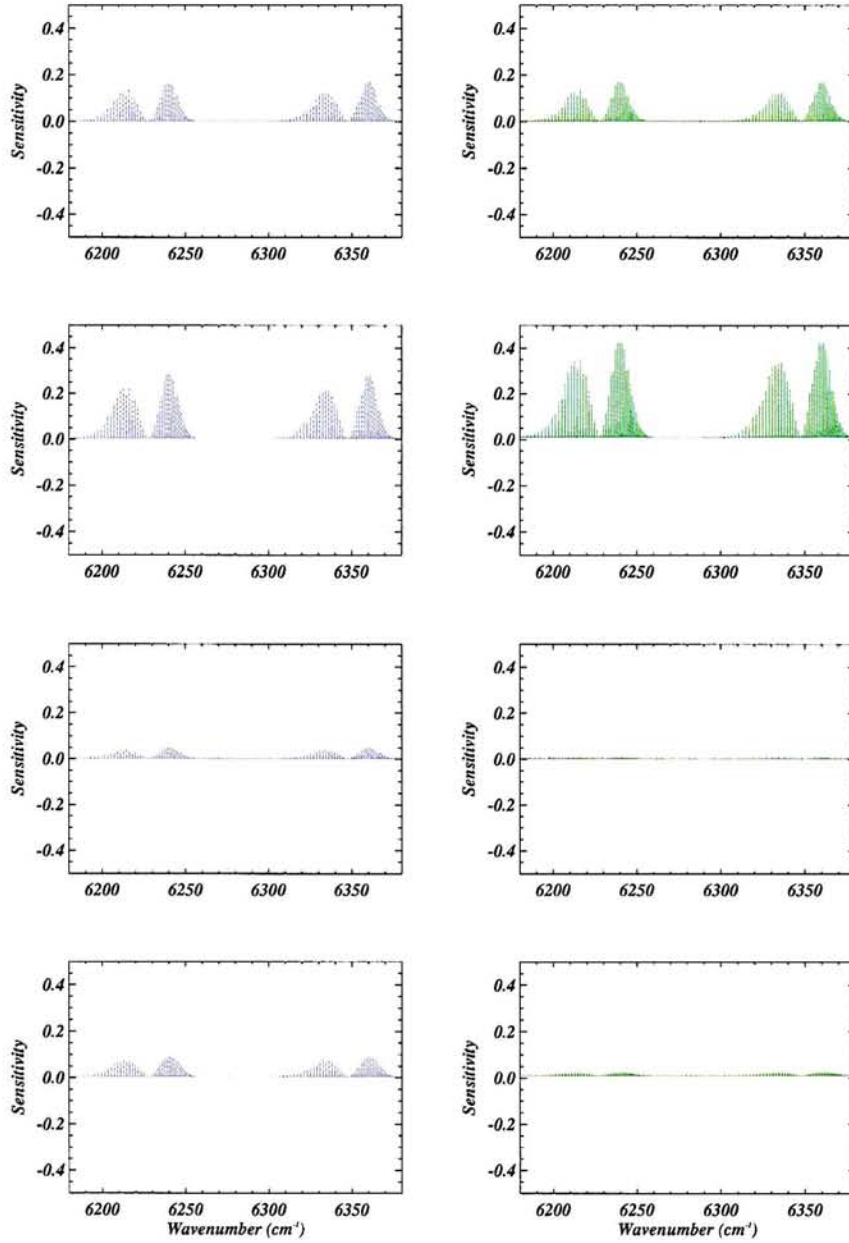


Figure 6.8: Sensitivity of $1.6\mu m$ radiances to thin cirrus (left) and aerosol (right) for $\alpha = 0.25$ and $\theta_{\odot} = 60^{\circ}$. See Table 6.1 for key to cirrus and aerosol scenarios.

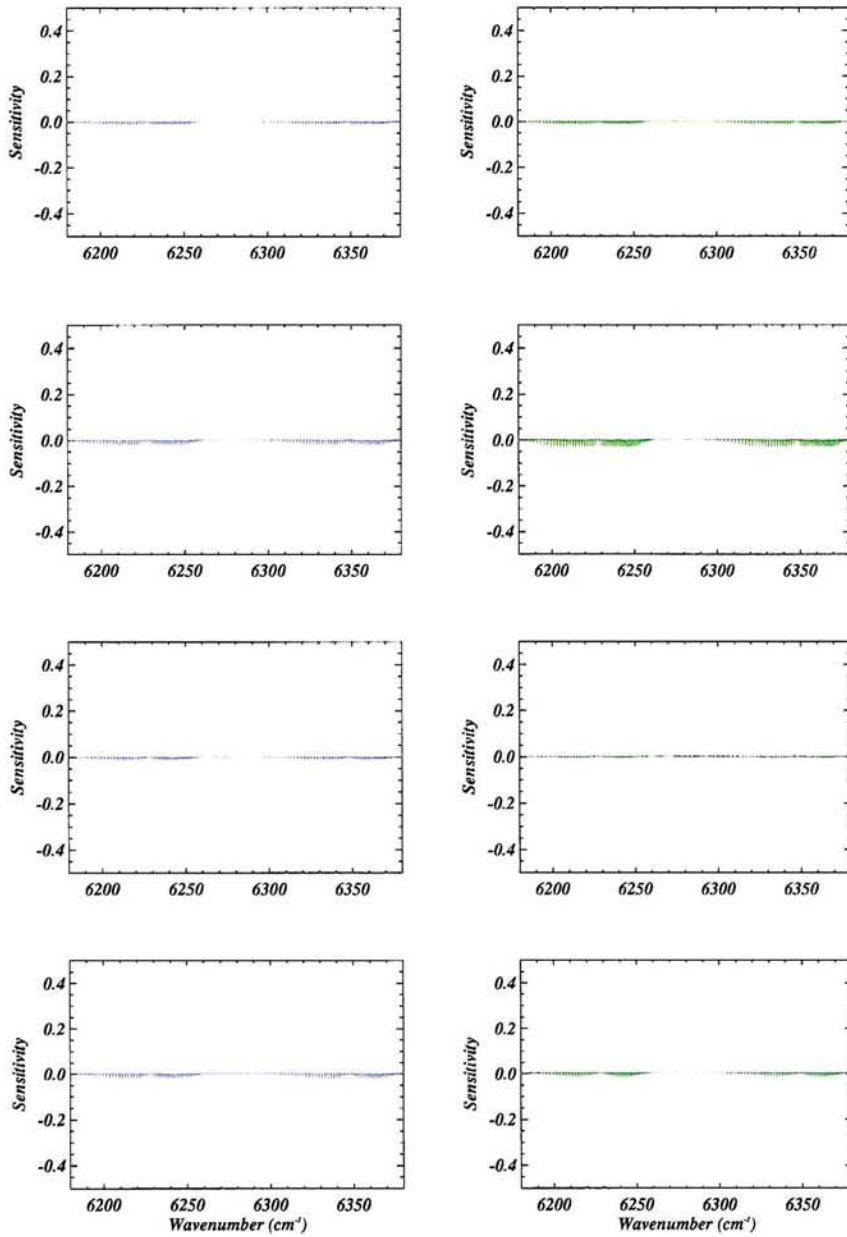


Figure 6.9: Sensitivity of $1.6\mu m$ radiances to thin cirrus (left) and aerosol (right) for $\alpha = 0.4$ and $\theta_{\odot} = 0^{\circ}$. See Table 6.1 for key to cirrus and aerosol scenarios.

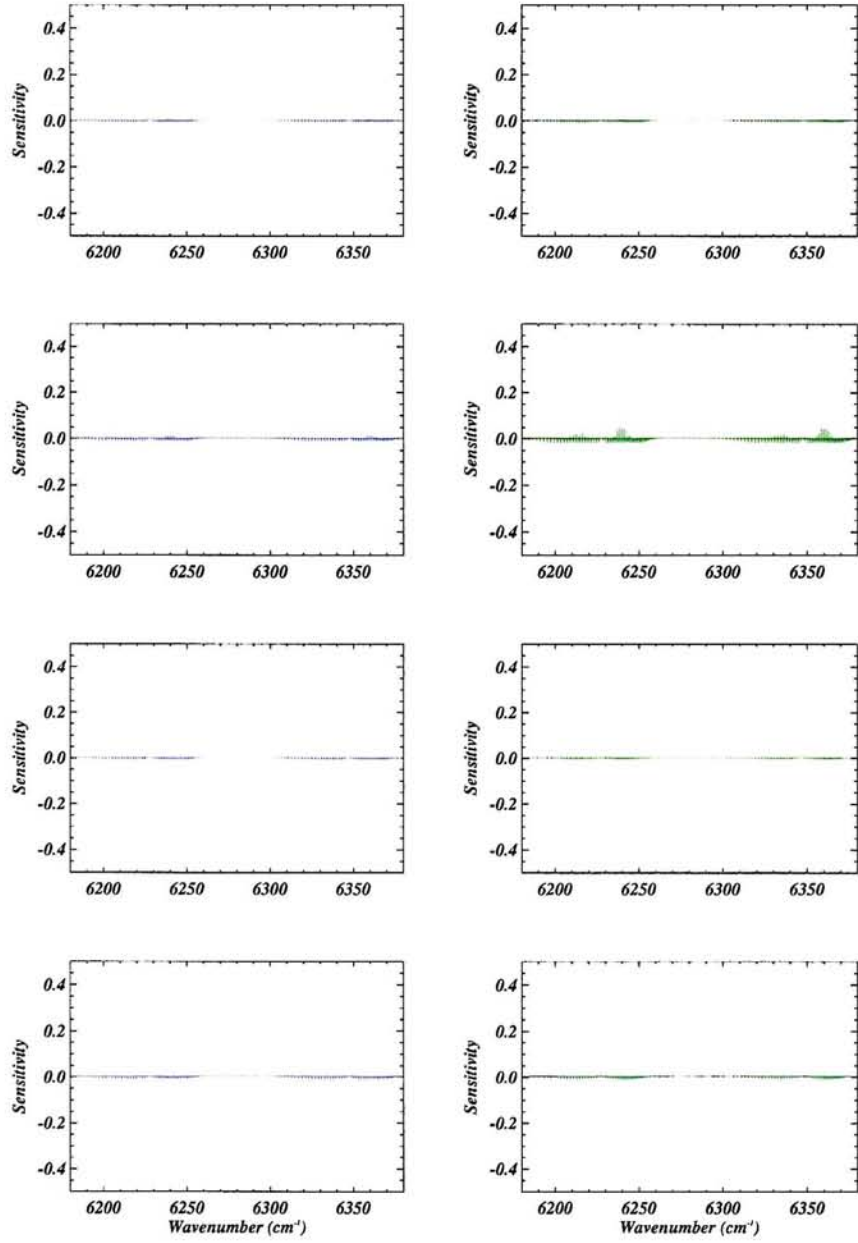


Figure 6.10: Sensitivity of $1.6\mu m$ radiances to thin cirrus (left) and aerosol (right) for $\alpha = 0.4$ and $\theta_{\odot} = 30^{\circ}$. See Table 6.1 for key to cirrus and aerosol scenarios.

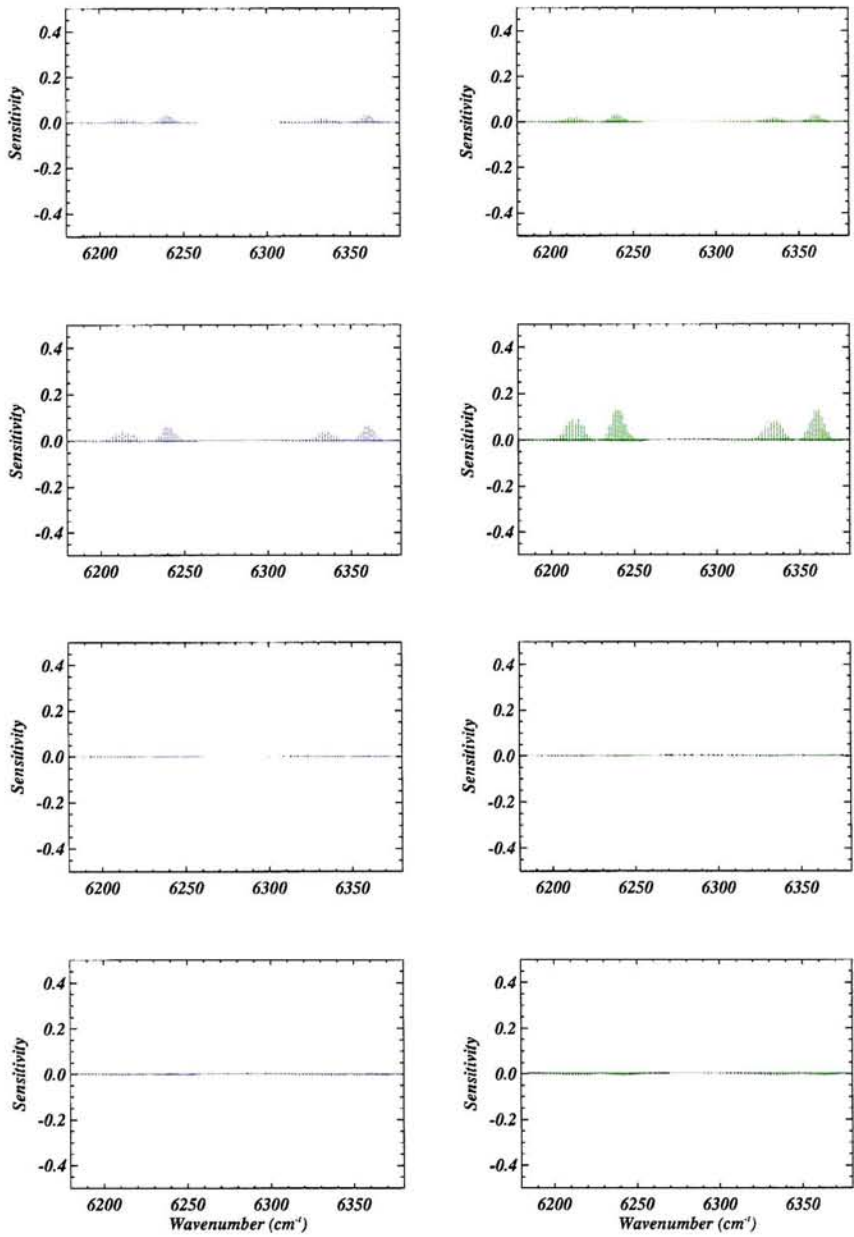


Figure 6.11: Sensitivity of $1.6\mu m$ radiances to thin cirrus (left) and aerosol (right) for $\alpha = 0.4$ and $\theta_{\odot} = 45^{\circ}$. See Table 6.1 for key to cirrus and aerosol scenarios.

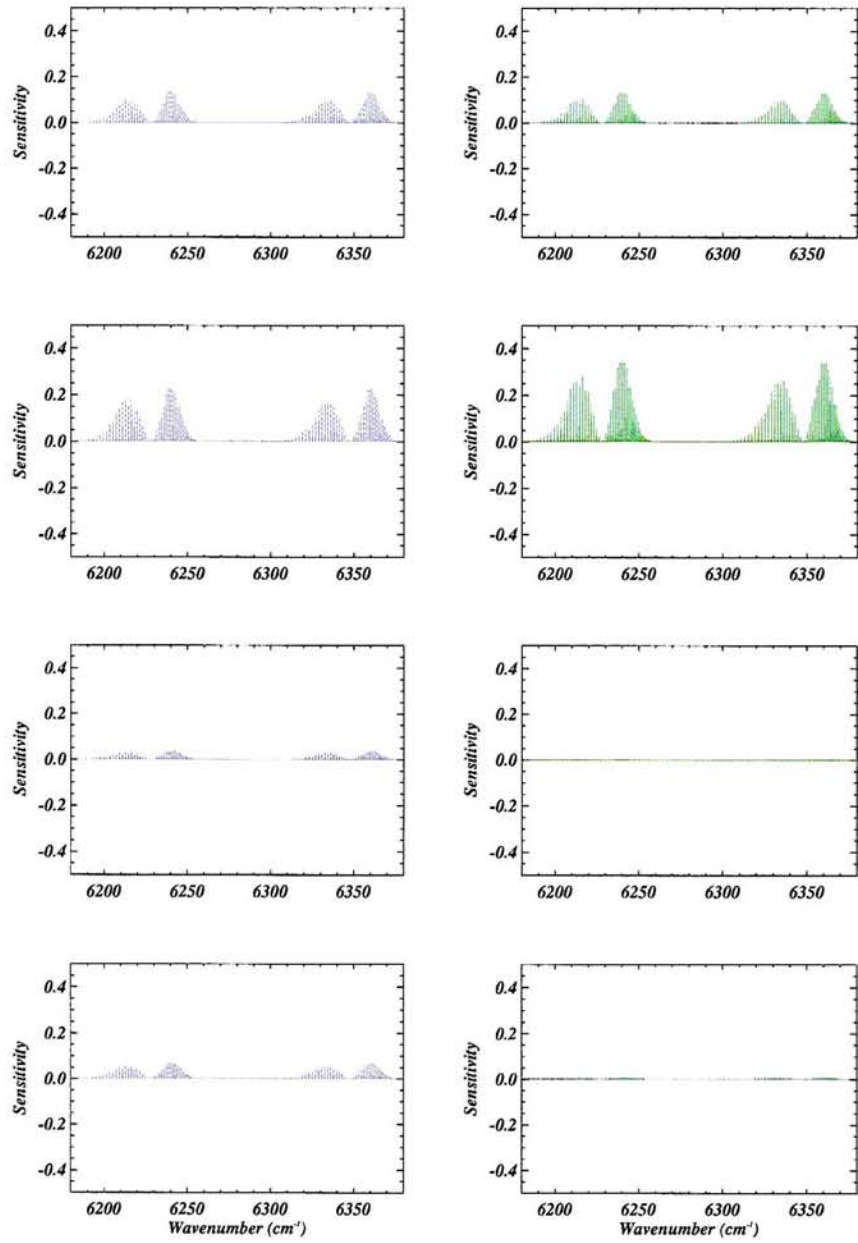


Figure 6.12: Sensitivity of $1.6\mu m$ radiances to thin cirrus (left) and aerosol (right) for $\alpha = 0.4$ and $\theta_{\odot} = 60^{\circ}$. See Table 6.1 for key to cirrus and aerosol scenarios.

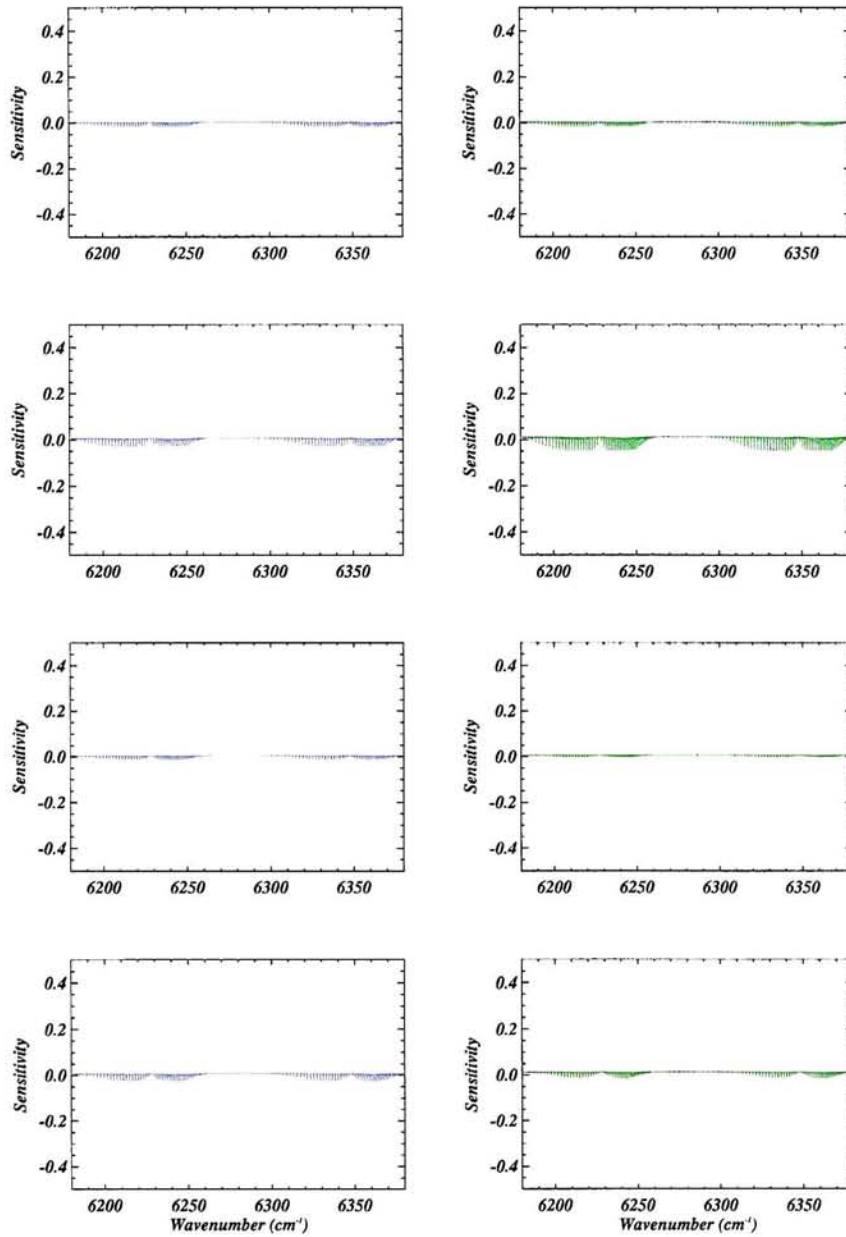


Figure 6.13: Sensitivity of $1.6\mu m$ radiances to thin cirrus (left) and aerosol (right) for $\alpha = 0.75$ and $\theta_{\odot} = 0^{\circ}$. See Table 6.1 for key to cirrus and aerosol scenarios.

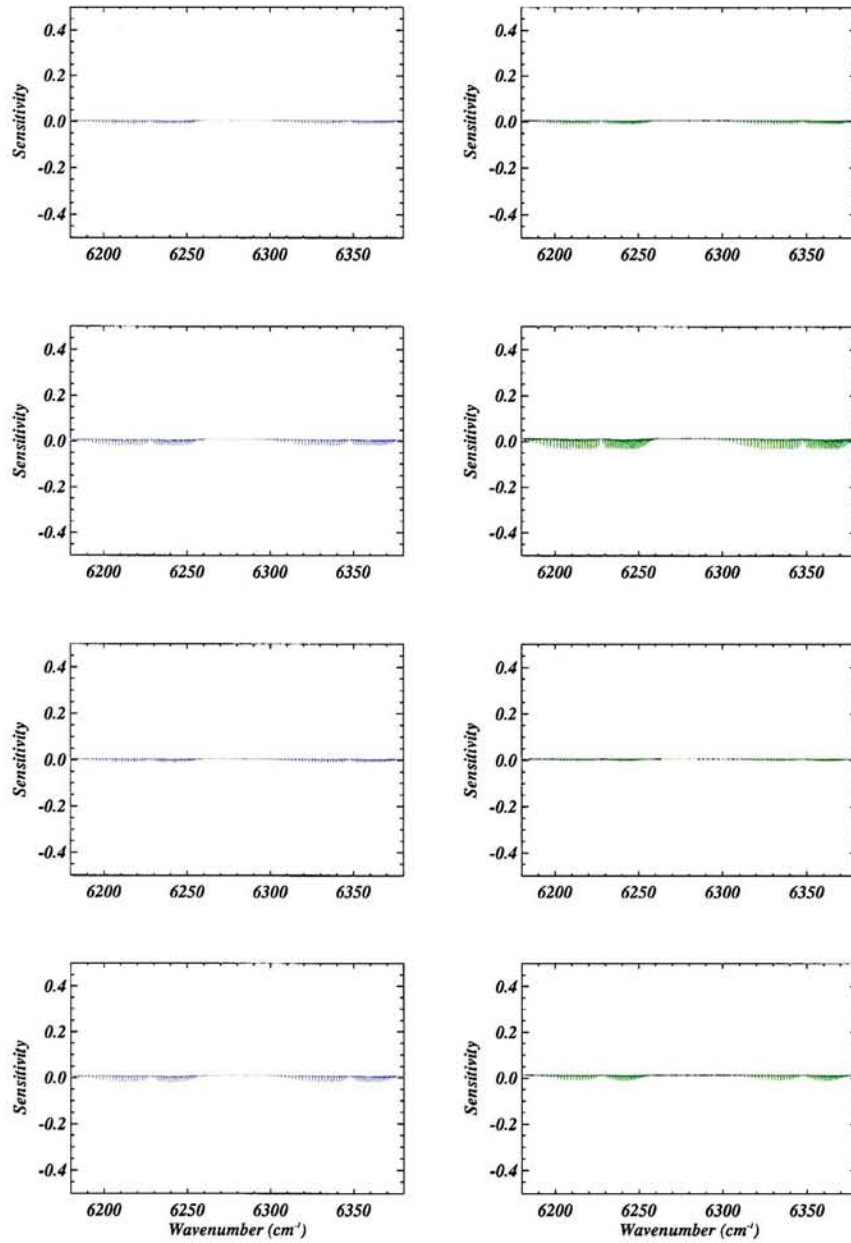


Figure 6.14: Sensitivity of $1.6\mu m$ radiances to thin cirrus (left) and aerosol (right) for $\alpha = 0.75$ and $\theta_{\odot} = 30^{\circ}$. See Table 6.1 for key to cirrus and aerosol scenarios.

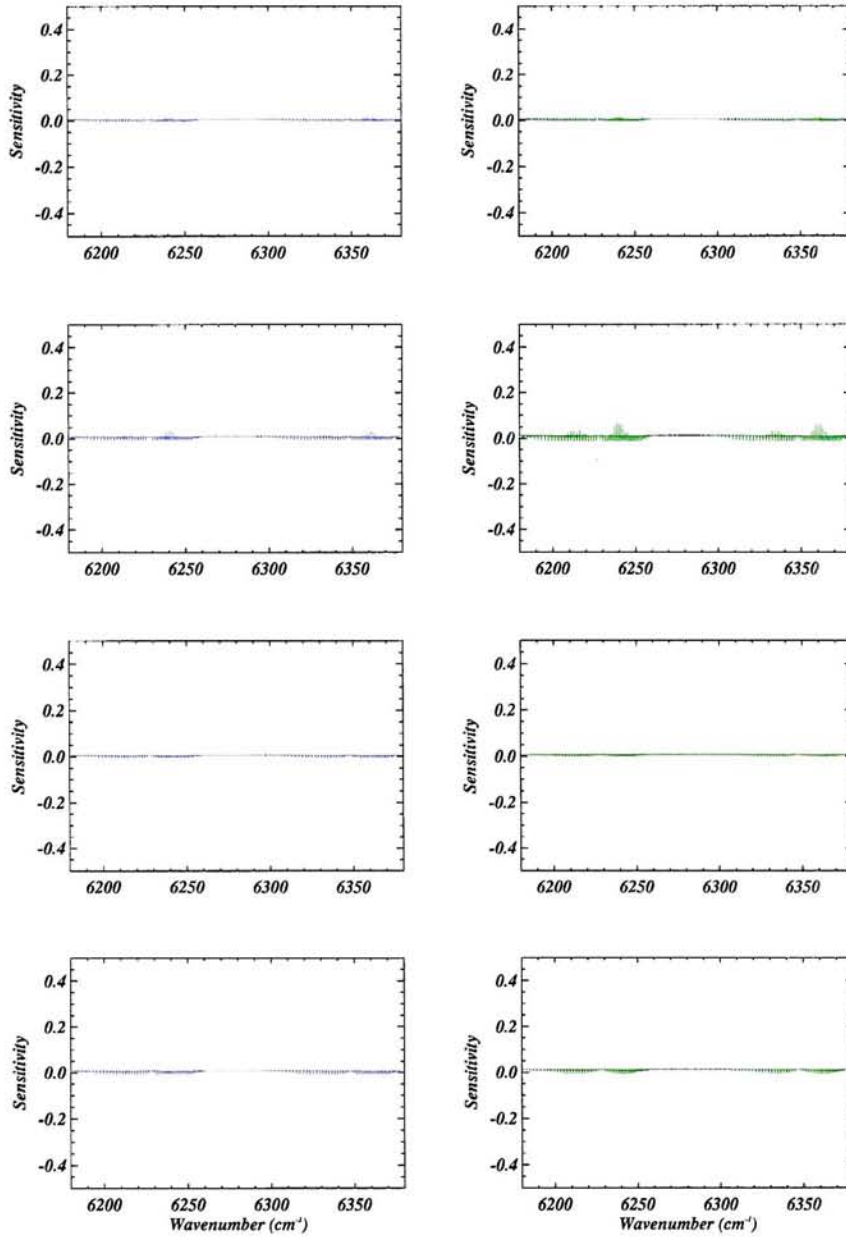


Figure 6.15: Sensitivity of $1.6\mu m$ radiances to thin cirrus (left) and aerosol (right) for $\alpha = 0.75$ and $\theta_{\odot} = 45^{\circ}$. See Table 6.1 for key to cirrus and aerosol scenarios.

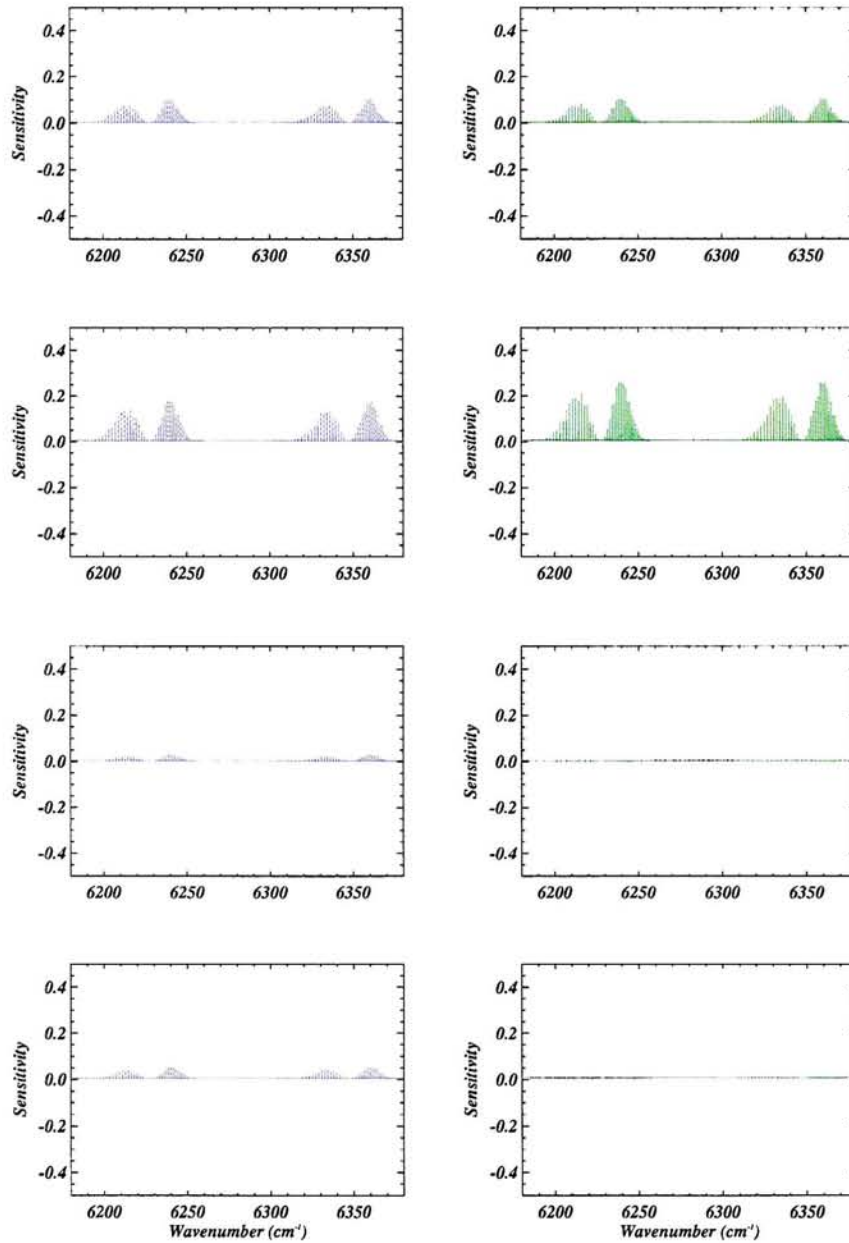


Figure 6.16: Sensitivity of $1.6\mu m$ radiances to thin cirrus (left) and aerosol (right) for $\alpha = 0.75$ and $\theta_{\odot} = 60^{\circ}$. See Table 6.1 for key to cirrus and aerosol scenarios.

6.2 Sensitivity to CO₂

Figure 6.17 shows the sensitivity of the radiances in the 1.6 μm region of the NIR to changes in CO₂. Specifically, it reveals the sensitivity of the radiances to the CO₂ volume mixing ratio q_{gas} for clear sky scenarios. Each row in the figure corresponds to a scenario with fixed surface albedo α . Here, α takes on values of 0.10, 0.25, 0.40, and 0.75 as one moves down the page. Each column in the figure corresponds to a scenario with fixed solar zenith angle θ_{\odot} . In the figure, θ_{\odot} takes on values of 0°, 30°, 45°, and 60° as one moves across the page from left to right. For example, row 2 and column 3 correspond to the case where $\alpha = 0.25$ and $\theta_{\odot} = 45^\circ$. For these plots, a specific profile of CO₂ was given and the CO₂ mixing ratio perturbed by 2 ppmv in the 0-1 km region of the atmosphere.

Moving down the page, one noteworthy feature of the results shows that the CO₂ sensitivity becomes marginally more negative as α increases for a given θ_{\odot} . This effect has nothing to do with the CO₂ itself, but rather with Rayleigh scattering from molecules of oxygen and nitrogen in the atmosphere. This effect was isolated by initially accounting for the Rayleigh scatter in the NIR forward model whereby the plots in Figure 6.17 were obtained. The Rayleigh scatter in the model was then turned off and then some of the cases re-run. With the Rayleigh scatter turned off, the variation in CO₂ sensitivity with α disappeared. This makes sense as one would not expect a change in CO₂ sensitivity if the atmosphere only absorbed photons as they attempted to pass through it. However, Rayleigh scatter is a reality in our atmosphere and thus its affect remains.

Moving across the page from left to right, another observation is that, as θ_{\odot} increases for a given value of α , the sensitivity of the radiances to the CO₂ mixing ratio becomes more negative. This is due to the increase in optical path of CO₂ through which the photons must pass along increasing slant paths. That is, the photons must traverse a longer distance through the CO₂-rich lower atmosphere: this leaves them more susceptible to absorption by CO₂. As a result, the radiances are made more

sensitive. Depending on the wavenumber, the sensitivity of the radiances to CO₂ in this region of the atmosphere varied from 0-20%.

The last two experiments performed in the sensitivity study were to see how the sensitivity of the radiances to CO₂ changed across a large range of values of surface albedo and solar zenith angle for a few wavenumbers in the 6203.400-6221.475 cm⁻¹ spectral interval from the 1.6 μm region. This interval was chosen because absorption of photons here is due almost exclusively to absorption lines of CO₂. Consequently, these NIR wavenumbers were chosen to retrieve the profile of CO₂ concentration later in this work.

For these two experiments, three wavenumbers were selected from this interval: one sensitive to CO₂ in the upper troposphere at 11 km (6216.35 cm⁻¹), one sensitive in the mid-troposphere at 5 km (again 6216.35 cm⁻¹), and one sensitive at the surface (6212.80 cm⁻¹). These wavenumbers were selected as the result of a brief study to investigate which wavenumbers from this interval were the most sensitive to a change in CO₂ at the particular altitude.

The results of the two sensitivity experiments are given in Figures 6.18 and 6.19. The magnitude of the sensitivities displayed is the result of perturbing the concentration of CO₂ by 1 ppmv at the affected altitude just stated while the rest of the atmosphere remained unchanged.

For the surface albedo test (Figure 6.18), solar zenith angles of $\theta_{\odot} = 0^{\circ}$, 30° , and 45° were used as the surface albedo was varied. From these plots, we observe that the measurements appear to be more sensitive to CO₂ in the mid and upper troposphere where the radiances usually experience a change of between 13 and 17%, whereas they change by only 6 to 8% near the surface. The figures further reveal that the sensitivity to CO₂ begins to show marked variability if the surface albedo falls below 5% and is highly variable for albedo values of 1% or less. Otherwise, the sensitivity remains fairly fixed. As in Figure 6.17, the change in CO₂ sensitivity with changing α is due to Rayleigh scatter. Thus, *these results suggest that a surface albedo*

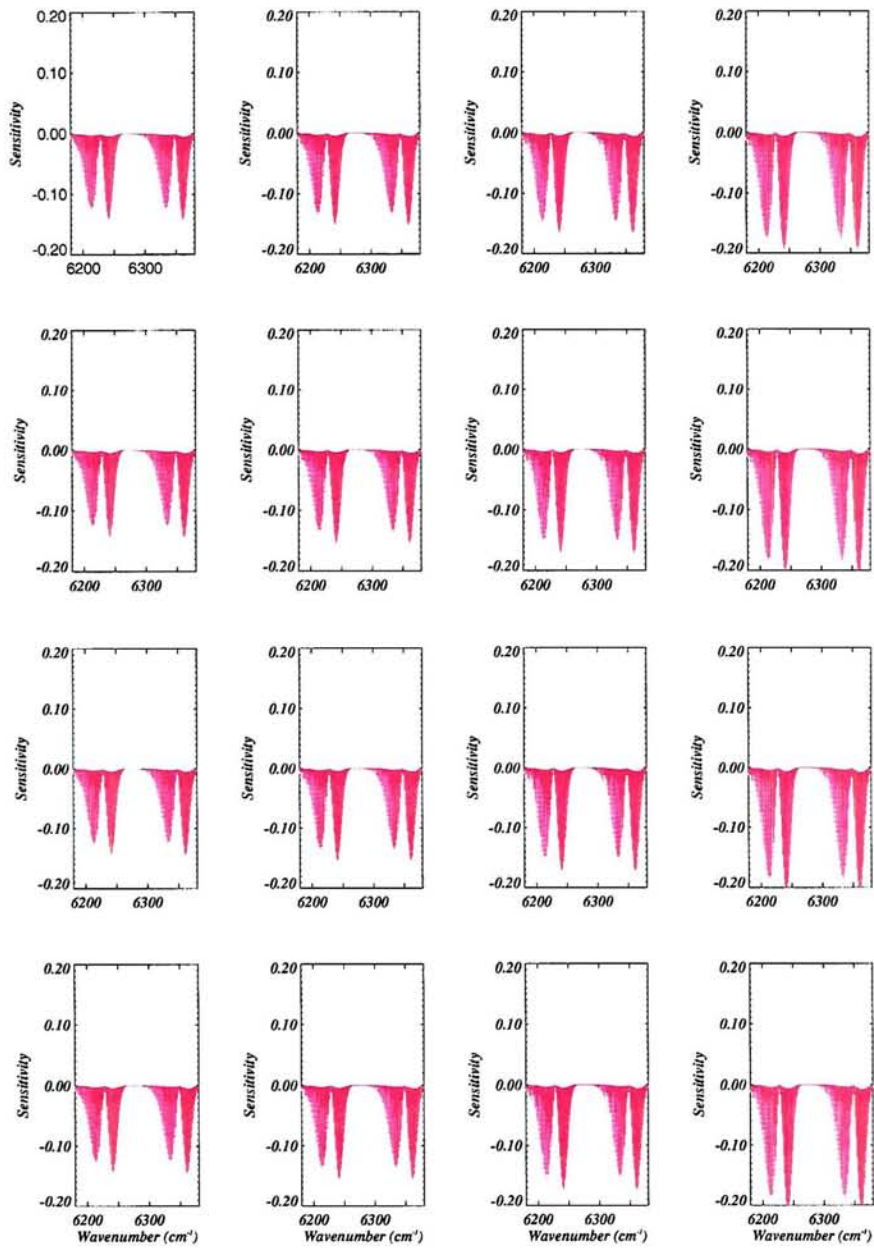


Figure 6.17: Sensitivity of NIR radiances to CO_2 in clear sky scenarios. Each plot corresponds to a CO_2 sensitivity scenario with fixed α and θ_{\odot} . The scenarios in each row took on a fixed value of α corresponding to values of 0.10, 0.25, 0.40, and 0.75 going down the page. The scenarios in each column took on a fixed value of θ_{\odot} corresponding to values of 0° , 30° , 45° , and 60° going across the page from left to right.

of 5% or greater will probably be required to fully take advantage of any benefit the NIR has to offer in retrieving CO₂.

The sensitivity of the radiances to CO₂ mixing ratio with respect to changing solar zenith angle is given in Figure 6.19. It appears to become rather strongly influenced by θ_{\odot} once one moves down beyond between 30° and 50° from the vertical, depending on where you are in the atmosphere. Here, surface albedos of $\alpha = 0.10$, 0.25, and 0.40 were used as θ_{\odot} was varied. In all plots, the sensitivity remains fairly constant out to about 20° or so. A peak in sensitivity occurs as the sun approaches the horizon due to the increase in geometric distance (and the resulting increase in optical path of CO₂) through the which the photons must pass. Beyond this point, the difference in the amount of photons returned from the surface directly to a nadir view given a change in CO₂ concentration is less; thus, the sensitivity approaches zero as one moves to the horizon from this maximum sensitivity.

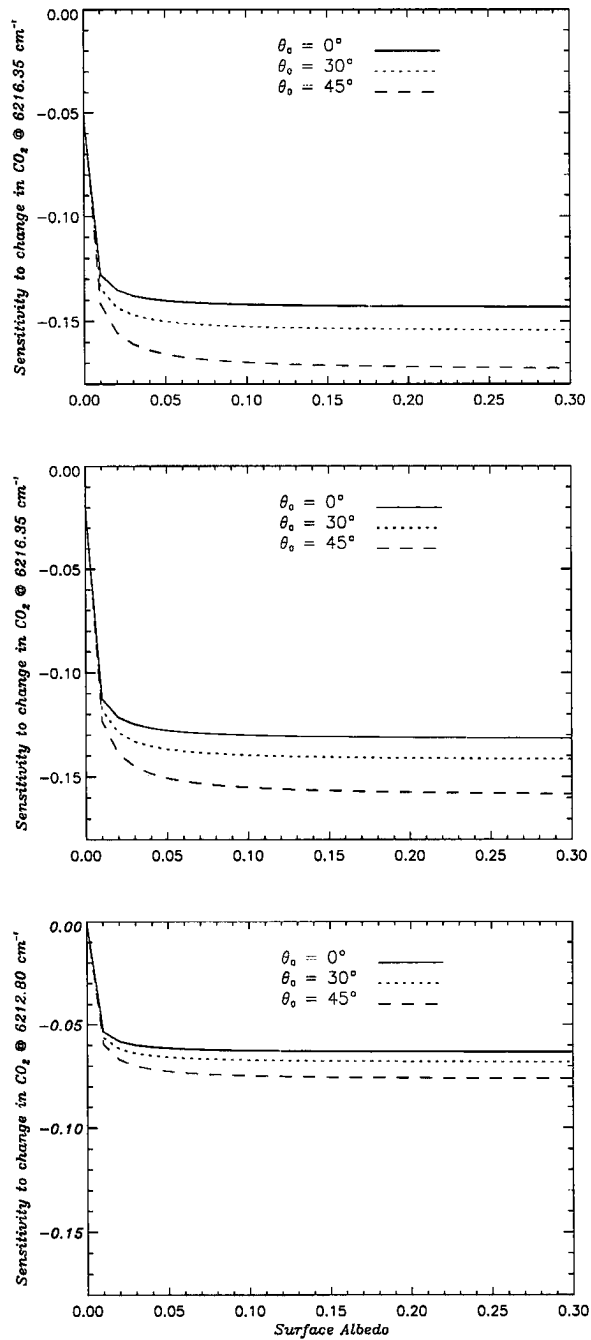


Figure 6.18: Sensitivity of radiances to CO_2 in clear sky for varying values of α for a $1.6 \mu\text{m}$ wavenumber sensitive to CO_2 in the upper troposphere (top panel), the mid-troposphere (middle panel), and the lower troposphere (lower panel).

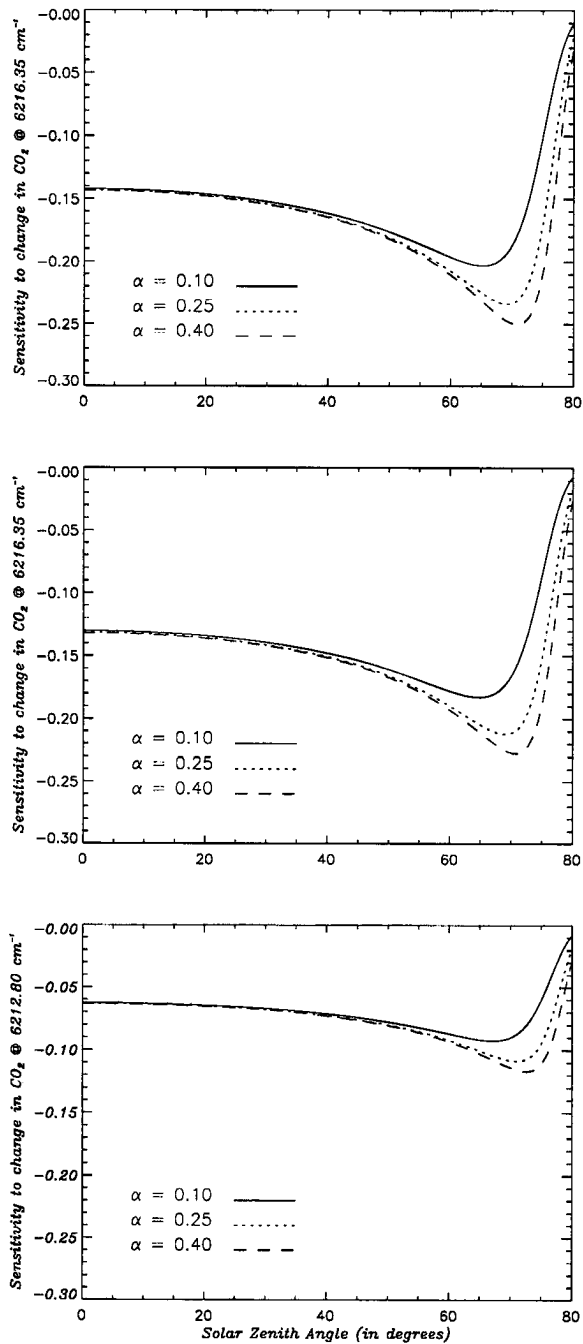


Figure 6.19: Sensitivity of radiances to CO₂ in clear sky for varying values of θ_{\odot} for a 1.6 μm wavenumber sensitive to CO₂ in the upper troposphere (top panel), the mid-troposphere (middle panel), and the lower troposphere (lower panel).

Chapter 7

Retrieval Results

7.1 Retrieving a Profile of CO₂ in Clear Sky

The CO₂ profile used in the retrieval simulations is meant to typify the kind of profile one would expect to find downwind of a source of atmospheric CO₂. It was generated by the Colorado State University GCM and corresponds to the eastern coast of the United States and is the same as used in Engelen et al. (2001). The atmospheric profiles of temperature and pressure as well as density of air, water vapor, and ozone in which the CO₂ profile is embedded are from the Air Force Cambridge Research Lab's "Optical Properties of the Atmosphere" by F.A. McClatchey, et al. and correspond to midlatitude summer conditions. The results of the CO₂ retrievals for clear sky viewing are given in Figures 7.1 - 7.5 along with their associated profiles of retrieval error and averaging kernels.

The figures for clear sky contain either two or three sets of results. The first three figures of this section contain three sets corresponding to retrieval results using measurements from the IR only (upper set), NIR only (middle set), or both (lower set). The remaining two figures provide results using only IR and NIR measurements together.

In each set, the lefthand plots display the actual profile being retrieved as the

thin solid line, the retrieved profile as the thick solid line, and the *a priori* as dotted. In the center plots, the estimated error profile of the retrieval is the thick solid line, the *a priori* error profile the dotted line, and the actual error profile the dashed line. Of course, during normal operation the actual error is unknown, but since we know the profile the retrieval is supposed to be returning, this will be used to see how much the measurements improved our knowledge of the CO₂ profile versus the *a priori*. Lastly, the righthand plots display the averaging kernels of the retrieval on the left with every 5th kernel given as a thick line to assist viewing. We recall that these provide a measure of the spatial resolution of the observing system. Also, the areas of each of the averaging kernel curves for each of the retrieved values of CO₂ are given to the right in these righthand figures. For a retrieved value of CO₂ at a given height, the corresponding value on this righthand curve should be approximately unity if its value is being derived primarily from the measurements.

For these retrievals, the surface albedo and solar zenith angle are assumed known. Also, as in the NIR sensitivity study, the surface albedo is assumed to remain constant across the 18.075 cm⁻¹ spectral band from the 1.6 μm region used for the NIR measurements. This allows us to focus our attention on what role the IR and NIR measurements are contributing to the retrieval as well as the potential problems that can be caused by thin cloud and aerosol.

In the NIR, the instrument is given to have a CO₂ continuum signal-to-noise ratio (SNR) of 400:1 at a surface albedo $\alpha = 0.06$ and solar zenith angle $\theta_{\odot} = 22^{\circ}$. This SNR is similar to that used in Kuang et al. (2002) where they simulate obtaining CO₂ column-averaged values utilizing two CO₂ bands in the NIR as part of their scheme. The instrument here, like in the NIR sensitivity study, is assumed to have a δ -function response for the same reasons given earlier. Also, because of a desire to produce results that can later be compared with Kuang et al. (2002), a surface albedo of $\alpha = 0.06$ was used here to simulate a low albedo ocean rather than the value of 0.05 given earlier in Table 6.2.

Table 7.1: Total degrees of freedom for CO₂ retrievals.

Case	Total Degrees of Freedom
IR ONLY	2033
NIR ONLY	757
IR/NIR	2757

In the IR, the instrument is given to have a SNR of 200:1 at each wavenumber. This is the same as used in Engelen et al. (2001). Furthermore, the atmospheric profiles of temperature, water vapor, and ozone are assumed to be known perfectly; thus, there is no contribution to error in transmission due to these constituents on the measurements in the IR.

As stated earlier in this work, the expression (5.11) is used to compute a χ^2 statistic as a way to test the quality of the retrieval by providing a means to test the accuracy of the given error covariances (assuming a normal distribution). Table 7.1 gives the total number of degrees of freedom (DF) for a retrieval when using measurements from a given spectral region and corresponds to the actual number of measurements from the region(s) used in that retrieval summed with the number of elements in the *a priori* vector. For example, when only the IR portion of the spectrum is used in performing a CO₂ retrieval, 2000 measurements are used along with *a priori* values of CO₂ at 33 levels in the atmosphere; thus, the DF for the retrieval is 2033. If the assumed measurement and *a priori* errors used are reasonable, the value of χ^2 obtained for a given retrieval should fall fairly close to the corresponding DF.

Figures 7.1 - 7.3 show the retrieval results for clear-sky conditions where $\theta_{\odot} = 0^{\circ}$ and α successively takes on the values of 0.06, 0.25, and 0.40 as one proceeds through these first three figures. In each of these figures, the results of retrieving CO₂ using only IR measurements are given in the upper set, using only NIR measurements in the middle set, and using measurements from both IR and NIR in the lower set.

Looking at the IR results in the upper set of Figure 7.1, we observe from part (c) that most of the information about the CO₂ profile is coming from the 1-11 km region of the atmosphere. In this region, the sum of the averaging kernels is 0.5 or

better at each level indicating that the retrieval is relying more on the measurements. Above and below this, the retrieval is relying mostly on the *a priori* profile as indicated by the lower averaging kernel sums. In the region 11-20 km, the *a priori* was fairly accurate due to the small variations in CO₂ that take place in this region and the retrieval did well as a result even though the IR measurements are not sensitive to CO₂ at these altitudes. Below this, as alluded to earlier, use of the IR to discern the presence of CO₂ as one approaches the surface becomes difficult due to a lack of contrast between the temperature of the surface and that of the lower atmosphere. The retrieval again converges to the *a priori* as a result, but here the *a priori* was not as accurate as it was for the higher altitudes and the retrieval errors are largest in this region with an error at the surface of about 8.8 ppmv.

Usually settling at less than 1.0 ppmv, the actual error in most of the profile was rather small down to about 2 km. The estimated retrieval error was larger than this being between 1 ppmv aloft and over 10 ppmv at the surface. The reason that the estimated retrieval errors were so much larger is primarily due to the assumed errors in the *a priori* profile. The χ^2 value obtained for this retrieval (2025) compares favorably with the value of 2033 for the DF given in Table 7.1 for the "IR ONLY" case. If one performed similar retrievals over the same region over a period of days, the previous retrieval data can assist in "tuning" the *a priori* for this locale and one could expect smaller estimated errors on future retrievals.

Next, looking at the NIR results in the middle set of Figure 7.1, we observe that, unlike the IR, the region from which the NIR is receiving its information about CO₂ is lower down in the atmosphere. Here, it is the region from 0-9 km that information about CO₂ is being gathered with information now coming from the surface. As a result, the retrieval maintains smaller errors closer to the surface with a surface error now coming in at 0.8 ppmv. However, the retrieval is not holding the true profile as well as the IR in the free troposphere - in part due to the low surface albedo. The χ^2 value for this retrieval was again good (753) as compared with what

would be expected from Table 7.1 (see "NIR ONLY").

Performing a retrieval with both the IR and NIR measurements, the lower set of Figure 7.1 reveals a result that is arguably better than using the IR only, but not quite as good as the NIR only case just discussed. Under these conditions, the retrieved profile holds the true profile better at midlevels, but with some loss of accuracy in the 0-5 km region. Here, the error in CO₂ concentration at the surface was 5.82 ppmv. The sum of the averaging kernels on the right side of plot (i) show that the retrieval largely takes on the character of the IR under these low albedo conditions. The estimated retrieval errors were also slightly better even given the large assumed *a priori* errors. The χ^2 value here (2754) is comparable with the DF for a "IR/NIR" case as given in Table 7.1.

In Figures 7.2 and 7.3, the upper set is the same IR retrieval as in Figure 7.1 as the IR measurements are not as influenced by changes in surface albedo as the NIR measurements and in these retrievals are assumed not to be affected. It is provided for convenient comparison with the middle and lower sets.

Focusing on the NIR retrieval, we compare the middle set of Figure 7.2 with that of Figure 7.1. Viewing plot (f) of Figure 7.2 we observe that, for a surface albedo $\alpha = 0.25$, the NIR retrieval has more CO₂ information coming in from throughout the lowest 12 km of the atmosphere due to an improved NIR signal-to-noise ratio as a result of stronger surface returns. The result is a slightly larger error of 2.1 ppmv at the surface but with a little tighter fit at midlevels. Including both IR and NIR measurements in these conditions yields a slightly better fit over the IR/NIR case in the previous figure with the error in CO₂ concentration at the surface now coming in at 3.3 ppmv. The estimated errors and values of χ^2 remain nearly the same as previously.

Now, comparing the middle set of Figure 7.3 with that of Figure 7.2 we observe that, for a surface albedo $\alpha = 0.40$, this increase in albedo appears to not have had much effect on the retrieved profile. Including the IR measurements in the lower set

however again results in a slightly tighter fit in the 0-5 km region over the previous IR/NIR case and brings with it a little smaller CO₂ concentration error at the surface of 1.3 ppmv.

From these three cases, we observe that the averaging kernels of the IR/NIR cases move from being more "IR like" in the low albedo case to becoming more "NIR like" as the albedo is increased. With this comes improvement in the quality of the retrieval as one approaches the surface as the NIR plays a larger role due to increased returns from the surface. From this, one can see the potential benefit of "marrying" the IR and the NIR together in performing CO₂ retrievals. Since they emphasize the radiative properties of different parts of the atmosphere, the IR works toward maintaining a better fit to the true profile at midlevels while inclusion of the NIR yields better retrieved values of CO₂ near the surface. Given the assumptions, this appears to be true for a significant range of surface albedo.

Two final comments on these first three figures are in order. First, one might be inclined to use only measurements from the NIR to perform CO₂ retrievals as reasonable profiles were obtained in each case without using the IR at all; however, as we will see in the cases with a scatterer present, this would be a mistake as the IR and NIR can assist in keeping each other in check under such conditions. Second, for the retrievals performed using only the NIR measurements, one may observe from the averaging kernel plots (plot (f) in each figure) that the contribution of the NIR measurements to the retrieval initially peaks at about 2 km in the atmosphere (Figure 7.1). The peak then moves up to about 7 km (Figure 7.2) and then to 8 km (Figure 7.3) as the albedo increases. In addition, a second peak begins to develop in the last case (Figure 7.3). Although needing to be confirmed, this second peak is believed due to information being picked up by the highly resolved measurements being used here from the weaker absorption band of CO₂ below the main band in this region at this higher surface albedo (see this weaker band in the 6203-6221 cm⁻¹ region in part (b) of Figure 2.1).

Table 7.2: Column-average values of CO₂ volume mixing ratio for real, *a priori*, and retrieved profiles along with associated error for clear sky scenarios (see text for explanation).

Profile	α	θ_{\odot}	\bar{q}	$\Delta\bar{q}_{est}$	$\Delta\bar{q}_{act}$
Real	-	-	373.43	-	-
<i>a priori</i> 1	-	-	370.20	± 1.96	-3.23
IR	-	-	372.70	± 1.19	-0.74
NIR	0.06	0	373.25	± 0.29	-0.18
NIR	0.25	0	373.41	± 0.09	-0.03
NIR	0.40	0	373.42	± 0.05	-0.02
IR/NIR	0.06	0	373.25	± 0.26	-0.18
IR/NIR	0.25	0	373.41	± 0.08	-0.02
IR/NIR	0.40	0	373.42	± 0.05	-0.01
IR/NIR	0.06	30	373.22	± 0.29	-0.22
IR/NIR	0.40	30	373.42	± 0.06	-0.01

Now, in addition to these cases where albedo was varied, two clear-sky cases were performed where θ_{\odot} was varied to observe its influence on the retrieved result. From the NIR sensitivity study, we would not expect very much difference in the results if θ_{\odot} is varied between, say, 0° and 30° (recall Figure 6.19). Observing Figures 7.4 and 7.5 where both the IR and NIR are working together to retrieve the profile of CO₂ concentration, we see that it indeed makes little difference. In Figure 7.4, $\alpha = 0.06$ while θ_{\odot} took on the values of 0° (upper set) and 30° (lower set). Both results are practically identical. The results in the sets displayed in Figure 7.5 where $\alpha = 0.40$ and θ_{\odot} again took on the values of 0° (upper set) and 30° (lower set) are also similar. Thus, for a sizeable range of solar zenith angle, the retrievals appear largely unaffected.

Table 7.2 shows the column-average values of CO₂ volume mixing ratio of the real CO₂ profile, the *a priori* 1 profile, and the retrieved profile for each clear-sky scenario simulated in this section. Each of the retrieved profiles are designated by the simulated measurements that were used in retrieving the profile as well as the values of α and θ_{\odot} used in that simulation. Next, the table shows the estimated error $\Delta\bar{q}_{est}$ in the *a priori* and retrieved column-average values obtained using the *a priori* covariance S_a and retrieved covariance S_x , respectively. Lastly, it reveals the actual

error $\Delta\bar{q}_{act}$ in the *a priori* and retrieved column-average values of CO₂ volume mixing ratio for each case. The table shows that, in each case, the difference between the actual column-averaged value and that retrieved was less than 1 ppmv and that the actual difference was less than that estimated from the retrieval covariance matrix S_x .

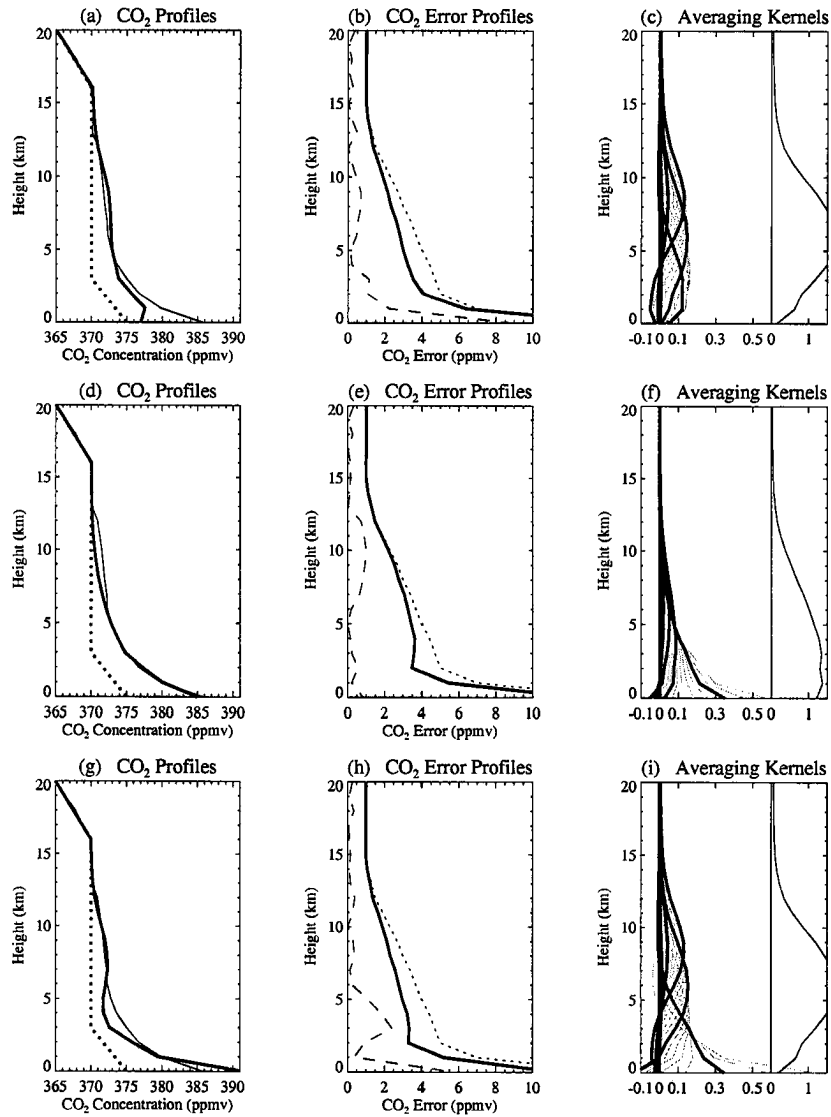


Figure 7.1: Retrieved source profile of CO₂ with associated profiles of error statistics for measurements with $\alpha = 0.06$ and $\theta_{\odot} = 0^{\circ}$. (a,d,g) Real (thin solid), retrieved (thick solid), and *a priori* (dashed) CO₂ profiles; (b,e,h) estimated error (thick solid line), *a priori* error (dotted), and actual error (dashed); (c,f,i) Averaging kernels for retrieval (see text). The upper set resulted from using ONLY IR measurements, the middle set from using ONLY NIR measurements, and lower set from using BOTH IR and NIR measurements. The χ^2 values were 2025 (IR), 753 (NIR), and 2754 (BOTH).

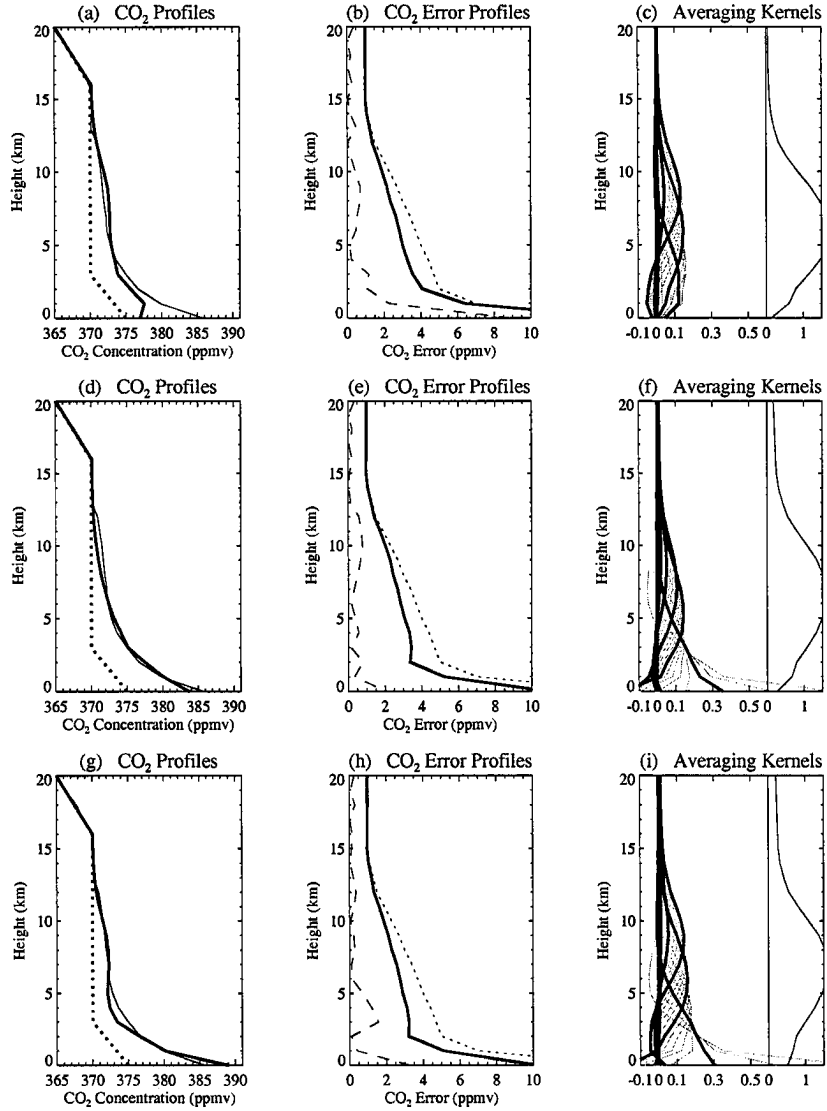


Figure 7.2: Retrieved source profile of CO₂ with associated profiles of error statistics for measurements with $\alpha = 0.25$ and $\theta_{\odot} = 0^{\circ}$. Notation and measurements used to obtain results for each set are the same as Figure 7.1. The χ^2 values were 2025 (IR), 754 (NIR), and 2755 (BOTH).

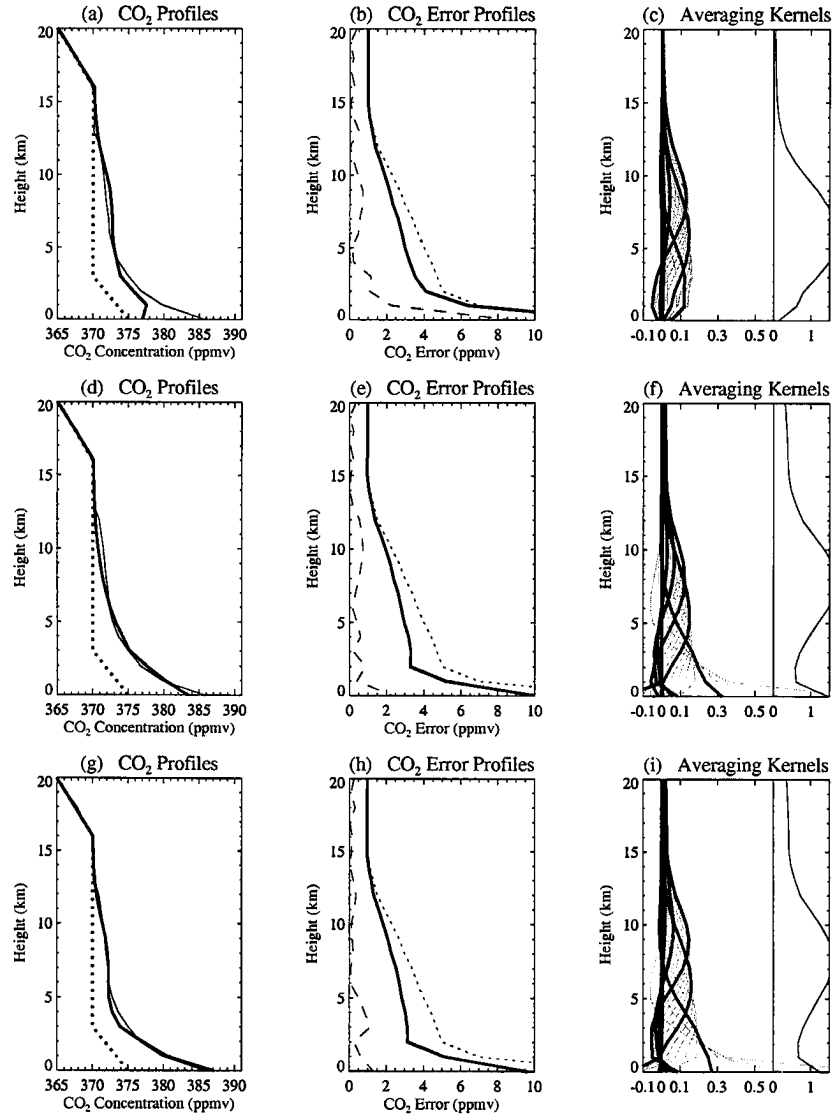


Figure 7.3: Retrieved source profile of CO₂ with associated profiles of error statistics for measurements with $\alpha = 0.40$ and $\theta_{\odot} = 0^{\circ}$. Notation and measurements used to obtain results for each set are the same as Figure 7.1. The χ^2 values were 2025 (IR), 754 (NIR), and 2755 (BOTH).

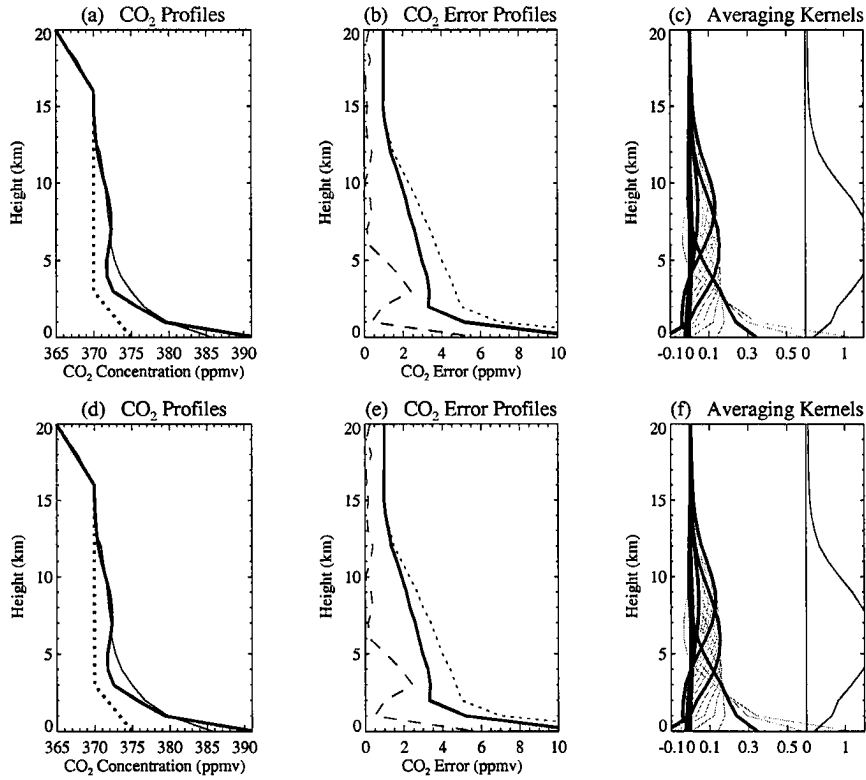


Figure 7.4: Comparison of retrieved source profile of CO₂ with associated profiles of error statistics for measurements where $\alpha = 0.06$ and $\theta_{\odot} = 0^{\circ}$ (upper set) and $\alpha = 0.06$ and $\theta_{\odot} = 30^{\circ}$ (lower set). Notation and measurements used to obtain results for each set are the same as Figure 7.1. The χ^2 value was 2754 for both upper and lower sets.

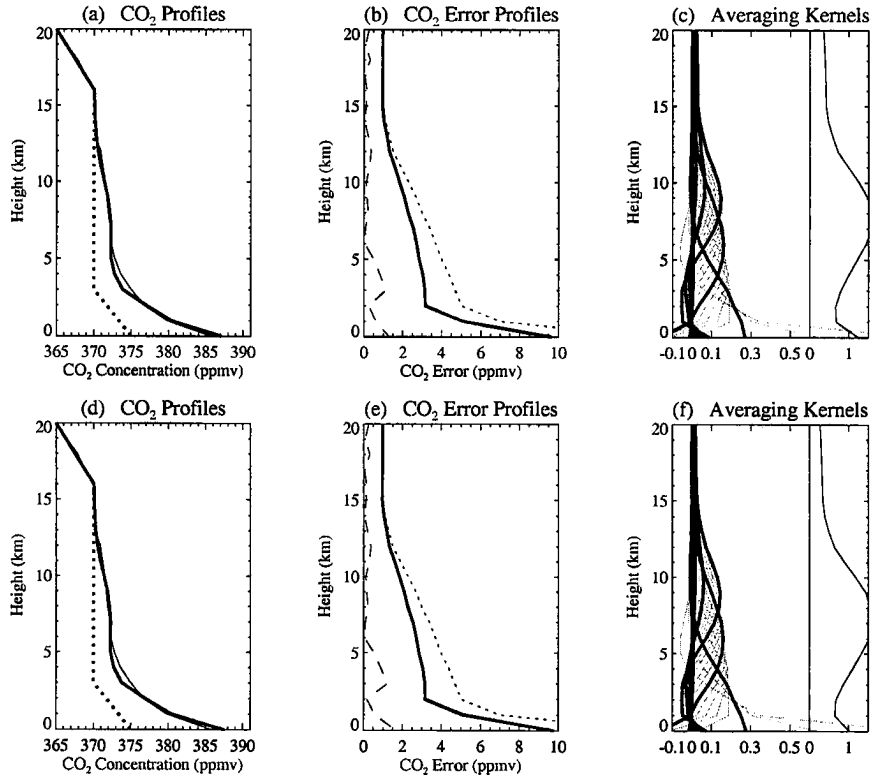


Figure 7.5: Comparison of retrieved source profile of CO₂ with associated profiles of error statistics for measurements where $\alpha = 0.40$ and $\theta_{\odot} = 0^{\circ}$ (upper set) and $\alpha = 0.40$ and $\theta_{\odot} = 30^{\circ}$ (lower set). Notation and measurements used to obtain results for each row are the same as Figure 7.1. The χ^2 value was 2755 for both upper and lower sets.

7.2 Retrieving a Profile of CO₂ in the Presence of Thin Cirrus

The results of retrieving the CO₂ source profile in the presence of a thin cirrus layer are given in Figures 7.6 - 7.10 along with the associated profiles of retrieval error and averaging kernels. For this part of the study, a cirrus cloud was placed at 13 km in the atmosphere with an optical depth $\tau = 0.1$ in the 1.6 μm region of the NIR. Since the amount of scattering in the IR is small, the cloud was approximated in the IR by a totally absorbing layer. The optical depth of the cloud in the IR was assigned based on this approximation and on the ratio of absorption to extinction efficiency as one moves into the IR portion of the spectrum ($\approx \frac{1}{2}$). Using this, τ is assigned a fixed value of 0.05 across the IR. The cloud was chosen to have an asymmetry factor of $g = 0.77$ and a single scatter albedo of $\omega_o = 0.97$ in the NIR. This corresponds to a cirrus cloud with ice crystals with a mean effective size of 10 μm (Lynch et al., 2002).

Figure 7.6 shows the results for a set of four retrievals when $\alpha = 0.06$ and $\theta_{\odot} = 0^{\circ}$, Figure 7.7 the results for an additional set of four retrievals when $\alpha = 0.40$ and $\theta_{\odot} = 0^{\circ}$, and Figure 7.8 for a set of four retrievals when $\alpha = 0.06$ and $\theta_{\odot} = 30^{\circ}$. Both the IR and the NIR were used together here to retrieve the profile of CO₂ concentration. In these plots, as in previous retrieval figures, the lefthand plots contain the real (thin solid), retrieved (thick solid), and *a priori* (dashed) CO₂ profiles, the middle plots the estimated (thick solid), *a priori* (dotted), and actual (dashed) CO₂ concentration errors and the righthand plots the averaging kernels for the retrieval.

As just mentioned, the first three figures in this section come in sets of four cases each. In each figure, case 1 shows CO₂ retrieval results when the cloud has been precisely determined in both optical depth and altitude, case 2 the results in the extreme case when neither the optical depth nor the altitude of the cloud is known, case 3 the results when the optical depth of the cloud has been precisely determined, but the altitude has been determined to be 1 km lower than truth, and case 4 the

results when the optical depth of the cloud has been determined to be 10% higher than truth, but the altitude has been precisely determined. In each case, except case 2 where the cloud is undetected, the optical properties of the cloud are assumed well-described.

In these three figures, case 1 used the *a priori* with the assumed larger error near the surface (i.e. *a priori 1* - recall discussion of this in section 5.2) as the optical depth and altitude of the scattering layer is assumed well known and its influence on the retrieval therefore minimal. This allows the measurements to be "in the driver's seat" as it were. However, in cases 2-4 where the optical depth and/or altitude of the scatterer is not well known, the *a priori* with the assumed smaller error near the surface (i.e. *a priori 2*) is used to assist in constraining the retrieval as the measurements suffer degradation in these more adverse conditions.

Case 1 (upper set) in part (i) of Figures 7.6 - 7.8 show the results when the cloud has been precisely determined in both optical depth and altitude. If one compares these results with the associated clear-sky results in the third row of Figures 7.1 and 7.3 and the second row of Figure 7.4, one will see that the results are basically unchanged. This is the ideal situation. Unfortunately, what is really experienced is less than that and some error in determining the optical depth or altitude of the cloud is expected.

In contrast to case 1 in these figures, case 2 (lower set) shows the results in the extreme case when neither the optical depth nor the altitude of the simulated cloud is known (i.e. the cloud is not detected at all). In this case, the scattering of the undetected cloud has dealt the retrieval a serious blow when $\alpha = 0.06$ and has a debilitating influence even when $\alpha = 0.40$. Given the potential magnitude of this effect, *some mechanism for detecting such a subvisual cloud must be used if the retrieval of profiles of CO₂ concentrations is to be made with a reasonable degree of accuracy under such conditions.*

For the next step in the study, it is assumed that there is such a mechanism -

Table 7.3: Column-average values of CO₂ volume mixing ratio for real, *a priori*, and retrieved profiles along with associated error in scenarios with a thin cirrus layer.

Profile	α	θ_{\odot}	Case	\bar{q}	$\Delta\bar{q}_{est}$	$\Delta\bar{q}_{act}$
Real	-	-	-	373.43	-	-
<i>a priori</i> 1	-	-	-	370.20	± 1.96	-3.23
IR/NIR	0.06	0	1	373.25	± 0.26	-0.19
IR/NIR	0.40	0	1	373.42	± 0.05	-0.01
IR/NIR	0.06	30	1	373.21	± 0.29	-0.22
<i>a priori</i> 2	-	-	-	370.20	± 1.36	-3.23
IR/NIR	0.06	0	2	370.65	± 0.74	-2.78
IR/NIR	0.40	0	2	375.24	± 1.28	+1.80
IR/NIR	0.06	30	2	370.92	± 1.34	-2.52
IR/NIR	0.06	0	3	372.61	± 0.64	-0.82
IR/NIR	0.40	0	3	373.48	± 0.04	+0.04
IR/NIR	0.06	30	3	372.49	± 0.67	-0.94
IR/NIR	0.06	0	4	376.36	± 0.67	+2.93
IR/NIR	0.40	0	4	371.02	± 0.04	-2.41
IR/NIR	0.06	30	4	377.56	± 0.83	+4.12

albeit an imperfect one. Case 3 (upper set) in part (ii) of Figures 7.6 - 7.8 show the results of the case where the optical depth of the cloud has been precisely determined, but altitude has been determined to be 1 km lower than truth. Here we see that the retrievals have not suffered the devastating effects of the previous scenario; however, plot (g) in these figures shows that the retrieved profile does not hold the true profile as tightly as before with errors in CO₂ surface concentration between 4-6 ppmv.

Lastly, case 4 (lower set) in part (ii) of Figures 7.6 - 7.8 show the results of the case where the optical depth of the cloud has been determined to be 10% higher than truth, but the altitude has been precisely determined. Unlike the previous scenario, the presence of these errors have had a more significant impact on the retrievals with the result in Figure 7.7 possibly being mistaken as a CO₂ sink profile rather than a source profile. The affect of these errors could be potentially more serious for the effective retrieval of CO₂. Here, the error in the optical depth of the cloud was only 0.01.

Like the clear-sky simulations, Table 7.3 shows the column-average values of

Table 7.4: Column-average values of CO₂ volume mixing ratio for retrieved profiles in CASE 3 and CASE 4 using measurements from the IR only, NIR only, and both along with associated error in scenarios with a thin cirrus layer when $\alpha = 0.06$ and $\theta_{\odot} = 0^{\circ}$.

Profile	Case	\bar{q}	$\Delta\bar{q}_{est}$	$\Delta\bar{q}_{act}$
Real	-	373.43	-	-
<i>a priori 2</i>	-	370.20	± 1.36	-3.23
IR	3	371.85	± 0.75	-1.58
NIR	3	372.93	± 0.34	-0.51
IR/NIR	3	372.61	± 0.64	-0.82
IR	4	372.18	± 0.75	-1.25
NIR	4	377.41	± 0.50	+3.98
IR/NIR	4	376.36	± 0.67	+2.93

CO₂ volume mixing ratio of the real CO₂ profile, the *a priori* profile used (case 1 used *a priori 1* and cases 2-4 *a priori 2*), and the retrieved profile for each scenario simulated with the thin cirrus layer. Along with these is the estimated error in the *a priori* and retrieved column-average values obtained using the *a priori* covariance S_a and retrieved covariance S_x , respectively. It also reveals the actual error in the retrieved column-average values of CO₂ volume mixing ratio.

Here, when the optical depth and height of the cloud is known (case 1), the actual errors were under 1 ppmv and smaller than those estimated for the given retrieval. Errors in case 3 were similar (when the optical depth was assumed known, but an error of 1 km in cirrus height was assumed). Unlike these, cases 2 and 4 suffered more with larger actual errors overall and larger than estimated. Despite this, almost all of the retrievals had actual errors less than their respective *a priori* profiles with 6 out of 9 roughly equal to or less than the 2.5 ppmv required for them to be useful in CO₂ source/sink inversion modeling.

As evidence of the benefit of using measurements from the IR and NIR together in retrieving CO₂ profiles, Figures 7.9 and 7.10 are provided along with Table 7.4. Figure 7.9 reveals what would have happened on case 3 when $\alpha = 0.06$ and $\theta_{\odot} = 0^{\circ}$ if IR or NIR had been used alone while Figure 7.10 shows the same for case 4. In Figure 7.9, the retrieval using only the NIR outperforms the one using only the

IR, while Figure 7.10 demonstrates the opposite. This can be more clearly seen in observing the resulting errors in the column-averaged values in Table 7.4. Working together, the IR and NIR measurements provide more stable performance.

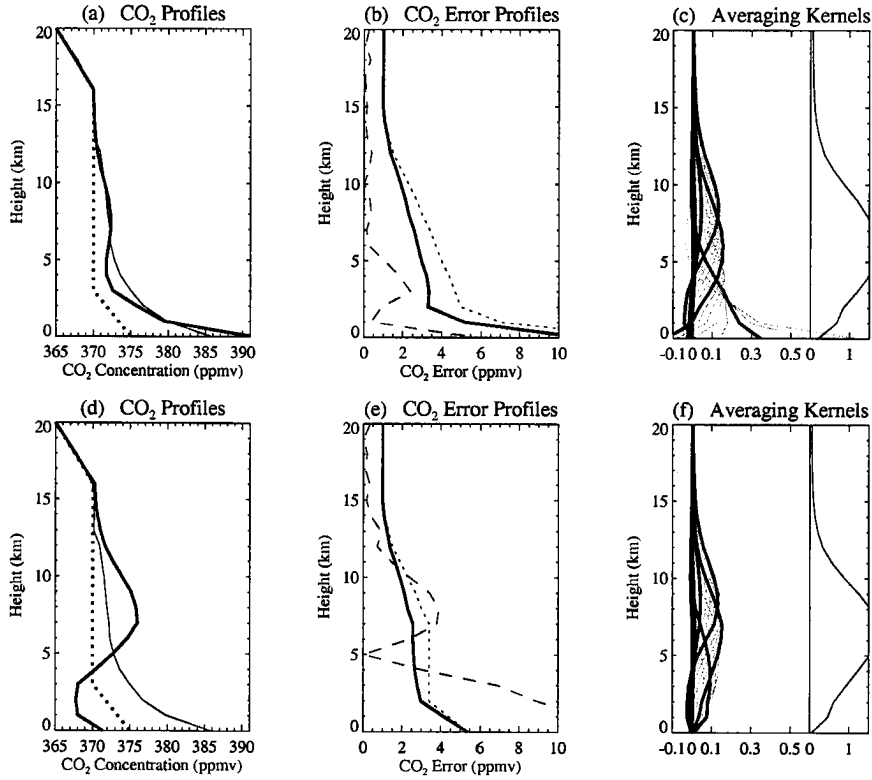


Figure 7.6: (i) Retrieved source profile of CO₂ with associated profiles of error statistics obtained by using both IR and NIR measurements in the presence of a cirrus cloud at 13 km with $\tau = 0.1$ where $\alpha = 0.06$ and $\theta_{\odot} = 0^{\circ}$. Illustrated is CASE 1 (upper set) where both the optical depth and altitude of the cloud are known precisely and CASE 2 (lower set) where both are unknown. Here, (a,d) Real (thin solid), retrieved (thick solid), and *a priori* (dashed) CO₂ profiles; (b,e) estimated error (thick solid line), *a priori* error (dotted), and actual error (dashed); (c,f) Averaging kernels for retrieval (see text). The χ^2 values were 2754 (upper set) and 2750 (lower set).

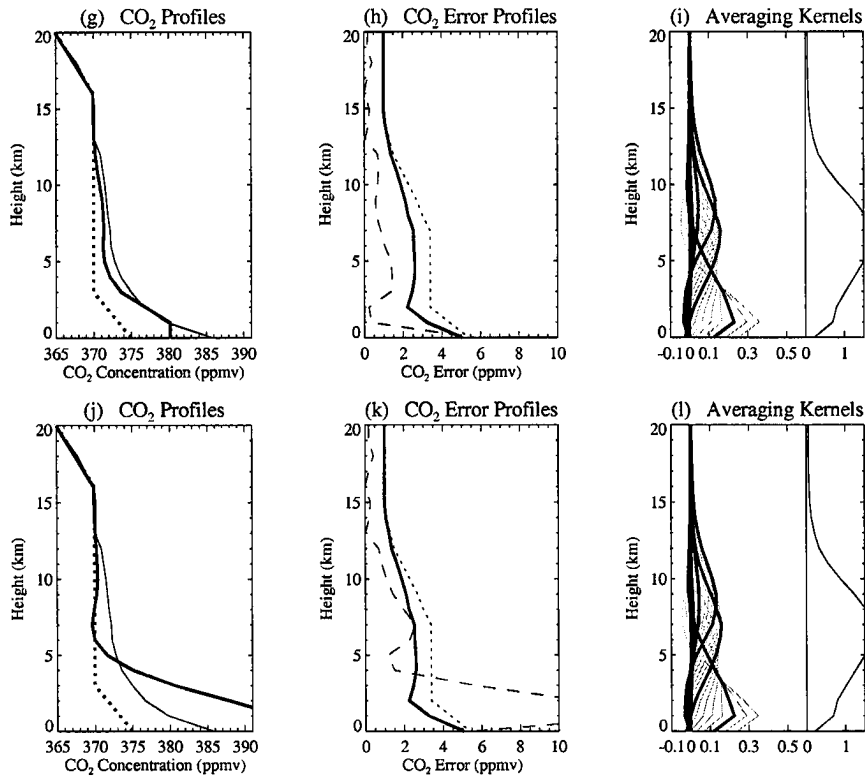


Figure 7.6: (cont'd) (ii) Retrieved source profile of CO₂ with associated profiles of error statistics obtained by using both IR and NIR measurements in the presence of a cirrus cloud at 13 km with $\tau = 0.1$ where $\alpha = 0.06$ and $\theta_{\odot} = 0^{\circ}$. Illustrated is CASE 3 (upper set) where the optical depth is known precisely, but the altitude has been estimated to be 1 km lower than truth and CASE 4 (lower set) where the optical depth has been estimated 10% too high, but the altitude is precisely known. Notation is the same as first part of this figure. The χ^2 values were 2735 (upper set) and 2745 (lower set).

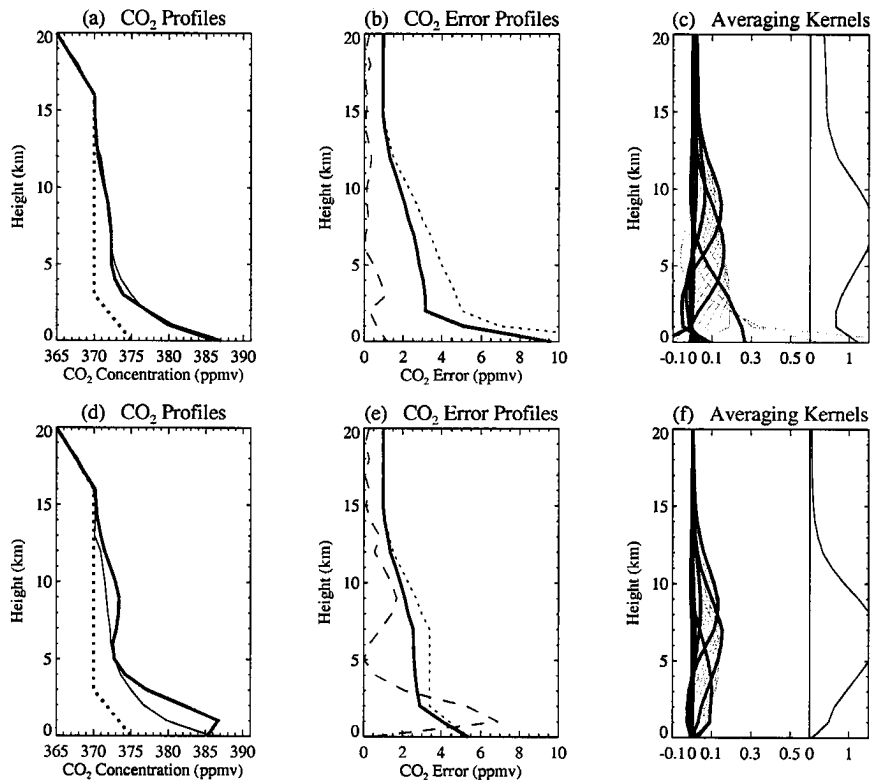


Figure 7.7: (i) Same as CASE 1 (upper set) and CASE 2 (lower set) of Figure 7.6 except that $\alpha = 0.40$ and $\theta_{\odot} = 0^{\circ}$. The χ^2 values were 2755 (upper set) and 2733 (lower set).

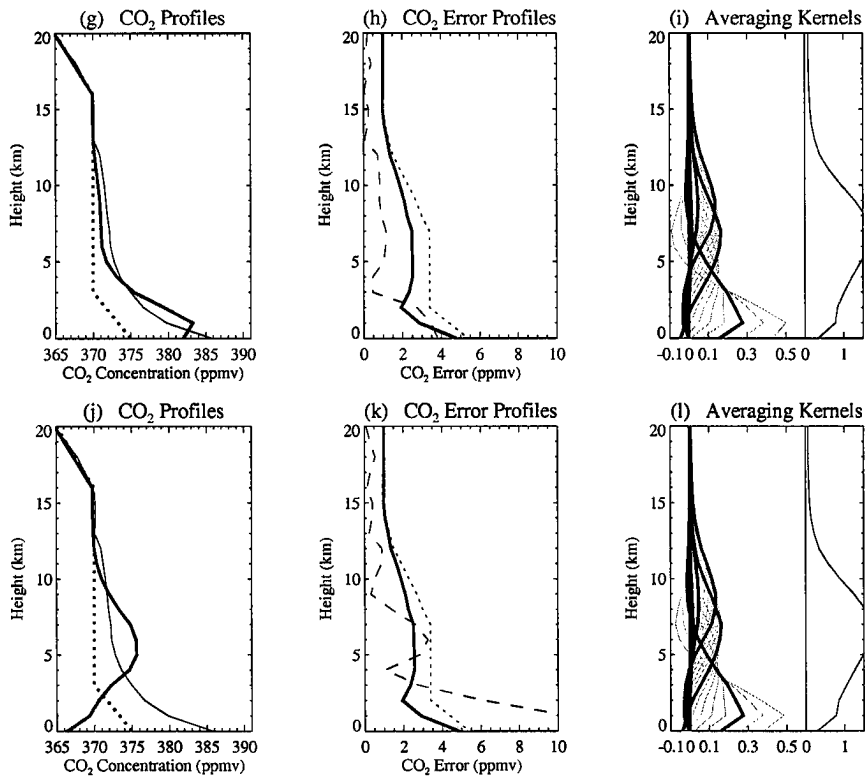


Figure 7.7: (cont'd) (ii) Same as CASE 3 (upper set) and CASE 4 (lower set) of Figure 7.6 except that $\alpha = 0.40$ and $\theta_{\odot} = 0^{\circ}$. The χ^2 values were 2743 (upper set) and 2751 (lower set).

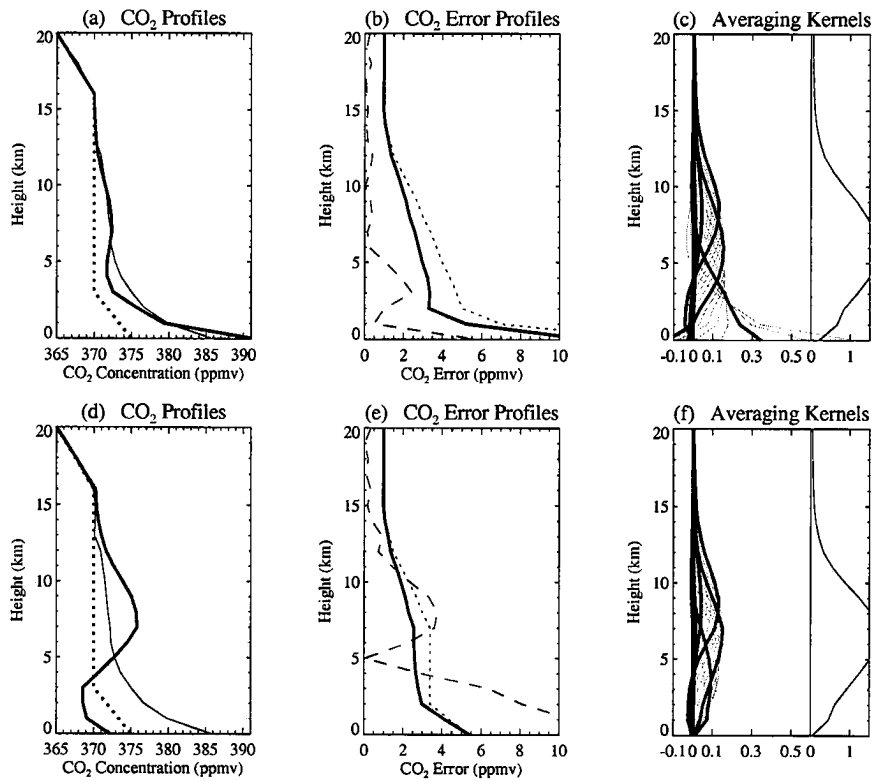


Figure 7.8: (i) Same as CASE 1 (upper set) and CASE 2 (lower set) of Figure 7.6 except that $\alpha = 0.06$ and $\theta_{\odot} = 30^{\circ}$. The χ^2 values were 2754 (upper set) and 2744 (lower set).

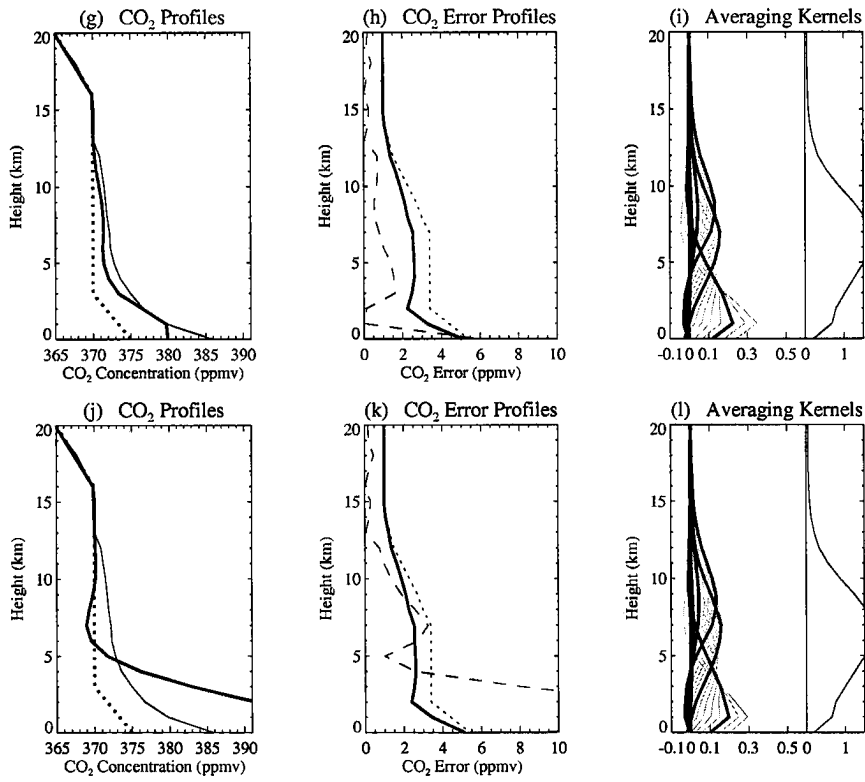


Figure 7.8: (cont'd) (ii) Same as CASE 3 (upper set) and CASE 4 (lower set) of Figure 7.6 except that $\alpha = 0.06$ and $\theta_{\odot} = 30^{\circ}$. The χ^2 values were 2741 (upper set) and 2758 (lower set).

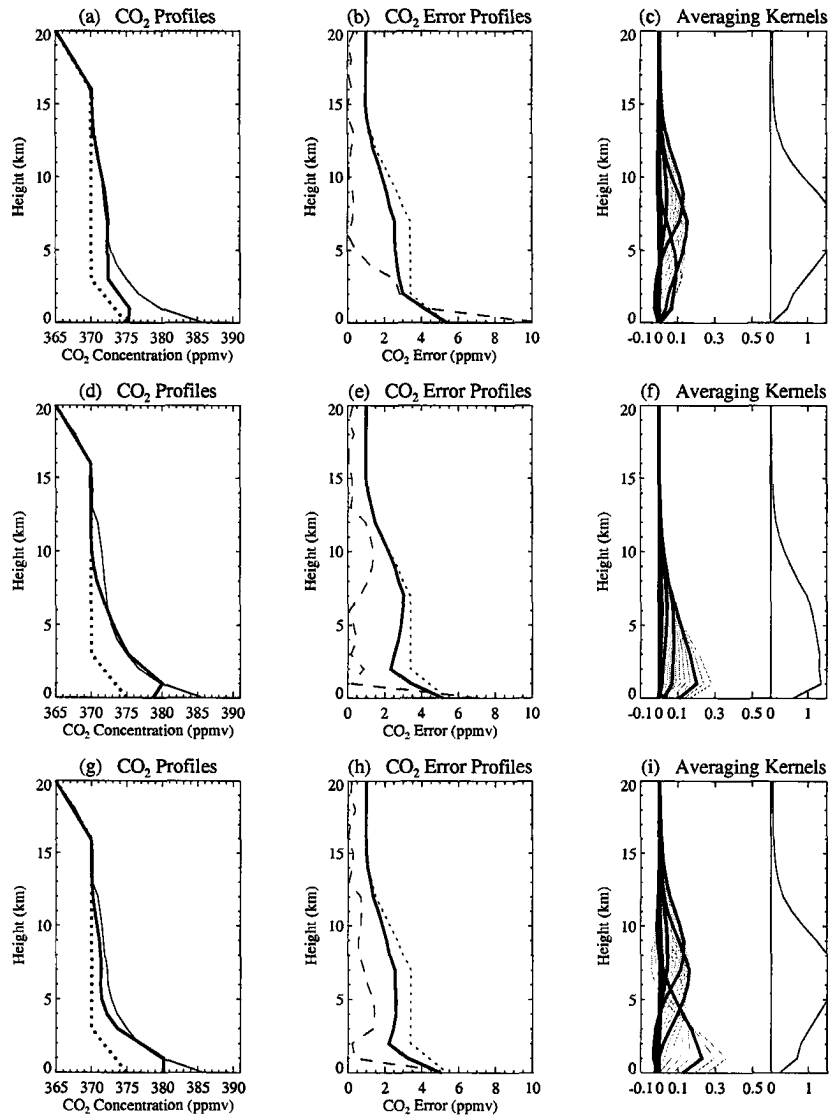


Figure 7.9: Retrieved source profile of CO₂ for CASE 3 with associated profiles of error statistics for measurements with $\alpha = 0.06$ and $\theta_{\odot} = 0^{\circ}$. (a,d,g) Real (thin solid), retrieved (thick solid), and *a priori* (dashed) CO₂ profiles; (b,e,h) estimated error (thick solid line), *a priori* error (dotted), and actual error (dashed); (c,f,i) Averaging kernels for retrieval (see text). The upper set resulted from using ONLY IR measurements, the middle set from using ONLY NIR measurements, and lower set from using BOTH IR and NIR measurements. The χ^2 values were 2029 (IR), 758 (NIR), and 2735 (BOTH).

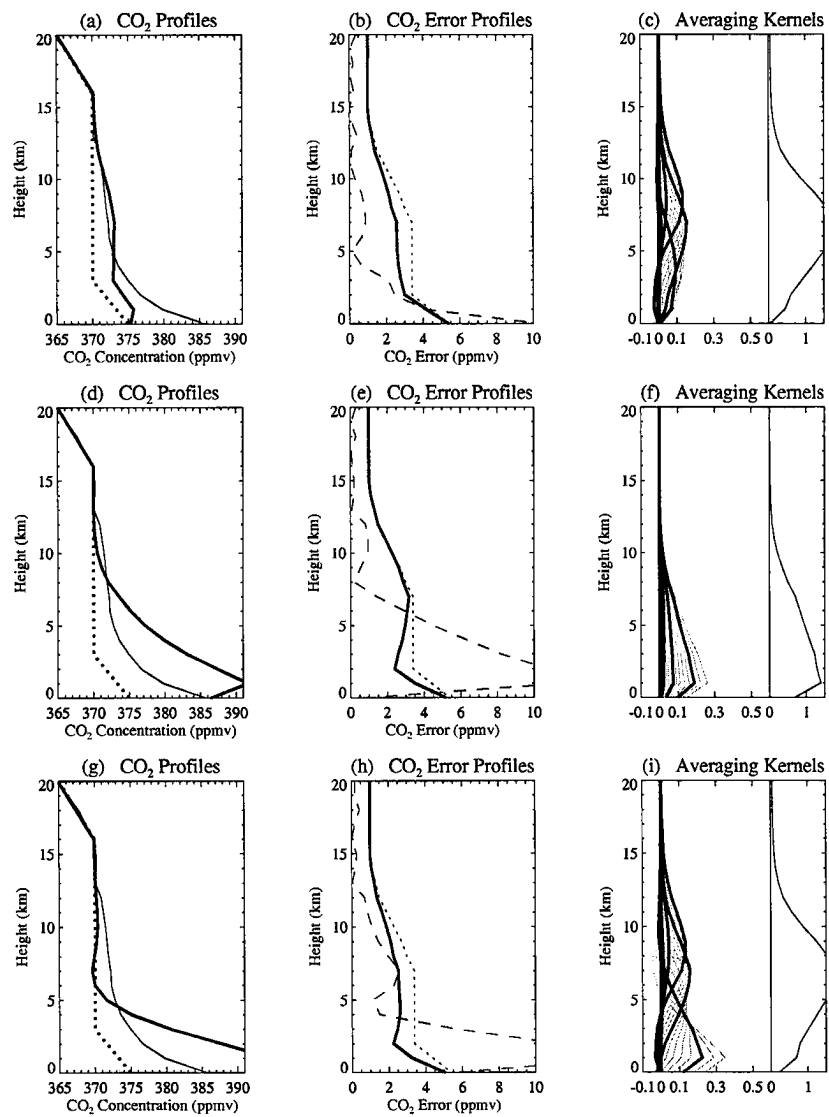


Figure 7.10: Same as Fig 7.9 except for CASE 4. The χ^2 values were 2024 (IR), 758 (NIR), and 2745 (BOTH).

7.3 Retrieving a Profile of CO₂ in the Presence of Thin Aerosol

The results of retrieving the CO₂ source profile in the presence of a thin aerosol layer are given in Figures 7.11 - 7.15 along with the associated profiles of retrieval error and averaging kernels. For this part of the study, the aerosol layer was placed at 2 km in the lower atmosphere with $\tau = 0.2$ in the NIR. In addition, τ was assigned a value half of that in the IR for the same reasons given in the previous section. The aerosol was assumed to have an asymmetry factor of $g = 0.75$ and a single scatter albedo of $\omega_o = 1.00$. These are the same optical properties that were assumed in the NIR sensitivity study. As in the cirrus cases, both the IR and the NIR were used together to retrieve the profile of CO₂ concentration in the first three figures. The notation in these plots is the same as in previous retrievals.

The figures in this section reveal the results for the same values of α and θ_{\odot} as in the thin cirrus cases: Figure 7.11 shows results for when $\alpha = 0.06$ and $\theta_{\odot} = 0^{\circ}$, Figure 7.12 the results for when $\alpha = 0.40$ and $\theta_{\odot} = 0^{\circ}$, and Figure 7.13 for when $\alpha = 0.06$ and $\theta_{\odot} = 30^{\circ}$. These results are described next.

Case 1 (upper set) in Figures 7.11 - 7.13 show the results when the aerosol layer has been precisely determined in both optical depth and altitude. If one compares these results with the associated clear-sky results in the third row of Figures 7.1 and 7.3 and the second row of Figure 7.4, one will again observe that the results are basically unchanged for this ideal situation.

Unlike the cases for thin cirrus, the results for the case when neither the optical depth nor altitude of the simulated aerosol layer is known are not shown. This is because the retrieval gave extremely poor results. This again underscores the importance of having a mechanism for detecting such an aerosol layer.

As in the cirrus set, two additional types of scenarios were assumed using this aerosol layer. Case 2 (middle set) in Figures 7.11 - 7.13 show the results of the case

where the optical depth of the aerosol has been precisely determined, but altitude has been determined to be 1 km lower than truth. Unlike the cirrus set, we see that the retrievals have been more seriously affected. This is due partly to the magnitude of the aerosol's optical depth as well as its position in the atmosphere. In a similar experiment (not shown), when the aerosol was assigned an optical depth of 0.1 with the same altitude, the results were not as poor as in this case, but were worse than in the cirrus case where the optical depth was also 0.1, but its location was at 13 km. It is believed that the difference is mainly due to the assistance that the IR measurements provide in tandem with the NIR measurements at the 13 km altitude, whereas the NIR measurements are acting more alone near the surface and the retrieval is more sensitive to scatter as a result.

One additional observation from this middle set of retrievals: it appears that the error in determining the height of the aerosol at this location in the atmosphere has also allowed the retrieval to become slightly more sensitive to θ_{\odot} . If one compares the results between Figures 7.11 and 7.13, one observes that the errors are worse in the latter case. This appears to be due to an apparent change in optical path of CO₂ caused by increased scatter in the aerosol layer from the increased angle between the sun and the vertical.

Lastly, case 3 (lower set) in Figures 7.11 - 7.13 show the results of the case where the optical depth of the aerosol has been determined to be 10% higher than truth, but the altitude has been precisely determined. Here, the retrievals have returned a CO₂ profile that is not as good as the ideal case, but still respectable.

The column-averaged values and the errors associated with these retrievals are given in Table 7.5. Here, except for the case 2 when $\alpha = 0.40$ and $\theta_{\odot} = 0^{\circ}$, the actual errors in the retrieved column-averaged values are all less than the required 2.5 ppmv.

To complete this preliminary study, Figures 7.14 and 7.15 are provided along with Table 7.6. Figure 7.14 reveals what would have happened on case 2 when $\alpha = 0.06$ and $\theta_{\odot} = 0^{\circ}$ if IR or NIR had been used alone while Figure 7.15 shows the same

Table 7.5: Column-average values of CO₂ volume mixing ratio for real, *a priori*, and retrieved profiles along with associated error in scenarios with a thin aerosol layer.

Profile	α	θ_{\odot}	Case	\bar{q}	$\Delta\bar{q}_{est}$	$\Delta\bar{q}_{act}$
Real	-	-	-	373.43	-	-
<i>a priori</i> 1	-	-	-	370.20	± 1.96	-3.23
IR/NIR	0.06	0	1	373.27	± 0.25	-0.17
IR/NIR	0.40	0	1	373.41	± 0.05	-0.03
IR/NIR	0.06	30	1	373.25	± 0.28	-0.19
<i>a priori</i> 2	-	-	-	370.20	± 1.36	-3.23
IR/NIR	0.06	0	2	373.27	± 0.79	-0.16
IR/NIR	0.40	0	2	378.45	± 0.20	+5.02
IR/NIR	0.06	30	2	372.69	± 0.81	-0.75
IR/NIR	0.06	0	3	375.64	± 1.29	+2.20
IR/NIR	0.40	0	3	373.30	± 0.14	-0.13
IR/NIR	0.06	30	3	374.83	± 1.31	+1.40

Table 7.6: Column-average values of CO₂ volume mixing ratio for retrieved profiles in CASE 2 and CASE 3 using measurements from the IR only, NIR only, and both along with associated error in scenarios with a thin aerosol layer when $\alpha = 0.06$ and $\theta_{\odot} = 0^{\circ}$.

Profile	Case	\bar{q}	$\Delta\bar{q}_{est}$	$\Delta\bar{q}_{act}$
Real	-	373.43	-	-
<i>a priori</i> 2	-	370.20	± 1.36	-3.23
IR	2	373.86	± 0.78	-0.42
NIR	2	372.72	± 0.31	-0.71
IR/NIR	2	373.27	± 0.79	-0.16
IR	3	371.43	± 0.76	-2.00
NIR	3	382.61	± 1.21	+9.18
IR/NIR	3	375.64	± 1.29	+2.20

for case 3. Both figures again demonstrate the benefit of using the IR measurements along with the NIR. Although the retrieval in Figure 7.14 using only the NIR has a generally better fit than the one using both the IR and NIR together, the column-averaged value turns out better for the retrieved profile when both are used together (see Table 7.6). The value of adding the IR is even more pronounced in Figure 7.15. Whereas the retrieved profile using the NIR only is basically nonsense due to the aerosol scatter, the additional IR measurements has made possible a resulting profile that is much more indicative of the character of the true profile. The resulting errors in the column-averaged values for these six retrievals is given in Table 7.6. Once again,

the table gives some evidence that the IR and NIR provide more stable performance when working together.

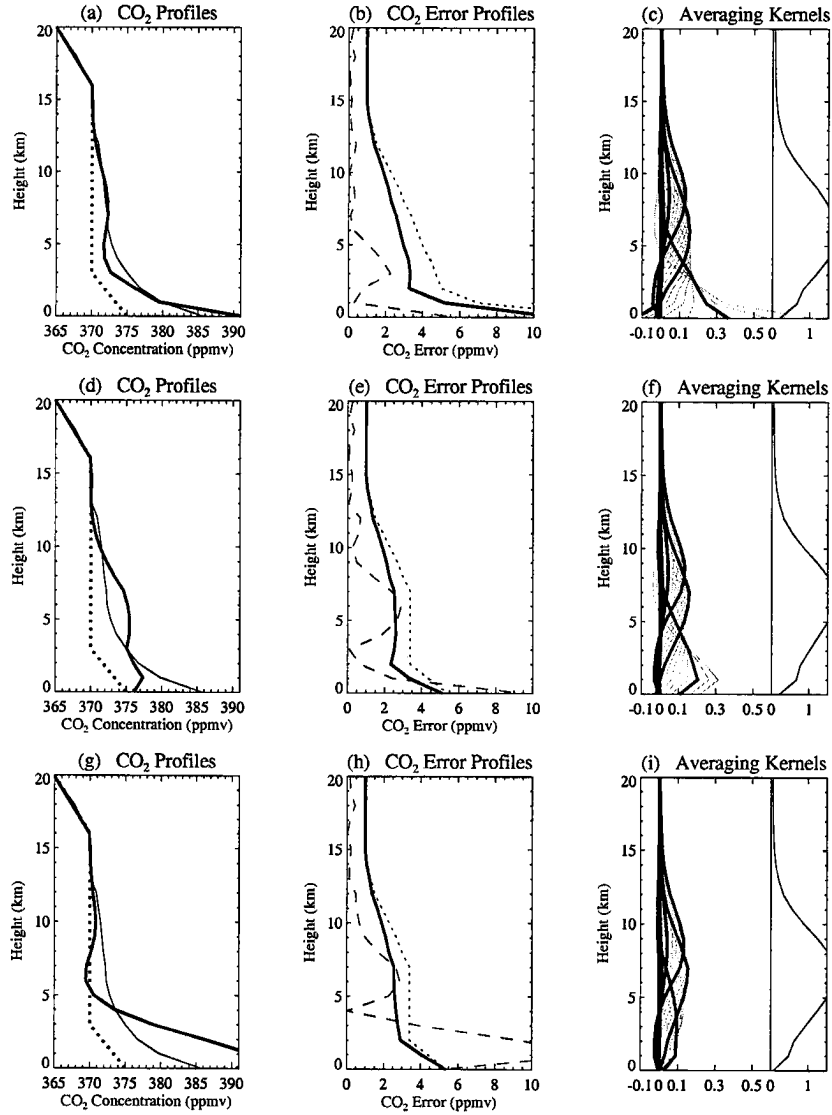


Figure 7.11: Retrieved source profile of CO₂ with associated profiles of error statistics obtained by using both IR and NIR measurements in the presence of an aerosol layer at 2 km with $\tau = 0.2$ where $\alpha = 0.06$ and $\theta_{\odot} = 0^{\circ}$. Illustrated is CASE 1 (upper set) where both the optical depth and altitude of the aerosol are known precisely, CASE 2 (middle set) where the optical depth is known precisely, but the altitude has been estimated to be 1 km lower than truth, and CASE 3 (lower set) where the optical depth has been estimated 10% too high, but the altitude is precisely known. Notation is the same as in previous figures. The χ^2 values were 2754 (upper set), 2744 (middle set), and 2756 (lower set).

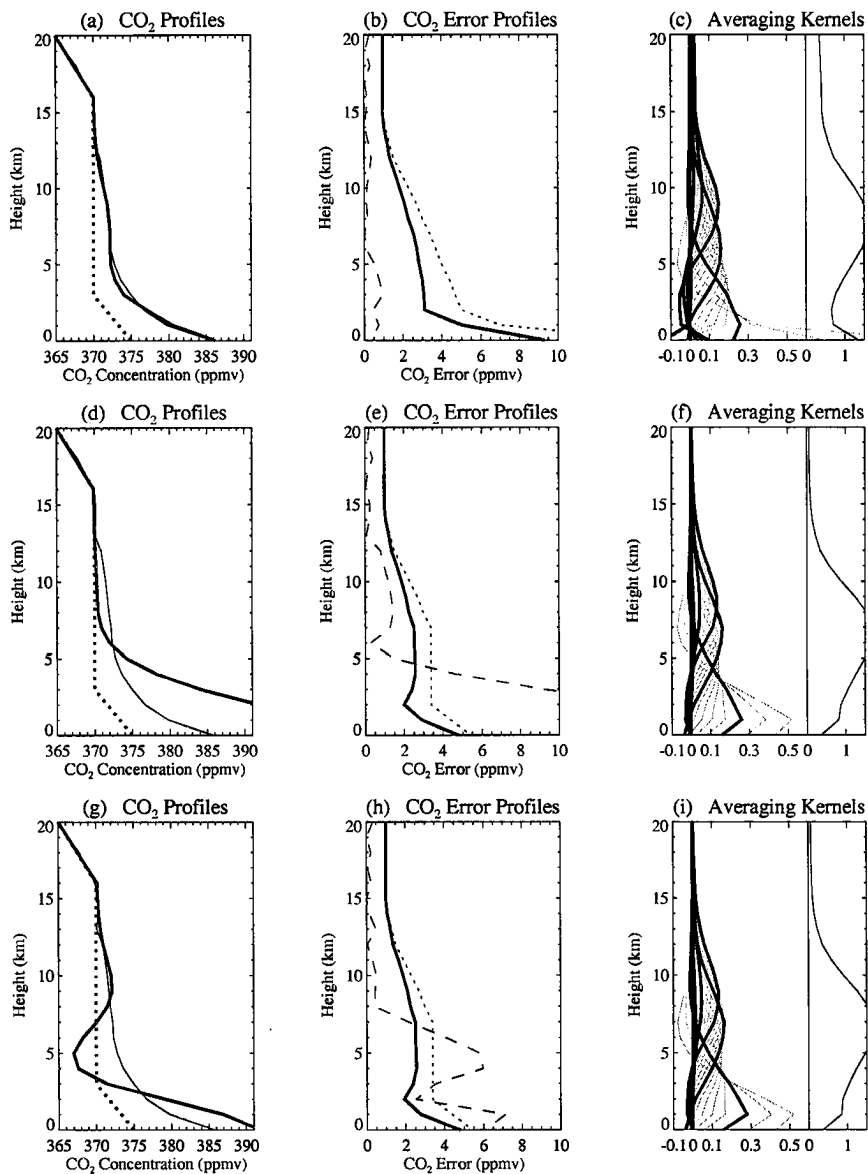


Figure 7.12: Same as Figure 7.11 except that $\alpha = 0.40$ and $\theta_{\odot} = 0^{\circ}$. The χ^2 values were 2755 (upper set), 2748 (middle set), and 2753 (lower set).

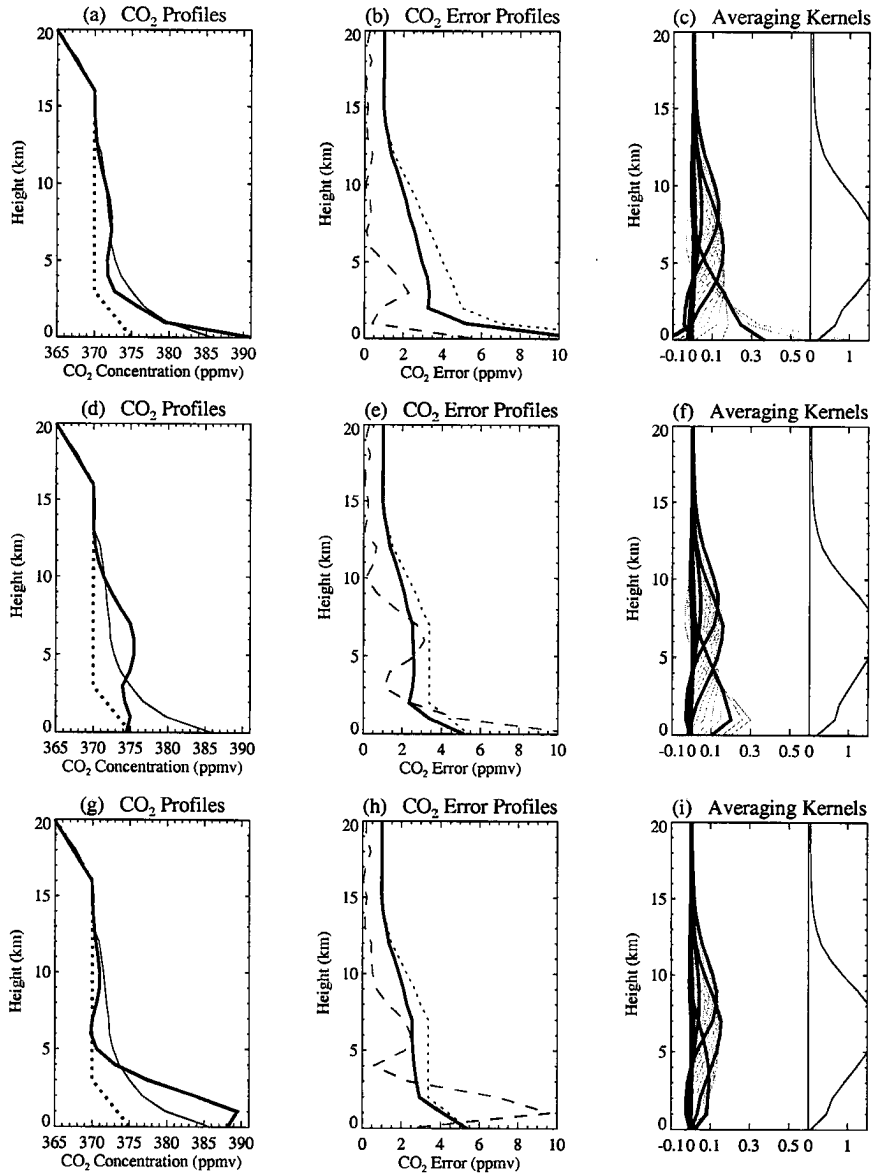


Figure 7.13: Same as Figure 7.11 except that $\alpha = 0.06$ and $\theta_{\odot} = 30^{\circ}$. The χ^2 values were 2754 (upper set), 2753 (middle set), and 2761 (lower set).

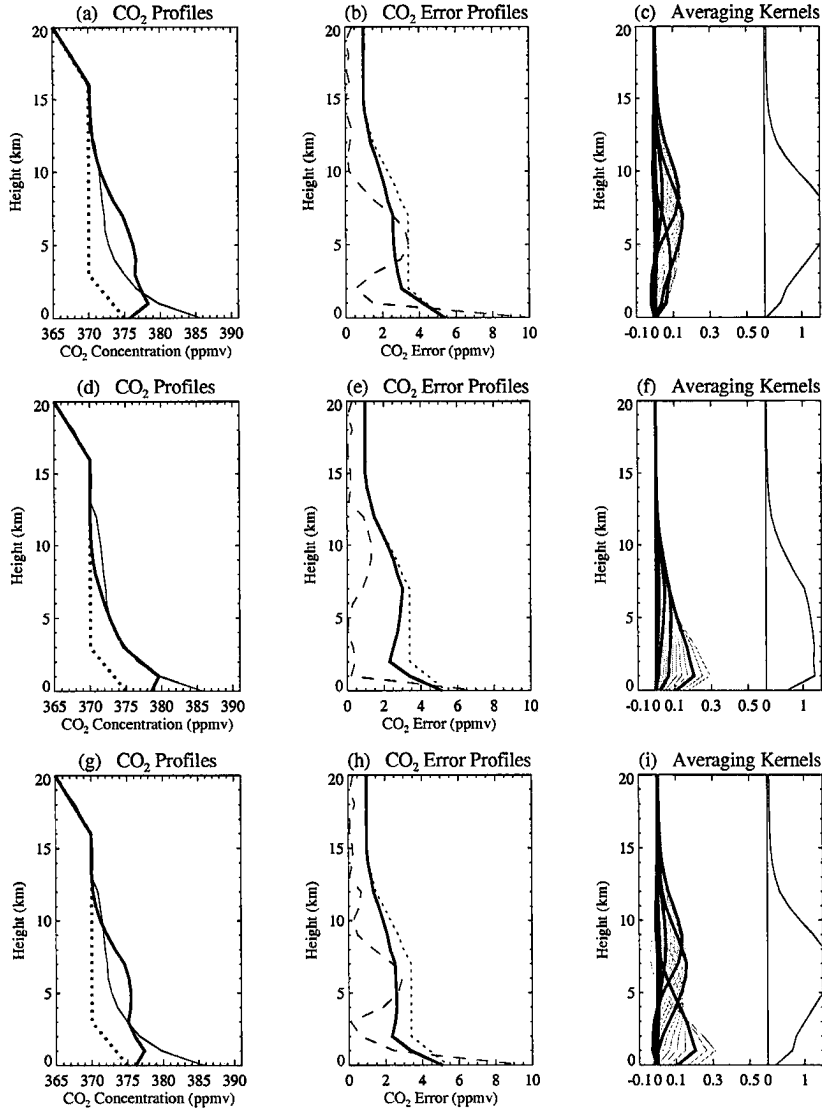


Figure 7.14: Retrieved source profile of CO₂ for CASE 2 with associated profiles of error statistics for measurements with $\alpha = 0.06$ and $\theta_{\odot} = 0^{\circ}$. (a,d,g) Real (thin solid), retrieved (thick solid), and *a priori* (dashed) CO₂ profiles; (b,e,h) estimated error (thick solid line), *a priori* error (dotted), and actual error (dashed); (c,f,i) Averaging kernels for retrieval (see text). The upper set resulted from using ONLY IR measurements, the middle set from using ONLY NIR measurements, and lower set from using BOTH IR and NIR measurements. The χ^2 values were 2036 (IR), 763 (NIR), and 2744 (BOTH).

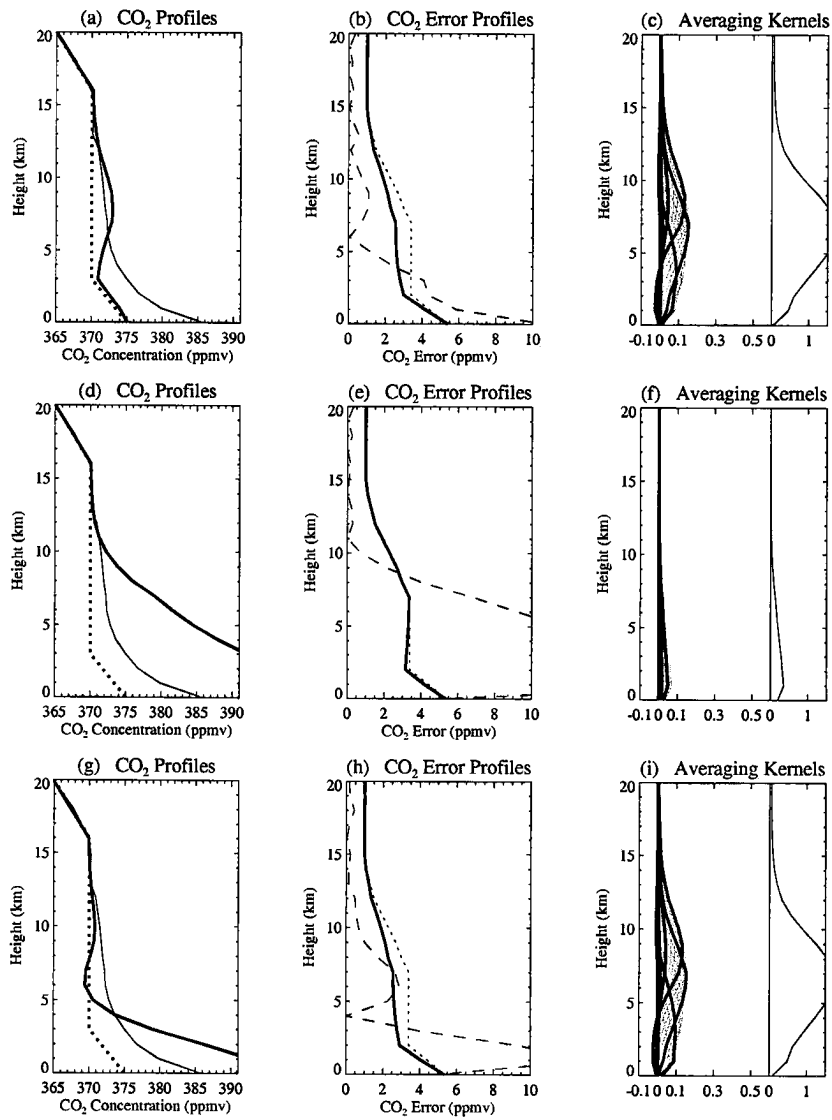


Figure 7.15: Same as Fig 7.14 except for CASE 3. The χ^2 values were 2038 (IR), 755 (NIR), and 2756 (BOTH).

Chapter 8

Conclusions and Future Work

The above study has demonstrated that the potential exists for measurements in the near infrared portion of the spectrum to be of benefit to retrieving profiles of CO₂ in the lower atmosphere, particularly when used in tandem with measurements from the far infrared. It was shown that the near and far infrared work in a complementary fashion in retrieving a profile of CO₂ in the lower atmosphere: the far infrared able to detect CO₂ in the mid troposphere and the near infrared closer to the surface.

Results indicate a precision in the CO₂ column-averaged values of better than 1 ppmv for the clear sky cases run. Results also indicate a precision in column-averaged value of better than 2.5 ppmv for the majority of cases ($\approx 73\%$) with a layer of thin cloud or aerosol present ($\tau < 0.2$) for an initial retrieval over a given locale provided there exists a means of detecting the height of a scattering layer to 1 km and the optical depth of the scattering layer to 10%. However, there is good reason to anticipate even better results once a number of retrievals are performed and the *a priori* tuned to a given locale using the results of previous retrievals.

Based on current research, it is estimated that the errors in resulting monthly-averaged column-average values of CO₂ from any such retrievals need to be less than 2.5 ppmv to be useful to researchers attempting to determine the location and magnitude of CO₂ surface sources and sinks. If space-based measurements are to be useful

in estimating CO₂ over broad regions not covered by thicker clouds, it appears that measurements in addition to those used from the near and far infrared in this work will be needed to mitigate the effects of scatter by optically thin cirrus and aerosol and other sources of potential retrieval bias. Given the uncertainty in the role that CO₂ plays in the earth's radiation budget and any warming in global climate that could result from its increase, the gravity of these issues warrant that further precise investigation into this potential is needed to assess the viability of space-based measurements to retrieve profiles of CO₂ in the lower atmosphere.

To obtain an improved quantitative assessment of this potential, more accurate parameterization in a number of areas is required. As this study was done somewhat "in a vacuum" with regard to the ability of current technology and methods to detect thin scatters, an assessment of these is required to determine if one or more possess the necessary capability to detect scatterers to the precision required to retrieving profiles of CO₂ or if new technologies and methods will have to be brought to bear on this problem of detecting CO₂ concentrations from space. Among the options to be explored are limb profiling of solar radiation (as done in the Stratospheric Aerosol and Gas Experiment (SAGE) missions), CO₂ slicing (as done using the High-Resolution Infrared Radiation Sounder (HIRS)), and absorption of reflected solar radiation by oxygen using the proposed Profiling A-Band Spectrometer/Visible Imager (PABSI). If these or other technologies show the potential of being useful in solving this problem, then a limit should be established as to how much scatter a CO₂ retrieval can tolerate and still return a desired level of accuracy in light of these available technologies. In relation to this endeavor, some further experimenting should be done to ascertain what combination of additional measurements would be most beneficial to retrieving CO₂ profiles from space.

On improving the realism of the retrieval, the spectral dependence of IR optical depth given a cloud or aerosol of particular optical depth in the NIR should be determined through the use of Mie calculations. Even though small, any effects of

scattering in the IR portion of the spectrum should also be included. As one will recall, the cirrus and aerosol retrieval cases performed here assumed them to be totally absorbing in this region of the spectrum.

Also, as noted earlier, the measurements done in the NIR were performed assigning a δ -function response to the instrument at each measuring wavenumber. Measurements in the NIR at state-of-the-art resolutions should be employed to more realistically simulate the contribution of the NIR measurements to retrieving CO₂ in the lower atmosphere.

Furthermore, there should be more investigation into the form of the *a priori* covariance matrix S_a to insure the correlations used are as accurate as possible. Data from sources such as balloon, aircraft, and surface should be used to establish a more empirically-derived S_a matrix. A reasonable but crude form was used in this study. In this light, a more accurate *a priori* CO₂ profile along with accompanying uncertainties might be obtained from such instruments as the scanning imaging absorption spectrometer for atmospheric cartography (SCIAMACHY). It is a part of the instrument package on the European Space Agency's Envisat 1 satellite.

Besides these, additional sensitivity studies should be undertaken to determine to what effect uncertainties in other input parameters besides scattering optical depth and altitude have on the uncertainty in the column-averaged value of the retrieved CO₂ profile. Among these are uncertainties in temperature, water vapor, surface albedo, solar zenith angle, and the optical properties of an atmospheric scatterer.

For the sake of efficiency, the information content of the measurements in the IR and NIR should also be performed similar to that done by Rodgers (1998) for the IR region covered by the Atmospheric Infrared Sounder (AIRS). By doing this, one will get a sense of how much a given number of measurements in the IR and NIR are contributing to retrieving concentrations of CO₂ at different levels in the atmosphere and how much added measurements are essentially suppressing noise.

There are also plans to do some further work on the radiative transfer model

used to simulate the measurements in the NIR (Radiant). A scheme allowing the addition of user-selected viewing angles (in addition to the current Gaussian angles) is planned. The addition of infrared sources is also planned so that Radiant can simulate the behavior of emission and scattering throughout both the solar and thermal infrared portions of the spectrum. This will make the model more flexible and easier to use by the atmospheric science community at large who may find some of its strengths attractive for particular applications.

Lastly, one of the primary goals of this effort is to consistently obtain CO₂ monthly column-averaged values that are precise enough for use by those trying to accurately determine the sources and sinks of CO₂ at the earth's surface. A logical next step therefore would be to work closely with those involved in this effort to assist in bringing closure to the carbon cycle problem.

Bibliography

- Bakwin, P., P. Tans, D. Hurst, and C. Zhao: 1998, Measurements of carbon dioxide on very tall towers: Results of the NOAA/CMDL program. *Tell. Ser. B*, **50**, 401–415.
- Bakwin, P., C. Zhao, W. U. III, P. Tans, and E. Quesnell.: 1995, Measurements of carbon dioxide on a very tall tower. *Tell. Ser. B*, **47**, 535–549.
- Benedetti, A., P. Gabriel, and G. Stephens: 2002, Properties of reflected sunlight derived from a Green's function method. *J. Quant. Spectrosc. Radiat. Transfer*, **72**, 201–225.
- Bischof, W.: 1971, Carbon dioxide concentration in the upper troposphere and lower stratosphere II. *Tellus*, **23**, 558–561.
- Bischof, W., R. Borchers, P. Fabian, and B. Krüger: 1985, Increased concentration and vertical distribution of carbon dioxide in the stratosphere. *Nature*, **316**, 708–710.
- Bode, H.: 1945, *Network Analysis and Feedback Amplifier Design*. Van Nostrand, Princeton, New Jersey.
- Bukata, R., J. Jerome, K. Kondratyev, and D. Pozdnyakov: 1995, *Optical Properties and Remote Sensing of Inland and Coastal Waters*. CRC Press, Boca Raton, Florida.
- Burkett, V. and J. Kusler: 2000, Climate change: Potential impacts and interactions in wetlands of the United States. *J. Am. Water Resour. Assoc.*, **36**, 313–320.
- Caldeira, K. and J. Kasting: 1993, Insensitivity of global warming potentials to carbon-dioxide emission scenarios. *Nature*, **366**, 251–253.
- Cess, R., M. Zhang, G. Potter, H. Barker, R. Colman, D. Dazlich, A. Delgenio, M. Esch, J. Fraser, V. Galin, W. Gates, J. Hack, W. Ingram, J. Kiehl, A. Lacis, H. Letreut, Z. Li, X. Liang, J. Mahfouf, B. McAvaney, V. Meleshko, J. Morcrette, D. Randall, E. Roeckner, J. Royer, A. Sokolov, P. Sporyshev, K. Taylor, W. Wang, and R. Wetherald: 1993, Uncertainties in carbon-dioxide radiative forcing in atmospheric general-circulation models. *Science*, **262**, 1252–1255.

- Cox, P., R. Betts, C. Jones, S. Spall, and I. Totterdell: 2000, Acceleration of global warming due to carbon-cycle feedbacks in a coupled climate model. *Nature*, **408**, 184–187.
- Dettinger, M. and M. Ghil: 1998, Seasonal and interannual variations of atmospheric CO₂ and climate. *Tell. Ser. B*, **50**, 1–24.
- Elachi, C.: 1987, *Introduction to the Physics and Techniques of Remote Sensing*. John Wiley and Sons, New York, New York.
- Engelen, R., A. Denning, K. Gurney, and G. Stephens: 2001, Global observations of the carbon budget: I. Expected satellite capabilities for emission spectroscopy in the EOS and NPOESS eras. *J. Geophys. Res.*, **106**, 20055–20068.
- Engelen, R. and G. Stephens: 1997, Infrared radiative transfer in the 9.6- μ m band: Application to TIROS operational vertical sounder ozone retrieval. *J. Geophys. Res.*, **102**, 6929–6939.
- 1999, Characterization of water-vapour retrievals from TOVS/HIRS and SSM/T-2 measurements. *Quart. J. Roy. Meteorol.*, **125**, 331–351.
- Feddema, J.: 1999, Future African water resources: Interactions between soil degradation and global warming. *Clim. Change*, **42**, 561–596.
- Fowler, A. and K. Hennessy: 1995, Potential impacts of global warming on the frequency and magnitude of heavy precipitation. *Nat. Hazards*, **11**, 283–303.
- Gabriel, P., S. Lovejoy, A. Davis, D. Schertzer, and G. Austin: 1990, Discrete angle radiative transfer 2. Renormalization approach for homogeneous and fractal clouds. *J. Geophys. Res.*, **95**, 11717–11728.
- Greenwald, T. and G. Stephens: 1988, Application of a doubling-adding radiation model to visibility problems. Technical report, Cooperative Institute for Research in the Atmosphere.
- Gurney, K., R. Law, A. Denning, P. Rayner, D. Baker, P. Bousquet, L. Bruhwiler, Y. Chen, P. Ciais, S. Fan, I. Fung, M. Gloor, M. Heimann, K. Higuchi, J. John, T. Maki, S. Maksyutov, K. Masarie, P. Peylin, M. Prather, B. Pak, J. Randerson, J. Sarmiento, S. Taguchi, T. Takahashi, and C. Yuen: 2002, Towards robust regional estimates of CO₂ sources and sinks using atmospheric transport models. *Nature*, **415**, 626–630.
- Howden, S., G. McKeon, H. Meinke, M. Entel, and N. Flood: 2001, Impacts of climate change and climate variability on the competitiveness of wheat and beef cattle production. *Environ. Int.*, **27**, 155–160.
- Keeling, C. and T. Whorf: 2001, Atmospheric CO₂ records from sites in the SIO air sampling network. *Trends: A Compendium of Data on Global Change*, Carbon Dioxide Information Analysis Center, Oak Ridge National Laboratory, U.S. Department of Energy, Oak Ridge, Tenn U.S.A.

- Kirschbaum, M.: 2000, Forest growth and species distribution in a changing climate. *Tree Physiol.*, **20**, 309–322.
- Kuang, Z., J. Margolis, G. Toon, D. Crisp, and Y. Yung: 2002, Spaceborne measurements of atmospheric CO₂ by high-resolution NIR spectrometry of reflected sunlight: An introductory study. *To Appear in Geophys. Res. Lett.*
- Lacis, A. and V. Oinas: 1991, A description of the correlated *k* distribution method for modeling nongray gaseous absorption, thermal emission, and multiple scattering in vertically inhomogeneous atmospheres. *J. Geophys. Res.*, **96**, 9027–9063.
- Lambert, G., P. Monfray, B. Ardouin, G. Bonsang, A. Gaudry, V. Kazan, and P. Polian: 1995, Year-to-year changes in atmospheric CO₂. *Tell. Ser. B*, **47**, 53–55.
- Liou, K.: 1992, *Radiation and Cloud Processes in the Atmosphere*. Oxford University Press, New York, New York.
- Lynch, D., K. Sassen, D. Starr, and G. Stephens, eds.: 2002, *Cirrus*. Oxford University Press, New York, New York.
- Manabe, S.: 1998, Study of global warming by GFDL climate models. *Ambio*, **27**, 182–186.
- Marggraf, W. and M. Griggs: 1969, Aircraft measurements and calculations of the total downward flux of solar radiation as a function of altitude. *J. Atmos. Sci.*, **26**, 469–477.
- Matveev, V.: 1972, Approximate representation of absorption coefficient and equivalent widths of lines with Voigt profile. *J. Appl. Spectrosc*, **16**, 228–233.
- Meehl, G., W. Collins, B. Boville, J. Kiehl, T. Wigley, and J. Arblaster: 2000, Response of the NCAR climate system model to increased CO₂ and the role of physical processes. *J. Clim.*, **13**, 1879–1898.
- Miller, S., G. Stephens, C. Drummond, A. Heidinger, and P. Partain: 2000, A multi-sensor diagnostic satellite cloud property retrieval scheme. *J. Geophys. Res.*, **105**, 19955–19971.
- O'Brien, D. and P. Rayner: 2002, Global observations of the carbon budget: II. CO₂ column from differential absorption of reflected sunlight in the 1.61 μ m band of CO₂. *To Appear in J. Geophys. Res.*
- Paltridge, G. and C. Platt: 1976, *Radiative Processes in Meteorology and Climatology*. Elsevier Scientific Publishing, Amsterdam, The Netherlands.
- Papadopol, C.: 2000, Impacts of climate warming on forests in Ontario: Options for adaptation and mitigation. *Forest. Chron.*, **76**, 139–149.
- Park, J.: 1997, Atmospheric CO₂ monitoring from space. *Appl. Opt.*, **36**, 2701–2712.

- Rayner, P. and D. O'Brien: 2001, The utility of remotely sensed CO₂ concentration data in surface source inversions. *Geophys. Res. Lett.*, **28**, 175–178.
- Rinsland, C., M. Gunson, R. Zander, and M. López-Puertas: 1992, Middle and upper atmosphere pressure-temperature profiles and the abundances of CO₂ and CO in the upper atmosphere from ATMOS/Spacelab 3 observations. *J. Geophys. Res.*, **97**, 20479–20495.
- Rodgers, C.: 1998, Information content and optimisation of high spectral resolution remote measurements. *Adv. Space Res.*, **21**, 361–367.
- 2000, *Inverse Methods for Atmospheric Sounding: Theory and Practice*. World Scientific Publishing, River Edge, New Jersey.
- Schmidt, U. and A. Khedim: 1991, In situ measurements of carbon dioxide in the winter arctic vortex and at midlatitudes: An indicator of the 'age' of the stratosphere. *Geophys. Res. Lett.*, **18**, 763–766.
- Sorenson, L., R. Goldberg, T. Root, and M. Anderson: 1998, Potential effects of global warming on waterfowl populations breeding in the Northern Great Plains. *Clim. Change*, **40**, 343–369.
- Stamnes, K. and P. Conklin: 1984, A new multi-layer discrete ordinate approach to radiative transfer in vertically inhomogeneous atmospheres. *J. Quant. Spectrosc. Radiat. Transfer*, **31**, 273–282.
- Stamnes, K. and R. Swanson: 1981, A new look at the discrete ordinate method for radiative transfer calculations in anisotropically scattering atmospheres. *J. Atmos. Sci.*, **38**, 387–399.
- Stamnes, K., S. Tsay, and T. Nakajima: 1988, Computation of eigenvalues and eigenvectors for the discrete ordinate and matrix operator methods in radiative transfer. *J. Quant. Spectrosc. Radiat. Transfer*, **39**, 415–419.
- Tanaka, M., T. Nakazawa, and S. Aoki: 1987, Seasonal and meridional variations of atmospheric carbon dioxide in the lower troposphere of the northern and southern hemispheres. *Tell. Ser. B*, **39**, 29–41.
- Thorpe, R., J. Gregory, T. Johns, R. Wood, and J. Mitchell: 2001, Mechanisms determining the Atlantic thermohaline circulation response to greenhouse gas forcing. *J. Clim.*, **14**, 3102–3116.
- Timbal, B., J. Mahfouf, J. Royer, and D. Cariolle: 1995, Sensitivity to prescribed changes in sea-surface temperature and sea-ice in doubled carbon-dioxide experiments. *Clim. Dyn.*, **12**, 1–20.
- Titus, J. and C. Richman: 2001, Maps of lands vulnerable to sea level rise: Modeled elevations along the U.S. Atlantic and Gulf coasts. *Clim. Res.*, **18**, 205–228.

- Topp, C. and C. Doyle: 1996, Simulating the impact of global warming on milk and forage production in Scotland. 1. The effects on dry-matter yield of grass and grass white clover swards. *Agr. Syst.*, **52**, 213–242.
- VandeHulst, H.: 1980, *Multiple Light Scattering: Tables, Formulas, and Applications, Vol. I and II*. Academic Press, New York, New York.
- Wuebbles, D., A. Jain, K. Patten, and K. Grant: 1995, Sensitivity of direct global warming potentials to key uncertainties. *Clim. Change*, **29**, 265–297.

Appendix A

Radiant

A.1 Introduction

There are quite a few radiative transfer (RT) codes currently available to the atmospheric science community. A list of some of the RT codes in current use can be found in the Table A.1. Although the amount of code out there is not scarce, as one carefully observes from the table, the heart of most of these codes is based on one of two methods: the eigenmatrix method as implemented by the Discrete Ordinate Method of Radiative Transfer (DISORT) or the doubling/adding method. The purpose of this section is to describe a new plane-parallel RT code that takes advantage of the benefits of these two methods while leaving some of their more undesirable characteristics behind. Before beginning however, it should be noted that not all of the RT codes listed in Table A.1 are plane-parallel oriented as the code described next.

A.1.1 Doubling/Adding and DISORT

The idea of the doubling/adding method is to build up layers of atmosphere of relatively large optical depth, each with given optical properties, via taking slices of atmosphere of minute optical depth. This is done by a process of doubling the orig-

Table A.1: Sample of organizations or authors and some of their radiative transfer codes (Source: the World Wide Web; * = Not available)

Organization or Authors	Name of Code	RT Core
Air Force Research Lab	MODTRAN4	DISORT
Air Force Research Lab	MOSART	DISORT
Arve Kylling and Bernhard Mayer	LibRadTran	DISORT
Boston University	Streamer	DISORT
Brookhaven National Lab	*	doubling/adding
Environmental Systems Science Centre	DOORS	Similar to DISORT
Institut Für Meereskunde Kiel	MC-Layer	Monte Carlo
NASA - Ames	*	doubling/adding
NCAR	TUV	DOM
NOAA - GFDL	*	doubling/adding
Royal Netherlands Meteorological Inst.	DAK	doubling/adding
U. of Alaska Fairbanks	UVSPEC	DISORT
U. of Cal., San Diego	FEMRAD	FEM
U. of Cal., Santa Barbara	SBDART	DISORT
U. of Colorado	PolRadTran	DISORT
U. of Colorado	SHDOM	SHDOM
U. of Maryland	*	doubling/adding
U. of Texas, Arlington	*	doubling/adding
Universitetet I Oslo	RADTRAN	DISORT
U.S. Army Developmental Test Command	BLIRB	DOM

inal optical depth iteratively until the desired optical depth of the layer is attained. The resulting individual, homogeneous layers of atmosphere so constructed are then added together to yield the overall optical properties of the atmosphere. On the other hand, the eigenmatrix method as implemented by DISORT makes use of eigenmatrices to solve a system of differential equations to obtain a solution to the radiative transfer equation (4.1).

Both methods have their strengths and weaknesses. A primary strength of the doubling/adding method is that, once a given layer of atmosphere has been constructed, it does not need to be recomputed if the optical properties in the given layer do not change. Upon calculating any other layers in the medium whose optical properties do change, the layers can then again be added together to obtain the RT solution. However, some of this computational efficiency can be eroded if some layers

that need recomputing are optically thick.

In contrast, the time it takes to obtain the RT solution via the eigenmatrix approach as implemented by DISORT takes the same amount of time irrespective of the optical depths of the individual layers. However, when one wishes to account for changes that take place in the atmosphere, the entire system of differential equations needs to be re-solved to obtain the new solution.

As will now be demonstrated, another way of obtaining the solution to the equation of transfer that can take advantage of the strengths of both of these methods is introduced while leaving some of their more undesirable characteristics behind. We turn our attention now to this alternative method as employed in a new radiative transfer code introduced here as Radiant.

A.1.2 Radiant: An Efficient Approach to Computing

Radiative Transfer

As mentioned above, it would be highly desirable to use a method that was not sensitive to optical depth (as the doubling/adding method) and at the same time would not demand the recomputation of the entire solution if the optical properties in just one portion of the medium change (as done by DISORT). The idea is to take the optical depth insensitivity of the eigenmatrix approach and combine it with the "individual layeredness" of the doubling/adding method. By using the eigenmatrix method to compute the individual layers and then using adding to combine them, what results is an often faster yet accurate hybrid. These ideas have been joined in a new radiative transfer code called Radiant.

This model is used to describe the influence of nature on wavelengths of light in the NIR portion of the spectrum and produce the resulting simulated NIR measurements. Radiant is a multi-stream, plane-parallel RT code that accounts for multiple scattering in the atmosphere and has two computational modes for performing radiative transfer. The primary mode uses the ideas as described above: build individual

(homogeneous) layers of atmosphere using the eigenmatrix method and then combine the layers using adding. This will be referred to as the modified eigenmatrix method (MEM). The other mode uses a truncated series approach for building very optically thin layers (those with $\tau < 0.003$). This will be referred to as the truncated series method (TSM). The rationale for the second mode is to assist Radiant in obtaining the fastest possible solutions for even these very small optical depths. This is needed because the eigenmatrix approach, being insensitive to optical depth, always takes the same amount of time to compute a given layer. For the vast majority of media, the eigenmatrix method will be faster than doubling; however, for $\tau < 0.003$, the doubling method is faster (see section A.5 for timing results). This ensures faster layer-building regardless of the optical depth.

By using the interaction principle (see chapter 4), the solution to the radiative transfer equation can be expressed in terms of global transmission and reflection matrices and two source vectors. Here, the overall solution is rendered

$$I^+(H) = T(0, H)I^+(0) + R(H, 0)I^-(H) - T(0, H)S_1^+ - R(H, 0)S_2^- + S_2^+ \quad (\text{A.1})$$

$$I^-(0) = R(0, H)I^+(0) + T(H, 0)I^-(H) - R(0, H)S_1^+ - T(H, 0)S_2^- + S_1^- \quad (\text{A.2})$$

where $I^+(H)$ is the upwelling radiation at the top of the atmosphere, $I^-(0)$ is the downwelling radiation at the surface, T and R are the global transmission and reflection matrices for the atmospheric state, and S_1^\pm and S_2^\pm are the accompanying source vectors. Some details concerning the global transmission and reflection matrices along with some numerical discussion is given in appendix B.

No matter which method is used, MEM or TSM, the T and R matrices and source vectors are computed for each layer of atmosphere. Once these have been computed for a given layer, they are combined with those of other layers to build up the atmosphere for its current state. For layers whose optical properties do not change, they can be saved for subsequent use and again easily combined with those

of other layers whose optical properties do change to quickly obtain the radiances for a later atmospheric state.

A.2 Modified Eigenmatrix Method

The eigenmatrix method, as implemented in Radiant, can be used to derive the T and R matrices for layers of any optical depth experienced in the real atmosphere. Again, this process will be referred to as the modified eigenmatrix method (MEM).

Although theoretically straight forward, the solution of the radiative transfer equation (4.10) is fraught with numerical difficulty as the instability of computing the exponential matrix is well known. Using eigenvalues and eigenvectors, the exponential matrix can be expressed as

$$e^{A\tau} = X e^{\Lambda\tau} X^{-1} \quad (\text{A.3})$$

where $e^{\Lambda\tau}$ is a diagonal matrix with the exponentials of the eigenvalues of A on the diagonal, X is the matrix of associated eigenvectors and X^{-1} its inverse. To solve for the eigenvalues of A , polynomial deflation can be used to reduce the computational time as well as improve numerical stability (Stamnes and Swanson (1981); Stamnes et al. (1988)). However, the exponentials of the positive eigenvalues in $e^{\Lambda\tau}$ can produce numerical problems when the optical depth $|\tau| = \sigma_e \Delta z$ becomes large; however, Stamnes and Conklin (1984) showed that this problem can be largely overcome by using a scaling transformation. Using a similar transformation, the T and R matrices take the form (Benedetti et al., 2002)

$$T(H, 0) = -u_+ [I - (u_+^{-1} u_-)^2] [(u_+^{-1} u_-)^{-1} e^{-\Lambda^+ \tau(H)}] \\ \{I - [(u_+^{-1} u_-)^{-1} e^{-\Lambda^+ \tau(H)}]^2\}^{-1} u_-^{-1} \quad (\text{A.4})$$

$$\begin{aligned}
R(H, 0) &= -u_+[I - (u_+^{-1}u_-)e^{-\Lambda^+\tau(H)}(u_+^{-1}u_-)^{-1}e^{-\Lambda^+\tau(H)} \\
&\quad \{I - [(u_+^{-1}u_-)^{-1}e^{-\Lambda^+\tau(H)}]^2\}^{-1}u_-^{-1}
\end{aligned} \tag{A.5}$$

where u_+ and u_- are matrices, when appropriately assembled, composing the matrix X , Λ^+ is a diagonal matrix containing the positive eigenvalues of the matrix A , $\tau(H)$ is the optical depth at a given altitude H , and I is the identity matrix. The source vectors S_1^\pm and S_2^\pm can be given as

$$S_1^\pm = \left(\frac{I}{\mu_\odot} - A\right)^{-1} \frac{\omega_o}{4\pi} F_\odot M P_\odot^\mp e^{-\frac{\tau}{\mu_\odot}} \tag{A.6}$$

$$S_2^\pm = \left(\frac{I}{\mu_\odot} - A\right)^{-1} \frac{\omega_o}{4\pi} F_\odot M P_\odot^\mp \tag{A.7}$$

where μ_\odot , A , F_\odot , M , and P_\odot^\mp are the same as in section 4.2, ω_o is the single scatter albedo, and I is again the identity matrix. Note that the expressions for T and R now only contain decaying exponentials.

Upon careful inspection of the expressions for T and R , one observes that some further numerical savings can be achieved by employing some substitutions, rearranging, and simplifying. A discussion of this and the resulting expressions for global T and R are given in appendix B.

A.3 Truncated Series Method

The truncated series method, as implemented in Radiant, can be used to derive T and R matrices for layers whose optical depths are less than $\tau = 0.08$. Again, this process is denoted as the TRM. Its benefits and limitations were explored as a project by graduate student Brian McNoldy in a PhD-level course in radiative transfer at the CSU Department of Atmospheric Science. The method allows the computation of T

and R matrices using n^2 operations rather than alot of the n^3 operations required by the MEM.

The basic concept behind TRM is to do a series expansion of the exponential matrix and truncate it at an appropriate number of terms for a given accuracy. We start with

$$\begin{aligned}
e^{A\tau} &= e^{\begin{bmatrix} t & -r \\ r & -t \end{bmatrix} \tau} \\
&= \begin{bmatrix} 1 & 0 \\ 0 & 1 \end{bmatrix} + \begin{bmatrix} t & -r \\ r & -t \end{bmatrix} \tau + \begin{bmatrix} t & -r \\ r & -t \end{bmatrix}^2 \frac{\tau^2}{2!} \\
&\quad + \begin{bmatrix} t & -r \\ r & -t \end{bmatrix}^3 \frac{\tau^3}{3!} + \begin{bmatrix} t & -r \\ r & -t \end{bmatrix}^4 \frac{\tau^4}{4!} + \dots
\end{aligned} \tag{A.8}$$

In order to experience the numerical savings desired while retaining a reasonable degree of accuracy, the number of terms retained in the series is set so three significant digits are retained for the radiances calculated. Depending on the optical depth of the layer under construction, as many as six or as few as three terms are used. For example, for optical depths in the range $0.004 \leq \tau \leq 0.02$, four terms are retained in the series. The formulations for the T and R matrices that result for the four-term case are

$$\begin{aligned}
T(H, 0) &= 1 - t\tau + (t^2 - r^2) \frac{\tau^2}{2!} - (t^3 + 2(r^2t + tr^2) + rtr) \frac{\tau^3}{3!} \\
&\quad + (t(6t^3 + 5r^2t + 10tr^2 + 3rtr) \\
&\quad - r(2r^3 - t^2r + 2rt^2 - 3trt)) \frac{\tau^4}{4!}
\end{aligned} \tag{A.9}$$

$$\begin{aligned}
R(H, 0) = & r\tau - (rt + tr)\frac{\tau^2}{2!} + (t(2rt + tr) - r(4r^2 - t^2))\frac{\tau^3}{3!} \\
& - (t(5r^3 + t^2r + 3rt^2 + 3trt)) \\
& + r(t^3 - 7r^2t + 3tr^2 + 15rtr)\frac{\tau^4}{4!}
\end{aligned} \tag{A.10}$$

where t and r are the local transmission and reflection matrices and τ is the optical depth of the layer. Since the matrix A is composed of these t and r matrices (recall eqs. (4.4) and (4.9)), numerical savings are realized here due to the fact that if A is $2n \times 2n$ for example, then t and r are only $n \times n$; thus, even though there are more matrix multiplications required to compute T and R in the TRM as opposed to the MEM, the size of the matrices being multiplied actually causes the computation of T and R to be less numerically expensive.

A.4 Radiant, DISORT, and doubling/adding: Accuracy Comparisons

To test the trueness of Radiant's algorithms, calculations of radiant intensity were performed for a layer with different values of τ , ω_o , g , and μ_\odot and compared with the radiance tables from VandeHulst (1980) as well as the values generated by two doubling/adding schemes and DISORT for the same optical parameters. Tables A.2 and A.3 show the results of a comparison between Van de Hulst Table 35, the doubling/adding scheme used in Gabriel et al. (1990), DISORT, and Radiant using the Henyey-Greenstein phase function. Both DISORT and Radiant were run in a 16-stream mode (8 upward and 8 downward radiances) during these tests. Table A.4 reveals the results of a comparison with the doubling/adding scheme used in Miller et al. (2000) and also used for comparison by Benedetti et al. (2002) for the same optical parameters and values of degree m for the Henyey-Greenstein phase function.

Table A.2: Comparison of upwelling radiances generated by Van de Hulst Table 35 (VDH), a doubling/adding scheme (D/A), and DISORT (D) with those generated by Radiant (R) for a given layer of different optical parameters.

τ	ω_o	g	μ	μ_{\odot}	VDH $I^+(H)$	D/A $I^+(H)$	D $I^+(H)$	R $I^+(H)$
1	1	0.75	1	0.1	1.5137E-01	1.5172E-01	1.5836E-01	1.4854E-01
1	1	0.75	1	0.5	1.0120E-01	1.0146E-01	1.0771E-01	1.0020E-01
1	1	0.75	1	1.0	0.3909E-01	0.3925E-01	0.2019E-01	0.3796E-01
2	1	0.75	1	0.1	2.0571E-01	2.0618E-01	2.1269E-01	2.0216E-01
2	1	0.75	1	0.5	2.0119E-01	2.0163E-01	2.0798E-01	1.9991E-01
2	1	0.75	1	1.0	1.0438E-01	1.0476E-01	8.3351E-02	1.0277E-01
4	1	0.75	1	0.1	2.8433E-01	2.8485E-01	2.9130E-01	2.7987E-01
4	1	0.75	1	0.5	3.4710E-01	3.4764E-01	3.5391E-01	3.4561E-01
4	1	0.75	1	1.0	2.5658E-01	2.5712E-01	2.3530E-01	2.5465E-01
8	1	0.75	1	0.1	3.7997E-01	3.8042E-01	3.8693E-01	3.7446E-01
8	1	0.75	1	0.5	5.1971E-01	5.2013E-01	5.2651E-01	5.1808E-01
8	1	0.75	1	1.0	4.9270E-01	4.9300E-01	4.7138E-01	4.9086E-01

Table A.3: Comparison of downwelling radiances generated by Van de Hulst Table 35 (VDH), a doubling/adding scheme (D/A), and DISORT (D) with those generated by Radiant (R) for a given layer of different optical parameters.

τ	ω_o	g	μ	μ_{\odot}	VDH $I^-(0)$	D/A $I^-(0)$	D $I^-(0)$	R $I^-(0)$
1	1	0.75	1	0.1	2.1380E-01	2.1468E-01	2.1075E-01	2.1068E-01
1	1	0.75	1	0.5	2.6663E-01	2.6805E-01	2.6647E-01	2.6562E-01
1	1	0.75	1	1.0	3.0652E+00	3.0862E+00	2.9096E+00	3.0689E+00
2	1	0.75	1	0.1	2.7614E-01	2.7670E-01	2.7513E-01	2.7259E-01
2	1	0.75	1	0.5	4.2244E-01	4.2370E-01	4.2255E-01	4.2142E-01
2	1	0.75	1	1.0	2.8247E+00	2.8205E+00	2.7008E+00	2.8345E+00
4	1	0.75	1	0.1	2.9606E-01	2.9608E-01	2.9594E-01	2.9267E-01
4	1	0.75	1	0.5	5.0828E-01	5.0852E-01	5.0835E-01	5.0765E-01
4	1	0.75	1	1.0	1.5155E+00	1.5014E+00	1.4762E+00	1.5234E-01
8	1	0.75	1	0.1	2.3639E-01	2.3619E-01	2.3636E-01	2.3386E-01
8	1	0.75	1	0.5	4.2235E-01	4.2206E-01	4.2235E-01	4.2214E-01
8	1	0.75	1	1.0	6.7002E-01	6.6744E-01	6.6797E-01	6.7166E-01

Table A.4: Comparison of radiances generated by a doubling/adding scheme (D/A) with those generated by Radiant (R). The optical parameters are: $\tau = 1$, $\omega = 1$, $g = 0.8$. Also, $\mu_{\odot} = \cos 30^{\circ}$.

μ	m	D/A $I^+(H)$	R $I^+(H)$	D/A $I^-(0)$	R $I^-(0)$
0.9894	0	9.9717E-03	9.9718E-03	1.6764E-01	1.6765E-01
0.7554	0	1.6232E-02	1.6232E-02	1.8942E-01	1.8942E-01
0.0950	0	4.8565E-02	4.8566E-02	6.9504E-02	6.9504E-02
0.9894	3	1.0576E-02	1.0576E-02	2.8254E-01	2.8254E-01
0.7554	3	2.1393E-02	2.1393E-02	6.9865E-01	6.9865E-01
0.0950	3	8.3972E-02	8.3973E-02	1.3309E-01	1.3309E-01
0.9894	7	1.0577E-02	1.0577E-02	2.8442E-01	2.8442E-01
0.7554	7	2.1415E-02	2.1416E-02	8.3781E-01	8.3781E-01
0.0950	7	8.4466E-02	8.4467E-02	1.3444E-01	1.3444E-01
0.9894	11	1.0577E-02	1.0577E-02	2.8441E-01	2.8442E-01
0.7554	11	2.1408E-02	2.1407E-02	8.5923E-01	8.5922E-01
0.0950	11	8.4532E-02	8.4533E-02	1.3445E-01	1.3449E-01
0.9894	15	1.0577E-02	1.0577E-02	2.8441E-01	2.8442E-01
0.7554	15	2.1406E-02	2.1405E-02	8.6311E-01	8.6310E-01
0.0950	15	8.4497E-02	8.4498E-02	1.3447E-01	1.3446E-01

A.5 Radiant, DISORT, and doubling/adding: Timing Comparisons

To test the speed of Radiant’s algorithms, two speed comparisons were performed. First, Radiant was tested against the doubling/adding code used in Greenwald and Stephens (1988) to compare the time it took to compute radiances for layers of different optical depth. This was done to get a sense of how fast the eigenmatrix method was against the doubling method for building a given layer. Here, Figure A.1 confirms that, as one expects, the doubling method takes longer to compute the global transmission, reflection, and source properties of the layer as the optical depth τ increases (note that the abscissa on the plot is $\log \tau$) whereas the eigenmatrix method, which is insensitive to optical depth, takes a fixed amount of time to compute the radiances. What is somewhat enlightening is the fact that the eigenmatrix method (at least when being run in a 16-stream mode as this was) is faster than the doubling method for the vast majority of optical depths experienced in the real atmosphere.

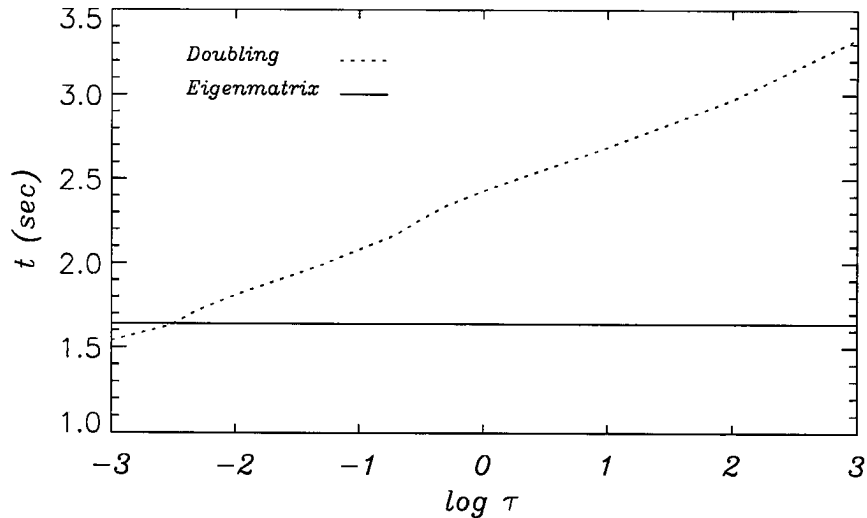


Figure A.1: Results of a speed comparison between the eigenmatrix method in Radiant and the doubling method. The total times are the result of computing the radiances for a given atmospheric scene 500 times on a computer with a 400 MHz microprocessor.

The crossover point is at $\approx \tau = 0.003$ with the eigenmatrix method being faster for every optical depth greater than this. For example, at $\tau = 10$ its about 66% faster. This increase in speed, while not outstanding, can potentially save much valuable time over the course of a long series of computations.

For the second test, Radiant was tested against DISORT to see, for a given atmospheric state built up from a fixed number of layers, what kind of time savings can be achieved by using Radiant as opposed to DISORT when only the optical properties in one layer of atmosphere change and the radiances are recomputed. This situation is faced in practice when, as in this work for the NIR radiances, Jacobians are needed to perform the retrieval and computing the elements of the Jacobian by finite difference is required.

Figure A.2 shows the results of these tests. The solid line denoted "Radiant (1)" is the time it took Radiant to compute the radiance for a new atmospheric scene for the number of layers indicated. The dash dot line denoted "DISORT" is the time it took DISORT to compute the radiance for the same scene and number of layers.

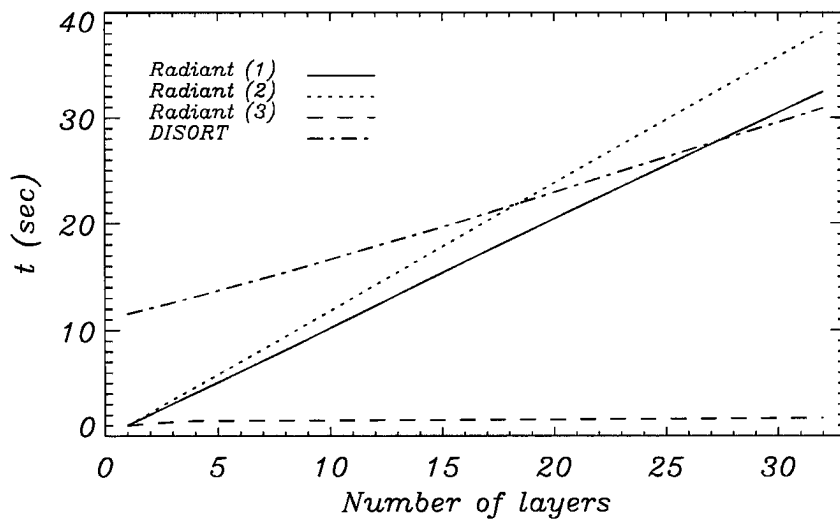


Figure A.2: Results of a speed comparison between Radiant and DISORT. The total times are the result of computing the radiances for a given atmospheric scene 500 times on a computer with a 550 MHz microprocessor. See text for details between Radiant (1), (2), and (3).

The two dashed lines denoted "Radiant (2)" and "Radiant (3)" are the times it took Radiant to perform Jacobian-related calculations. Specifically, "Radiant (2)" is the same as "Radiant (1)" except that some additional layer computations and saving were performed to prepare for following calls to Radiant when it would be tasked to compute the radiance for new atmospheric scenes where only the optical properties of one layer would change. Again, this was done in practice when the computation of Jacobian elements by finite difference was required. The extra time spent up front here can yield big dividends as the dashed line denoted "Radiant (3)" reveals. When subsequent calls to Radiant are made in this scenario, aside from some rescaling of source terms in the layers below the affected layer, only the optical properties of the affected layer need recomputed - the others are saved in memory as individual layers and blocks of atmosphere. Following the recomputation of the affected layer, it only needs added to the other layers and/or blocks that have already been saved to obtain the new radiance.

The savings observed is because, although using an eigenmatix formulation to obtain the solution to the radiative transfer equation, DISORT must re-solve the whole radiative transfer problem when the optical properties change in a single layer. This leads to much unnecessary computation in scenarios such as encountered in this work where only the recomputation of one or two layers may be required and the rest of the atmospheric state remains the same. As further evidence of the power of these ideas, when the saving features spoken of above were implemented in computing the elements of the Jacobian for the NIR wavenumbers in this work, the computation of the Jacobian was sped up by over a factor of 14!

The above illustrates some of the benefits that Radiant can provide in the way of saved time when working on certain problems requiring repeated calls to a radiative transfer model. It is planned to make the code available to the atmospheric science community following a few modifications.

Appendix B

Global Transmission and Reflection Matrices: Numerical Considerations

In appendix A, it was asserted that the global transmission (T) and global reflection (R) matrices can be obtained from the expressions

$$\begin{aligned} T(H, 0) = & -u_+[I - (u_+^{-1}u_-)^2][(u_+^{-1}u_-)^{-1}e^{-\Lambda^+\tau(H)}] \\ & \{I - [(u_+^{-1}u_-)^{-1}e^{-\Lambda^+\tau(H)}]^2\}^{-1}u_-^{-1} \end{aligned} \quad (\text{B.1})$$

$$\begin{aligned} R(H, 0) = & -u_+[I - (u_+^{-1}u_-)e^{-\Lambda^+\tau(H)}(u_+^{-1}u_-)^{-1}e^{-\Lambda^+\tau(H)}] \\ & \{I - [(u_+^{-1}u_-)^{-1}e^{-\Lambda^+\tau(H)}]^2\}^{-1}u_-^{-1} \end{aligned} \quad (\text{B.2})$$

where u_+ and u_- are matrices, when appropriately assembled, composing the matrix X from equation (A.3), Λ^+ is a diagonal matrix containing the positive eigenvalues of the matrix A , $\tau(H)$ is the optical depth at a given altitude H , and I is the identity matrix.

If one uses the above formulation for T exactly, one will need to perform eight matrix multiplications and four matrix inversions. This amounts to twelve matrix operations proportional to n^3 . Similarly, if the exact expression for R is used, this leads to an additional four matrix multiplications (assuming that some of the matrix products used in calculating T are used again so as to avoid unnecessary recomputation). This leads to a total of sixteen n^3 operations; however, there are some substitutions and simplifications that can be done to the above expressions. Employing these techniques leads to the following equivalent expressions for T and R :

$$T(H, 0) = [u_- - u_+ u_-^{-1} u_+] e^{-\Lambda^+ \tau(H)} \{I - [u_-^{-1} u_+ e^{-\Lambda^+ \tau(H)}]^2\}^{-1} u_-^{-1} \quad (\text{B.3})$$

$$R(H, 0) = [u_- e^{-\Lambda^+ \tau(H)} u_-^{-1} u_+ e^{-\Lambda^+ \tau(H)} - u_+] \{I - [u_-^{-1} u_+ e^{-\Lambda^+ \tau(H)}]^2\}^{-1} u_-^{-1} \quad (\text{B.4})$$

If one carefully observes, T now only requires seven matrix multiplications and two matrix inversions and R an additional three matrix multiplications leading to a total of twelve n^3 operations to obtain both these matrices. Furthermore, if one employs an $A^{-1}B$ algorithm (an algorithm in which both the inverse of the matrix A and the multiplication of it by matrix B are both done at the same time), one can save an additional two n^3 operations; thus, by trimming some of the "numerical fat" as it were, one can save six n^3 operations every time these very heavily used matrices need recomputed and lowers the total number of n^3 operations required to ten. The formulations for T and R given in Benedetti et al. (2002) help make Radiant a more numerically stable code for higher optical depths while the above modifications help make it more efficient.